

1-1-1987

The physics and chemistry of dark molecular clouds : a detailed study of L134N.

Daryl A. Swade

University of Massachusetts Amherst

Follow this and additional works at: https://scholarworks.umass.edu/dissertations_1

Recommended Citation

Swade, Daryl A., "The physics and chemistry of dark molecular clouds : a detailed study of L134N." (1987). *Doctoral Dissertations 1896 - February 2014*. 3355.

https://scholarworks.umass.edu/dissertations_1/3355

This Open Access Dissertation is brought to you for free and open access by ScholarWorks@UMass Amherst. It has been accepted for inclusion in Doctoral Dissertations 1896 - February 2014 by an authorized administrator of ScholarWorks@UMass Amherst. For more information, please contact scholarworks@library.umass.edu.

UMASS/AMHERST



312066 0298 5250 7

**FIVE COLLEGE
DEPOSITORY**

THE PHYSICS AND CHEMISTRY OF DARK MOLECULAR CLOUDS:
A DETAILED STUDY OF L134N

A Dissertation Presented

by

DARYL A. SWADE

Submitted to the Graduate School of the
University of Massachusetts in partial fulfillment
of the requirements for the degree of

DOCTOR OF PHILOSOPHY

September 1987

Department of Physics and Astronomy

© Copyright by Daryl Allen Swade 1987

All Rights Reserved

THE PHYSICS AND CHEMISTRY OF DARK MOLECULAR CLOUDS:
A DETAILED STUDY OF L134N

A Dissertation Presented

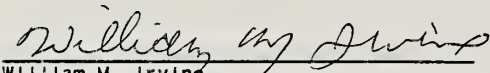
by

DARYL A. SWADE

Approved as to style and content by:



F. Peter Schloerb, chairman



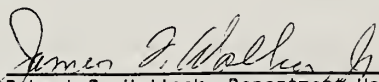
William M. Irvine



Ronald L. Spell



John L. Ragle, Department of Chemistry



Robert B. Hallock, Department Head
Department of Physics and Astronomy

ACKNOWLEDGMENTS

The majority of the observations for this work was conducted at the Five College Radio Astronomy Observatory. I would like to express my appreciation to the scheduling committee for their generous allotment of the telescope time needed to conduct a study of this type and the observatory staff for their technical assistance during the observations. FCRAO is supported by NSF grant AST 85-12903 and by the Commonwealth of Massachusetts, and is operated with the permission of the Metropolitan District Commission. This research was supported by NASA grant NGL 22-010-023 for Planetary Astronomy at FCRAO.

My years as a graduate student at the University of Massachusetts have been both challenging and enjoyable thanks to the many faculty, staff, and fellow graduates students with whom I have had the pleasure of being associated. In particular, I am grateful to my thesis committee for all their support and encouragement during my graduate career. Pete Schloerb, Bill Irvine, and Ron Snell suggested the topic of this thesis, taught me how to perform radio astronomical observations, guided me through studies of the techniques of molecular astrophysics used to analyze the data, and provided valuable insight as this thesis was being written. John Raglè helped to clarify points and bring a fresh perspective to the thesis writing. But I would especially like to thank my thesis advisor, Pete Schloerb. Through the many hours I have spent with him observing, analyzing data, and discussing the results, on this thesis and all the other projects I

have had the pleasure to work on with him, he has not only shown me what is important to think about, but how to think about it.

Finally, I could never have endured graduate school without the support of my family. I thank my parents, Clarence and Irene Swade, for all their support, encouragement, and the confidence they have shown in me. I thank my son, David, for being a constant source of joy during some otherwise trying times. And especially, I thank my wife, Marianne, for all she has sacrificed and endured. Because of her love and faith in me, this thesis is dedicated to her.

ABSTRACT

THE PHYSICS AND CHEMISTRY OF DARK MOLECULAR CLOUDS:
A DETAILED STUDY OF L134N

SEPTEMBER 1987

DARYL ALLEN SWADE

B.S., PENNSYLVANIA STATE UNIVERSITY
M.S., Ph.D., UNIVERSITY OF MASSACHUSETTS

Directed by: F. PETER SCHLOERB

The dark molecular cloud L134N has been studied in detail through radio astronomical observations of spectral lines at millimeter and centimeter wavelengths. The overall goal of this thesis is to develop a physical and chemical model for L134N, which may be applicable to other dark clouds, to provide insight into the formation of low mass stars and solar systems. L134N was chosen for this study because: (1) It is a nearby cloud at a distance of 160 parsecs, thus radio observations have high spatial resolution; (2) It resides out of the galactic disk, providing unobscured viewing along the line of sight; and (3) It is known to be a rich source of molecular emission. The absence of any embedded infrared sources leads to the assumption that L134N is either in a stage of evolution prior to star formation, or is a cloud in which internal support will prohibit stars from forming.

The large scale structure of L134N was observed by mapping the ^{13}CO J=1-0 spectral line over 1.3 square degrees on the sky. L134N contains approximately 190 solar masses of molecular gas distributed

In four subclouds, one of which appears to be rotating.

A dense core, which is not evident in the ^{13}CO map, exists within the main subcloud. This core has a kinetic temperature of 12 K, a peak molecular hydrogen density of $3 \times 10^4 \text{ cm}^{-3}$, a mass of 23 solar masses, and is characterized by maps of molecular emission from C^{18}O , CS, H^{13}CO^+ , SO, NH_3 , and C_3H_2 . The emission from each of these molecules reveals different distributions which result from C^{18}O probing a less dense envelope; NH_3 , C_3H_2 , and H^{13}CO^+ excitation from a high density condensation; CS emission suffering radiative transfer effects; and SO emission emanating from a region of high oxygen abundance. The difference between the NH_3 and C_3H_2 distributions and the SO distribution may be explained by a gradient in the gas phase C/O ratio in the L134N core. This C/O gradient could be produced by an oxygen depletion in the region of highest density due to condensation of water ice onto dust grain mantles.

In addition to the six species mapped, the dense core region was surveyed in twenty-four molecular transitions at up to seven positions. Relative abundances of the observed species provide observational constraints for theoretical models of cloud chemistry.

TABLE OF CONTENTS

ACKNOWLEDGEMENTS.....	iv
ABSTRACT.....	vi
LIST OF TABLES.....	ix
LIST OF FIGURES.....	x
 CHAPTER	
I. INTRODUCTION.....	1
II. LARGE SCALE STRUCTURE OF L134N.....	8
a) introduction.....	8
b) Observations.....	9
c) Results.....	11
d) Discussion.....	16
e) Conclusion.....	20
III. OBSERVATIONS OF THE MOLECULAR CORE.....	39
a) FCRAO.....	39
b) NRAO.....	43
c) Haystack.....	45
IV. MOLECULAR MAPPING AND SPECTRAL LINE SURVEY RESULTS.....	51
a) mapping.....	51
b) survey.....	57
c) discussion.....	64
V. PHYSICAL PARAMETERS OF THE L134N MOLECULAR CORE.....	134
a) CO analysis.....	134
b) ammonia analysis.....	146
c) HC ₃ N analysis.....	160
d) hyperfine structure.....	167
e) Isotopic variations.....	172
f) excitation summary.....	176
VI. CORE CHEMISTRY	181
a) chemical abundances.....	181
b) correlation analysis.....	198
c) chemical models.....	215
VII. SOURCE MODEL.....	240
a) excitation differences.....	240
b) chemical differences.....	242
c) L134N age.....	246
d) summary of source model.....	248
e) TMC 1.....	250
VIII. CONCLUSIONS AND PROSPECTUS.....	253
a) conclusions.....	253
b) future endeavors.....	255
BIBLIOGRAPHY.....	257

LIST OF TABLES

2.1	^{13}CO SUBCLOUD STRUCTURE	21
3.1	L134N MAPPING SUMMARY	46
3.2	FCRAO MOLECULAR SURVEY OBSERVATIONAL PARAMETERS	47
3.3	FCRAO ANTENNA PERFORMANCE	49
3.4	NRAO MOLECULAR SURVEY OBSERVATIONAL PARAMETERS	50
4.1a	FCRAO OBSERVATIONAL RESULTS	66
4.1b	H^{13}CN $J=1-0$ HYPERFINE LINES	69
4.1c	N_2H^+ $J=1-0$ HYPERFINE LINES	70
4.2a	NRAO OBSERVATIONAL RESULTS	72
4.2b	NH_3 (1,1) HYPERFINE LINES	74
4.2c	C_3H_2 $J_K^- - J_K^+ = 1_0^- - 1_0^+$ DATA AT POSITIONS OF FCRAO SURVEY	76
4.3	PARAMETERS OF MOLECULES OBSERVED IN L134N	77
5.1	NRAO NH_3 MODELING RESULTS	155
5.2	RESULTS OF ISOTOPIC VARIATIONS	175
6.1a	FCRAO LTE ABUNDANCES AT (0.6,2.9)	188
6.1b	FCRAO LTE ABUNDANCES AT (0.7,0.7)	189
6.1c	FCRAO LTE ABUNDANCES AT (-0.8,0.4)	190
6.1d	FCRAO LTE ABUNDANCES AT (-1.4,-0.8)	191
6.1e	FCRAO LTE ABUNDANCES AT (-2.8,0.8)	192
6.1f	FCRAO LTE ABUNDANCES AT (-2.3,2.0)	193
6.1g	FCRAO LTE ABUNDANCES AT (3.7,-1.2)	194
6.2	NRAO LTE ABUNDANCES.....	195
6.3	L134N MAPPED INTEGRATED INTENSITY CORRELATIONS	203
6.4	FCRAO SURVEY CORRELATIONS	204
6.5	NRAO SURVEY CORRELATIONS	208
6.6	FCRAO ABUNDANCE RATIOS	238
6.7	NRAO ABUNDANCE RATIOS	239

LIST OF FIGURES

2.1	^{13}CO J=1-0 Integrated intensity map	23
2.2	L134N on the POSS red print	25
2.3	Sample ^{13}CO J=1-0 spectra	27
2.4	L134N velocity maps a) $0.75-1.50 \text{ K km s}^{-1}$	29
	b) $1.75-2.50 \text{ K km s}^{-1}$	31
	c) $2.75-3.50 \text{ K km s}^{-1}$	33
	d) $3.75-4.50 \text{ K km s}^{-1}$	35
2.5	^{13}CO spectra at low and high velocity peaks of Feature 2	37
2.6	^{13}CO J=1-0 column density vs. radius in L134N	38
4.1	^{13}CO J=1-0 Integrated intensity map of core region	80
4.2	Integrated Intensity contour map of a) C^{18}O J=1-0	81
	b) CS J=2-1	82
	c) H^{13}CO^+ J=1-0	83
	d) SO N, J=2, 3-1, 2	84
	e) NH_3 (1,1)	85
	f) C_3H_2 $1_{10}^{-1}0_1$	86
4.3	Contour map of ^{12}CO peak Intensity	87
4.4	L134N survey positions	88
4.5	^{12}CO J=1-0 FCRAO survey spectra	90
4.6	C^{18}O J=1-0 FCRAO survey spectra	92
4.7	CS J=2-1 FCRAO survey spectra	94
4.8	C^{34}S J=2-1 FCRAO survey spectra	96
4.9	HCS^+ J=2-1 FCRAO survey spectra	98
4.10	H^{13}CO^+ J=1-0 FCRAO survey spectra	100
4.11	HC^{18}O^+ J=1-0 FCRAO survey spectra	101
4.12	H^{13}CN J=1-0 FCRAO survey spectra	102
4.13	HN^{13}C J=1-0 FCRAO survey spectra	104
4.14	HC_3N J=5-4 FCRAO survey spectra	106
4.15	HC_3N J=9-8 FCRAO survey spectra	107
4.16	C_3H_2 $2_{12}^{-1}0_1$ FCRAO survey spectra	109
4.17	N_2H^+ J=1-0 FCRAO survey spectra	111

4.18	SO N, J=2,3-1,2 FCRAO survey spectra	113
4.19	SO N, J=2,2-1,1 FCRAO survey spectra	115
4.20	³⁴ SO N, J=2,3-1,2 FCRAO survey spectra	117
4.21	SO ₂ 3 ₁₃ -2 ₀₂ FCRAO survey spectra	119
4.22	OCS J=7-6 FCRAO survey spectra	120
4.23	NH ₃ (1,1) NRAO survey spectra	122
4.24	NH ₃ (2,2) NRAO survey spectra	124
4.25	C ₃ H ₂ 1 ₁₀ -1 ₀₁ NRAO survey spectra	126
4.26	HC ₃ N J=2-1 NRAO survey spectra	128
4.27	C ₄ H N=2-1, F=3-2 NRAO survey spectra	130
4.28	C ₄ H N=2-1 F=2-1 NRAO survey spectra	132
4.29	HC ₃ N J=2-1 NRAO spectrum at (0.6,3.3)	133
5.1	¹² CO J=1-0 excitation temperature across L134N core	141
5.2	CO excitation temperature as a function of density	142
5.3	¹³ CO and C ¹⁸ O J=1-0 optical depth maps in L134N core	144
5.4	Ratio of LTE to LVG column densities as a function of density	145
5.5	Contour map of NH ₃ (1,1) total integrated intensity	156
5.6	Contour maps of L134N core a) NH ₃ (1,1) optical depth	157
	b) NH ₃ (1,1) excitation temperature.	158
	c) molecular hydrogen density	159
5.7	HC ₃ N rotation diagram	165
5.8	HC ₃ N J=5-4/J=9-8 line ratio as a function of density	166
5.9	LTE main line optical depth vs. hyperfine intensity	171
5.10	Characteristic density vs. size for mapped transitions	180
6.1	Integrated intensity of CS J=2-1 and HCS ⁺ J=2-1 vs. C ³⁴ S J=2-1	210
6.2	Integrated intensity of HC ₃ N J=5-4, C ₃ H ₂ 2 ₁₂ -1 ₀₁ , and H ¹³ CN J=1-0 vs. HN ¹³ C J=1-0	212
6.3	Integrated intensity of SO 2,3-1,2, ³⁴ SO 2,3-1,2 and SO ₂ 3 ₁₃ -2 ₀₂ vs. SO 2,2-1,1	214

CHAPTER I

INTRODUCTION

Dark molecular clouds are observed to be sites of low mass star formation, and conditions within these high density clouds provide clues about the formation of protostellar nebulae and solar type stars. Therefore, initial boundary conditions for solar system formation may be obtained from observations of dark cloud composition, structure, and dynamics.

Within the dense core regions of dark clouds, the dust and gas reach a high enough density to initiate gravitational collapse into prestellar nebulae which give rise to stars of approximately solar mass. At these high densities, most of the gas is in the molecular state because the extinction due to dust grains shields the core from the interstellar ultraviolet radiation field. In the absence of internal heat sources, the kinetic temperature is about 10 Kelvin. The principle means of heating in these regions is cosmic rays which penetrate into the core (Goldsmith and Langer 1978). The dominant constituents of the core, H_2 and He, transfer their kinetic energy through collisions to the trace molecules, which cool the cloud through spectral line radiation in the infrared and radio region of the

electromagnetic spectrum. Hence, observations of high frequency molecular emission lines provide an excellent probe of the physical and chemical properties of the gas within these clouds.

One such dark cloud is L134N. This cloud was catalogued by Lynds (1962) as source L183 because of its high visual extinction on the Palomar Observatory Sky Survey, and later molecular line observers labeled the same region as L134N for Lynds 134 North, since it lies two degrees north of L134. The location of L134N provides two advantages for observations. First, this cloud lies in a relatively isolated region of the sky, and therefore observations are uncluttered along the line of sight. Secondly, it lies at a distance of only 160 parsecs (Snell 1981). Hence, it is still well within the galactic disk despite its high galactic latitude of 36° . This proximity makes it possible to study L134N at a higher spatial resolution than is possible with most other molecular sources.

Another advantage L134N offers for studies of physical properties and chemistry of dark clouds is the absence of any complications from internal energy sources. Snell (1981) determined that five stars observed in the infrared, which are spatially coincident with the L134N CO emission, are background sources not associated with the L134N cloud. Also, infrared surveys by Sargent *et al.* (1983) and the Infrared Astronomical Satellite (IRAS) Point Source Catalogue (1985) did not find any far-infrared sources within the boundaries of the

L134N molecular cloud. Thus, L134N is either in a stage of evolution that precedes proto-stellar formation, or it is a cloud in which internal dynamics will prohibit the formation of stars.

L134N has been well studied at radio wavelengths and is known to be a rich source of molecular emission. A dense core of molecular material exists within the dark cloud L134N. This core is not evident from the ^{13}CO observations presented in Chapter II, because the ^{13}CO emission is not sensitive to the dense gas which defines the core. However, observations of the 2 mm transition of formaldehyde (H_2CO) by Evans and Kutner (1976) revealed a peak near the position; RA = $15^{\text{h}}51^{\text{m}}30^{\text{s}}$, DEC = $-2^{\circ}43'31''$ (1950.0) (see Caldwel 1979 for a review of early observations). Subsequent observations have discovered many molecular emission lines emanating from this core in the millimeter and centimeter region of the electromagnetic spectrum. These observations include maps of ammonia, NH_3 (Ungerechts, Walmsley, and Winnewisser 1980), the formyl ion, HCO^+ (Guellin, Langer, and Wilson 1982), and carbon monosulfide, CS (Snell et al. 1982). Even a cursory look at these maps indicates a different nature of emission for each of the transitions. The CS map has a ridge structure which extends from the southeast to the northwest, the NH_3 emission shows a double peak clump with a definite north-south elongation, while the HCO^+ map indicated a centrally peaked, spherical condensation.

Dense cores of molecular clouds are the sites of an abundant and complex molecular chemistry. Shielded from the dissociating effects of the interstellar ultraviolet radiation field, gas phase chemical reactions, along with possible chemical reactions on the surface of dust grains, produce an array of molecules, some of which may be observed through their radio emission lines. Through radio observations of molecules with permanent electric dipole moments, relative abundances may be estimated, and a picture of the chemical state of the core generated. Models of time dependent chemistry (e.g., Leung, Herbst, and Huebner 1984; Prasad and Huntress 1980a) within the core can then be used to fill in the missing pieces of the entire chemical puzzle. However, observations which can accurately determine the relative abundance of various molecular species are necessary to place constraints on these models.

Thus, microwave spectroscopy has two applications in the study of dark clouds. First, the observed spectral lines can be used to probe the physical conditions within the dark cloud. This can be accomplished by a number of techniques including: observing single spectral lines indicative of a certain physical parameter of the cloud (e.g., column density); multitransitional studies of a species which can provide a determination of column density, rotational temperature, and through the use of statistical equilibrium calculations, total density and relative abundances; studies of isotopic variations, which provide information on the optical depth and excitation temperature of

the transitions studied; and analysis of the hyperfine structure of a transition, which can provide optical depth, excitation temperature, and column density. The crucial step in forming a detailed picture of the cloud is the transformation of the parameters determined directly from the observations (such as column density, excitation temperature, optical depth, and line profile) into physical parameters of the cloud (such as molecular hydrogen number density, kinetic temperature, cloud size, geometry, and velocity structure). Secondly, the observed spectral lines may be used to determine abundances of the molecular species, hence determine the chemical composition of the cloud. The chemical composition may then be used to place constraints on the chemical models of the clouds (e.g., Prasad and Huntress 1980b, 1982; Millar and Freeman 1984a, b; Leung, Herbst, and Huebner 1984, Herbst and Leung 1986a, b), which in turn may constrain the state of evolution of the physical parameters of the cloud.

A molecular mapping project was undertaken in order to further elucidate the molecular distribution differences described above through observations of complementary transitions and production of high spatial resolution maps. These observations include an extended ^{13}CO $J=1-0$ map to investigate the large scale structure of L134N, along with molecular maps of ^{12}CO , C^{18}O , CS, H^{13}CO^+ , SO, NH_3 , and C_3H_2 in the region containing the dense core. The mapping revealed a different distribution for each of the molecular emissions and posed the question as to whether these differences were due to varying conditions of

excitation for the mapped transitions or due to actual chemical abundance variations within the core region.

Since the mapping of more molecular emission lines would require inordinate amounts of observing time, a survey of other molecular species at as many as seven positions at peaks in the integrated intensity of the maps was conducted. In all twenty-four transitions at millimeter and centimeter wavelengths were observed. The goals of this survey were to obtain a consistent set of observational data which would accurately determine relative abundances of the observed molecular species in order to provide better constraints for models of cloud chemistry, and through association with a molecular map to determine the region within the core in which emission from a surveyed species originates. In this way the core mapping and survey could lead to a determination of the physical conditions probed by the various molecular emission lines.

Overall, the goal of this thesis is to develop a physical and chemical model for L134N, which may be applicable to other dark clouds, and which may provide insight as to how the physical and chemical evolution of molecular clouds leads to the formation of stars and solar systems. In Chapter II, the large scale structure of L134N is discussed, and a perspective for the study of the molecular core is established. The core observations are presented in Chapter III and the results of these observations are discussed in Chapter IV for both

the core mapping and spectral line survey. In Chapter V the observed spectra are analyzed to determine the physical parameters of the L134N core. Abundances with respect to molecular hydrogen are estimated and the results are discussed in terms of chemical models in Chapter VI. Chapter VII presents a source model to explain the observations. Finally, conclusions are summarized and future studies are discussed in Chapter VIII.

CHAPTER 11

LARGE SCALE STRUCTURE OF L134N

a) Introduction

Cold, dark molecular clouds are known to be the sites of low mass star formation, and conditions in the dense cores of dark clouds are believed to give rise to stars of approximately solar mass. The study of the physical properties and kinematics of the large scale structure of these clouds is essential to an understanding of cloud collapse and fragmentation from a diffuse interstellar cloud into a proto-stellar nebulae. Observations of the large scale structure of the dark cloud L134N were undertaken in an effort to investigate the processes which may lead to the formation of low mass stars in molecular clouds of this type (cf. Scalo 1985), as well as to provide a context for the study of the molecular core region.

L134N appears to be associated with the Lynds sources L134 and L1778 (Clark and Johnson 1981). The relative isolation of this entire system and the similar velocity with respect to the local standard of rest of the individual clouds in the system suggest that these three clouds are physically related to each other, and not clouds at different distances superimposed on the plane of the sky. If this is

the case, it is likely that either they formed simultaneously from collapse of a more diffuse cloud and accreted interstellar gas into their present form, or that they are segments of a once larger molecular cloud which has undergone fragmentation. Infrared surveys have indicated that there are no internal sources embedded within the regions of high column density in L134N (Snell 1981, Sargent *et al.* 1983, IRAS Point Source Catalogue 1985), hence this cloud has not yet undergone star formation.

b) Observations

In order to trace the large scale structure and kinematics of L134N, a map of the ^{13}CO J=1-0 emission at a wavelength of 2.7 millimeters was made with the 14 meter radio telescope of the Five College Radio Astronomy Observatory (FCRAO). CO is the most abundant constituent of the molecular gas with a permanent dipole moment and is easily observable at millimeter wavelengths. Observations of the ^{13}CO J=1-0 transition offer an excellent tool for probing the structure of dark clouds because it is believed to be a good tracer of the column density of the molecular gas (Dickman 1978). Since the terrestrial $^{13}\text{C}/^{12}\text{C}$ ratio of 1/89 is representative of this ratio in nearby dark clouds (Wilson *et al.* 1981; Henkel *et al.* 1982), ^{13}CO emission can probe the cloud to a greater depth than the more optically thick ^{12}CO , while ^{13}CO is still readily detected in short integrations. However, it is not an ideal tracer of the molecular column density since it does become optically thick in the densest region of the cloud (Dickman

1978; Frerking, Langer, and Wilson 1982). Hence, the ^{13}CO isotopic variant is chosen as a compromise between the more optically thick ^{12}CO and the more optically thin C^{18}O , whose emission would be too weak to thoroughly map over the extent of the cloud. The observed ^{13}CO spectra provide information on the intensity and velocity of the molecular emission, from which can be deduced size scales, masses, densities, and velocity structure of the molecular gas component of the cloud.

A ^{13}CO map of L134N was constructed from spectra obtained with the FCRAO radio telescope during the spring of 1984. This map covers 1.3 square degrees of the sky and consists of 2051 individual spectra. The 1177 innermost spectra were sampled at one arcminute resolution (the half-power beam width of the telescope at the frequency of ^{13}CO J=1-0 is about 50"), and 874 spectra sample the rest of the cloud at two arcminute resolution. At a distance of 160 parsecs to L134N, the high resolution (1') spacing gives a spatial resolution of 0.05 parsecs (1×10^4 AU). The map coordinate offsets are referenced to the position RA = $15^{\text{h}}51^{\text{m}}30^{\text{s}}$, DEC = $-2^{\circ}43'31''$ (1950.0); and the map extends 9' north, 59' south, 34' east, and 54' west of this reference position.

The integration time for each spectra was 30 seconds, and the data were obtained by frequency switching 5 MHz (14 km s^{-1}) in a 256 channel filterbank spectrometer with a spectral resolution of 100 kHz, corresponding to 0.27 km s^{-1} at the ^{13}CO J=1-0 frequency of 110.201370 GHz. The excellent sensitivity of the FCRAO cooled mixer receiver, which produced single sideband system temperatures referenced to above

the Earth's atmosphere in the range of 500 to 1000 degrees Kelvin during the observations, enabled the short integration times. Calibration of the data was accomplished using the standard chopper wheel technique (Penzias and Burris 1973) with an image sideband rejection filter in place during all the observations. Antenna temperatures were corrected to the T_R^* temperature scale as suggested by Kutner and Ulich (1981) by dividing the observed antenna temperatures, T_A^* , by the forward scattering and spillover efficiency, η_{fss} , taken to be 0.70 at the frequency of these observations based on measurements of the Moon (Snell 1985). The typical root-mean-square noise in the individual spectra is 0.3 to 0.5 Kelvin measured on the T_R^* temperature scale, such that the signal-to-noise in the map peaks at 20. The ^{13}CO spectra were boxcar smoothed at a resolution of 0.5 km s^{-1} , and resampled at a resolution of 0.25 km s^{-1} , which typically decreased the noise by a factor of three.

c) Results

The integrated intensity of the ^{13}CO J=1-0 spectral lines is presented in the form of a gray scale image in Figure 2.1. This image can be compared with the same area of the sky from the Palomar Observatory Sky Survey (POSS) red plate shown in Figure 2.2. There is a high degree of correlation between the integrated intensities of ^{13}CO emission and amount of visual obscuration on the sky, which is due to the linear relation between these two quantities found by previous observers (e.g., Dickman 1978; Frerking, Langer, and Wilson 1982).

The spectra in Figure 2.3 exemplify ^{13}CO $J=1-0$ emission in L134N. The lines are mostly single peaked with a maximum intensity lying in the velocity range of 2.0 to 2.5 km s^{-1} . The line wings are generally more extended on the high velocity side which may suggest large scale motion toward the cloud center (Myers 1980) or a lower excitation component of the molecular gas with broader lines. Double peaked spectra such as the line at position (6,0) probably indicate self-absorption of the ^{13}CO emission by lower excitation foreground material along the line of sight to this position rather than multiple velocity components since the dip occurs near the peak velocity of other lines.

Assuming that the ^{13}CO $J=1-0$ emission is optically thin over most of the cloud (refer to Chapter V for a discussion of ^{13}CO optical depth), the column density of ^{13}CO can be related to the integrated intensity by the relation

$$N(^{13}\text{CO}) = 3.6 \times 10^{14} \int T_R^* dv / f_1 \quad (2.1)$$

where f_1 is the fractional population of the upper ($J=1$) level which is 0.5 assuming LTE at 10 K (Schloerb and Snell 1984). A core kinetic temperature of 10 K is determined from observations of the ^{12}CO molecular emission (Snell 1981). In this equation, the units of column density are cm^{-2} and the units of integrated intensity are K km s^{-1} . Hence, the column density of optically thin ^{13}CO is linearly proportional to the integrated intensity, and therefore is also proportional to the visual obscuration.

From a determination of the ^{13}CO column density over the region observed, the total mass of L134N can be estimated. Assuming a fractional abundance for $^{13}\text{CO}/\text{H}_2$ of $1. \times 10^{-6}$ (Heyer et al. 1987), the total molecular column density can be obtained from the ^{13}CO column density. By summing the total column density over the area mapped, the total mass of the cloud is estimated to be 190 solar masses, but may be as much as 74 percent higher or 22 percent lower. This error estimate has contributions from four sources. (1) The optically thin approximation for ^{13}CO used to derive equation 5.1 does not strictly hold. If the ^{13}CO J=1-0 had a uniform optical depth of 1, an underestimation of the mass by 58 percent would result. (2) The $^{13}\text{CO}/\text{H}_2$ fractional abundance may be as high as 1.4×10^{-6} (Frerking, Langer, and Wilson 1982) or as low as 9×10^{-7} from the $\text{C}^{18}\text{O}/\text{H}_2$ fractional abundance found by Frerking, Langer, and Wilson scaled by the terrestrial $^{13}\text{CO}/\text{C}^{18}\text{O}$ ratio. (3) The error in the determination of the J=1 level population is 20 percent (Schloerb and Snell 1984). (4) The degree of saturation of the ^{13}CO J=1-0 emission in the densest region of the core may underestimate the mass as much as 12 percent based on a dense core mass of 23 solar masses determined from the C^{18}O J=1-0 emission (Chapter V).

Low level ^{13}CO emission extends over most of the region mapped, and the size of the cloud as determined from the spatial extent of this emission is about 1.7 parsecs. Assuming spherical symmetry this size and mass give a mean density of about 200 cm^{-3} over the entire region

mapped, which must be characteristic of the minimum density required to excite the ^{13}CO J=1-0 emission.

1) subcloud structure

The ^{13}CO image demonstrates that the large L134N cloud is irregular and fragmented in appearance. The total area mapped has been divided into seven regions, in four of which subclouds are evident as indicated in Figure 2.1. Table 2.1 lists physical parameters determined from the subclouds. Individual subcloud masses are determined from the ^{13}CO observations in the same manner as described above. A characteristic radius, R , of each subcloud region is determined to be one-half of the square root of the mapped area. This radius is used to determine the mean molecular hydrogen densities, which are estimated for each subcloud assuming spherical symmetry. Since it might be argued that the size of the cloud determined in this manner depends on the area observed, an alternative characteristic radius, R_{HP} , of each subcloud region is determined to be one-half of the square-root of the area of ^{13}CO emission greater than 3.5 K km s^{-1} , which is approximately one-half the peak integrated intensity observed in L134N. This quantity is listed in Table 2.1 for comparison. Regions 5, 6, and 7 in Figure 2.1 do not contain a significant amount of integrated intensity and are excluded from Table 2.1.

The most massive of the subclouds lies in region 1. It has sharp boundaries along the north with extensions in the south and southwest.

The high density core, which is the source of many molecular transitions and will be examined in the following chapters, is in the northern part of this subcloud and lies within the box in region 1 of Figure 2.1. The ^{13}CO emission does not give any indication of its presence. Region 2, which was also Feature 2 in the H_2CO map of Clark and Johnson (1981), appears in the southwest corner of Figure 2.1. The subcloud in this region actually appears as two clumps in the image of Figure 2.1, but is connected in velocity space and appears to be rotating as will be discussed below. The subcloud in region 3, which is in the western portion of the map, seems to be a connecting filament between the subclouds of region 1 and region 2. A southern subcloud appears in region 4, below the main body of the subcloud in region 1. Finally, an extension of the main subcloud in region 1 appears in the far eastern edge defined as region 5. Areas in Figure 2.1 not numbered were not observed.

ii) kinematics

The intensity within individual velocity bins across the ^{13}CO emission line profile is shown in Figure 2.4. Each map represents the emission averaged over a velocity width of 0.25 km s^{-1} centered on an indicated velocity with respect to the local standard of rest. Scanning through the individual images allows one to examine the complex velocity structure of L134N. In general, the same features can be seen in the individual velocity images as seen in the integrated intensity image. However, there are some distinctive features

particular to certain velocities. At low velocity, there is a sharp ridge which extends north-south along the eastern edge of the cloud. The most intense emission from the main subcloud is at 2.5 km s^{-1} , while that of regions 4 and 5 occurs at slightly lower velocities of about 2.25 km s^{-1} . The filamentary region 3 also peaks at 2.0 to 2.25 km s^{-1} .

The velocity structure of the subcloud in region 2 indicates that it is rotating. In the southeast, the maximum line intensity occurs at low velocities and progresses to the northwest as the velocity increases. A velocity gradient for this feature is estimated to be $3.4 \text{ km s}^{-1} \text{ pc}^{-1}$. Figure 2.5 shows spectra at the peaks of the low and high velocity range of region 2. Not only does the peak velocity position shift between the two spectra, but the extended emission from the line wings shifts from velocities greater than the peak for the low velocity line to velocities lower than the peak for the high velocity line. From the observed size and velocity gradient of this subcloud, a dynamic mass can be determined by assuming a balance between potential energy and centripetal acceleration. This mass is $24 M_{\odot} / \sin^2 i$ where i is the angle of inclination of the rotation axis to the line of sight.

d) Discussion

Hunter (1962) proposed a model in which interstellar clouds undergo spherically symmetric collapse from an initially spherical gas

cloud. During the collapse, perturbations cause dynamic instabilities which lead to the breakup of the symmetric flow and form cloud fragments. More recent numerical models which include rotation (Bodenheimer et al. 1980, Terebey et al. 1984) and the effect of magnetic fields (Shu 1983) have improved on this simple model and still find fragmentation not only possible, but necessary in order to conserve angular momentum in a collapsing cloud. The images previously presented show a clumpy structure for the L134N molecular cloud, perhaps indicating that such a fragmentation process has taken place.

Studies by Larson (1981) and Myers (1983) have shown that clouds collapse while remaining in a quasi-virial equilibrium. A virial mass for the five subclouds is listed in Table 2.1 based on the equation

$$M_V = 210 R(\text{pc}) \Delta v^2 (\text{km s}^{-1}) M_\odot \quad (2.2)$$

(Dickman et al. 1986) where Δv is the observed ^{13}CO J=1-0 line width taken to be 1.25 km s^{-1} . The virial masses are greater than, but generally in close agreement with the masses determined from the ^{13}CO integrated intensities, indicating that the subclouds are close to virial equilibrium and marginally stable against further collapse. The extension of this quasi-static virial equilibrium collapse to the dense molecular core is demonstrated by the C^{18}O data listed in Table 2.1 taken from Chapter IV. Despite an increase in density by an order of magnitude indicated by the C^{18}O observations, the dense core is still close to virial equilibrium.

With the assumption of spherical symmetry, a density as a function of radius can be modeled for the subcloud in region 1 from the ^{13}CO observations. If a density power law is assumed, such that $n(\text{H}_2)$ is proportional to r^α , then the column density as a function of projected radius, R , can be represented by

$$\log N(R) = \text{constant} + (\alpha+1) \log R. \quad (2.3)$$

The column density for each integrated intensity can be determined from equation (2.1). A projected radius for each integrated intensity from 0.0 to 7.0 K km s⁻¹ is defined to be one-half the square-root of the area greater than the corresponding integrated intensity value. Figure 2.6 shows the results of this calculation in which the column density is plotted as a function of projected radius for each integrated intensity bin. A linear fit to the five highest column density points indicates a power law decrease in column density as a function of radius with a slope of -0.19, which indicates density decreasing as $r^{-1.2}$. This density law is less than that which results from an isothermal cloud in gravitational equilibrium, r^{-2} , or from free-fall collapse, $r^{-3/2}$, but does roughly agree with that found by Larson (1981), $r^{-1.1}$, for the relationship between mean density and size of interstellar clouds. At lower column densities the deviation from this line may be caused by both a decrease in the abundance of CO and diminished ^{13}CO excitation at lower densities.

The high values for the observed ^{13}CO line widths are characteristic of those observed in molecular clouds. These line widths are much greater than the thermal width of 0.1 km s⁻¹ for CO at

10 K indicating that a non-thermal process is responsible for the broadening. Two proposed mechanisms which provide support for the cloud from free-fall collapse are turbulent broadening by large scale motions (cf. Myers 1983) and magnetic support (Myers and Goodman 1987). At present it is difficult to distinguish between these mechanisms but both are most likely present at some level. Turbulent motion may require an energy source to maintain itself against viscous dampening unless the time scale for dissipation is sufficiently long.

Because of the presence of non-thermal support, cloud age is believed to be much greater than the free-fall collapse time

$$t_{ff} = 16.6 [(R^3(\text{pc})/M(M_\odot))]^{-1/2} \times 10^6 \text{ yrs} \quad (2.4)$$

which is shown in Table 2.1 for each subcloud to be typically on the order of one million years. Numerical models by Shu (1977) indicate that massive cores form before the collapse of outer envelopes. Since high density regions evolve more rapidly, all size scales of the cloud collapse and fragmentation process should be simultaneously visible. This allows for the dense cores to evolve a complex chemistry while the large scale structure is still intact. Time dependent chemical models for dense molecular cores indicate a time scale of 10^6 - 10^7 years for the production of complex species found in the L134N core (e.g., Leung, Herbst, and Huebner 1984), hence it seems that the large scale structure can be stable for at least as many as 1 to 10 free-fall time scales.

e) Conclusion

L134N appears to have a hierarchical structure which begins on the largest scale as an association with the molecular clouds L134 and L1778, continues through a fragmented structure for L134N itself, and ends with a dense molecular core. The observations presented in the following chapters indicate that this dense molecular core is further divided into an outer low density region characterized by $C^{18}O$ emission and a high density condensation characterized by NH_3 emission which may be the site of future star formation. This structure is suggestive of models of collapse and fragmentation of a generally spherical precursor cloud, where the successive stages of fragmentation and collapse will eventually produce stars. Observations of the ^{13}CO emission from the L134N molecular cloud indicate that each subcloud is near virial equilibrium, hence the entire cloud is in a state of quasi-static collapse. Free-fall collapse is inhibited by non-thermal pressure as indicated by ^{13}CO line widths much larger than would be produced solely by thermal broadening.

The main subcloud contains the dense molecular core identified by rarer molecular species. This dense core, which is not evident from the ^{13}CO observations that only probe low density gas, will be the object of study in subsequent chapters.

TABLE 2.1

 ^{13}CO SUBCLOUD CHARACTERISTICS

region	M (M_{\odot})	area (sq ')	R (pc)	$\langle n(\text{H}_2) \rangle$ (cm^{-3})	R_{HP} (pc)	M_V (M_{\odot})	t_{ff} (10^6 yr)
1	76	1040	0.76	840	0.48	250	1.3
2	52	1128	0.79	510	0.26	260	1.6
3	18	408	0.47	840	0.17	150	1.3
4	22	920	0.71	300	0.16	230	2.1
total	191	5366	1.72	180	0.60	560	2.7
C^{18}O	23	148	0.29	4700	0.19	22	0.54

Figure 2.1 A contour map and gray scale image of the integrated intensity over the ^{13}CO J=1-0 emission line in the dark cloud L134N. The image was constructed from 2051 spectra obtained with the FCRAO 14 m radio telescope. The core region was sampled at a resolution of one arc-minute and consists of 1177 of the spectra, while the remaining 874 spectra sample the rest of the cloud at two arc-minute resolution. The map is referenced to the position: RA = $15^{\text{h}}51^{\text{m}}30^{\text{s}}$, DEC = $-2^{\circ}43'31''$ (1950.0); and extends 9' north, 59' south, 34' east, and 54' west of the reference position. There are ten contour levels ranging from 2.5 to 7.0 K km s^{-1} in steps of 0.5 K km s^{-1} . Numbered regions are discussed in the text, while unnumbered regions were not observed. The inset box in region 1 indicates the area over which the dense molecular core was mapped.

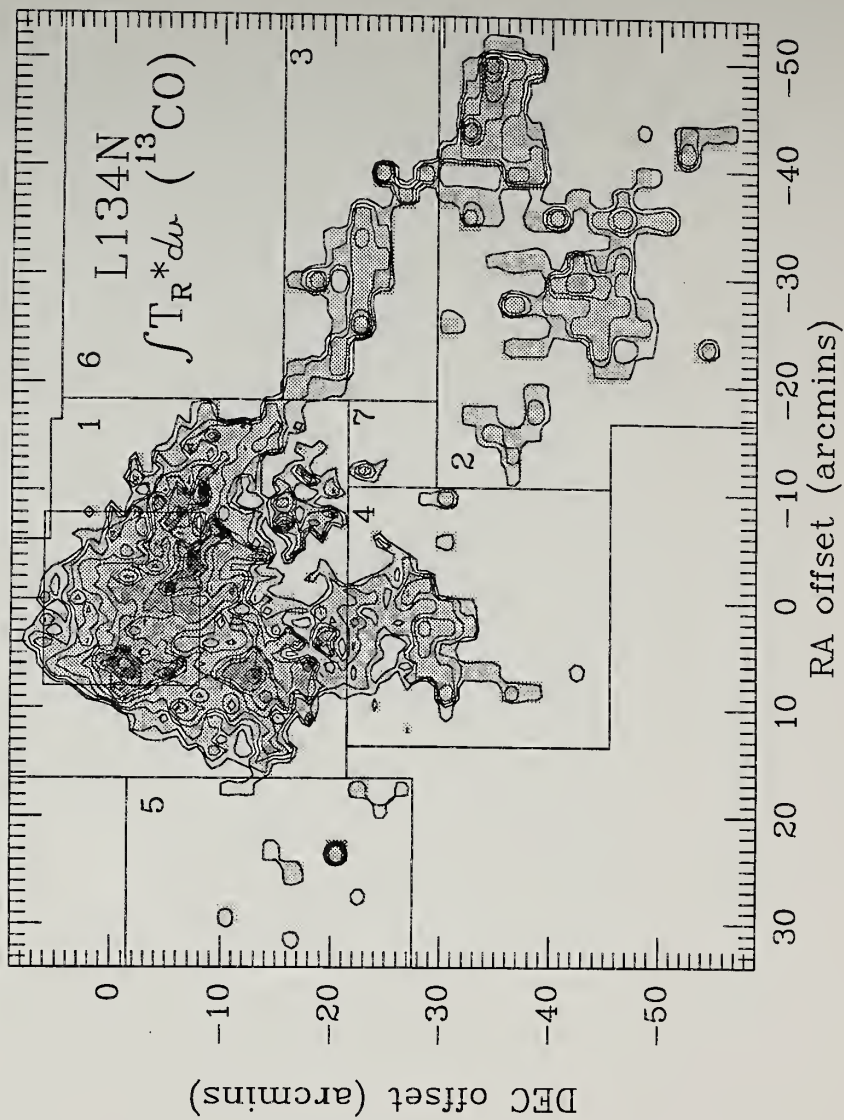


Figure 2.2 An enlarged portion of the Palomar Observatory Sky Survey red (E) print which covers the region including L134N. The ^{13}CO 2.5 and 7.0 K km s^{-1} integrated intensity contour levels are superimposed. Coordinate offsets are as in Figure 2.1.

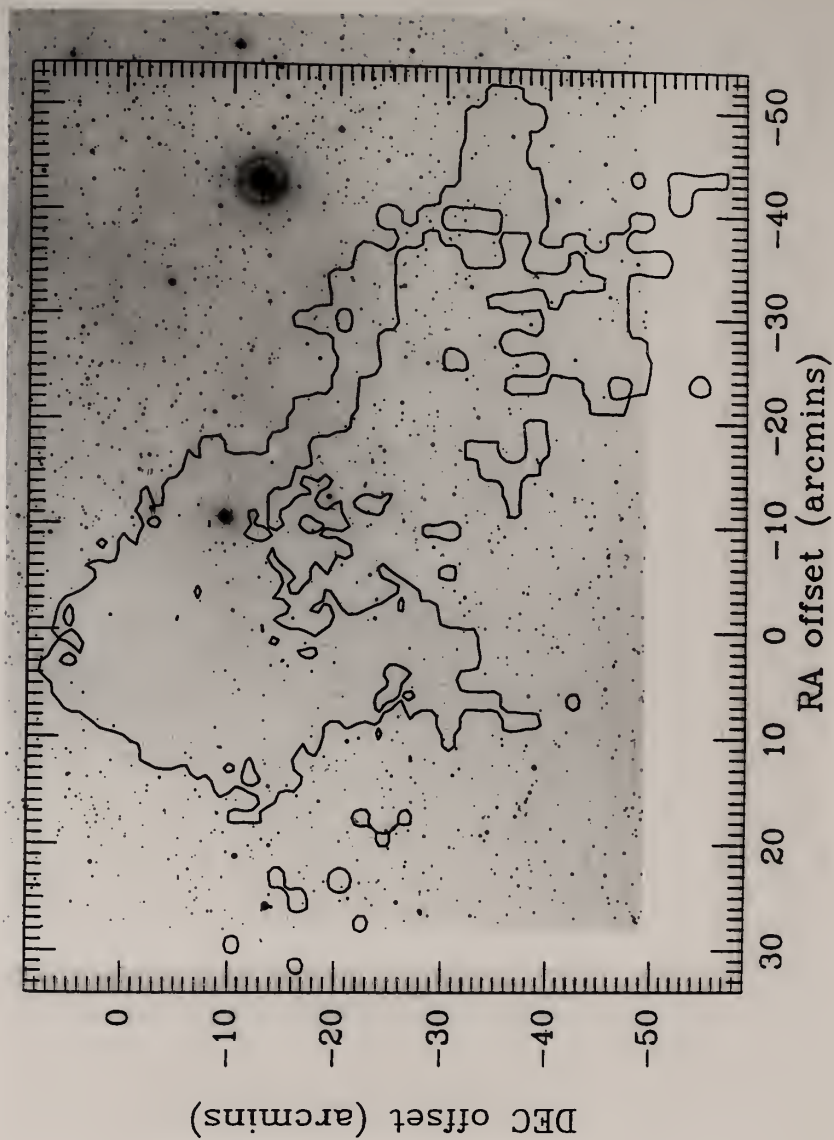


Figure 2.3 Sample ^{13}CO J=1-0 spectra. The coordinates represent the position in the map of Figure 2.1 from which the spectra were taken.

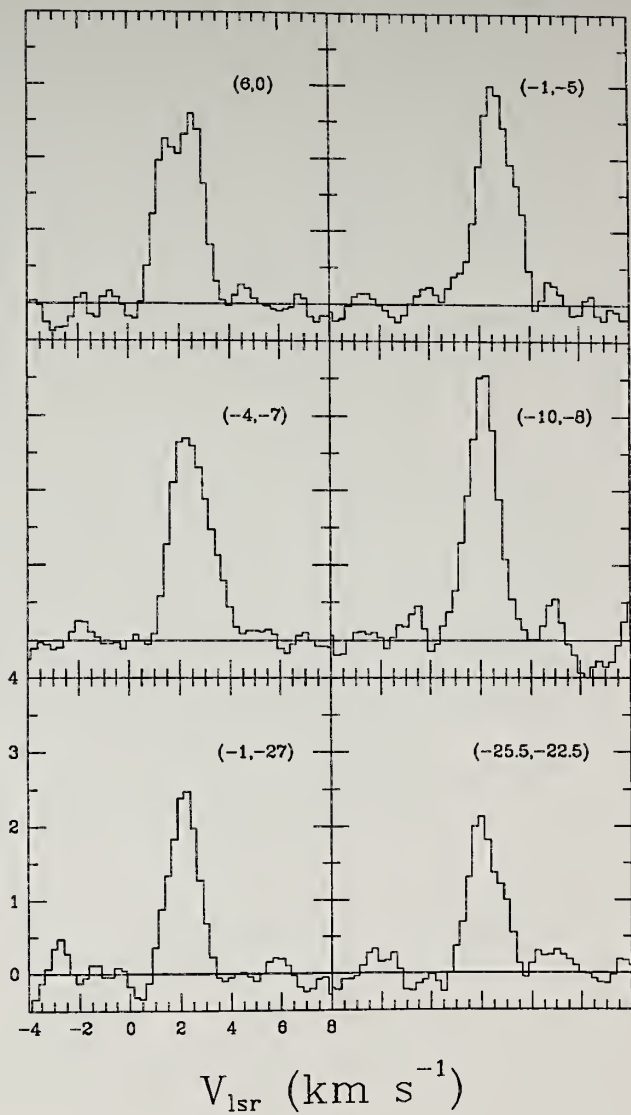
$^{13}\text{CO } J=1-0$
 T_A^* (K)

Figure 2.4 Intensity maps for individual channels of the ^{13}CO emission line averaged in bins of 0.25 km s^{-1} at individual velocities with respect to the local standard of rest scale. The center velocity of each bin is labeled in the upper right of each map in units of km s^{-1} . There are five contour levels ranging from 1. to 5. K in steps of 1. K. Scanning the images in velocity space reveals the complex structure of the L134N cloud.

a) Velocities $0.75, 1.00, 1.25, \text{ and } 1.50 \text{ km s}^{-1}$.

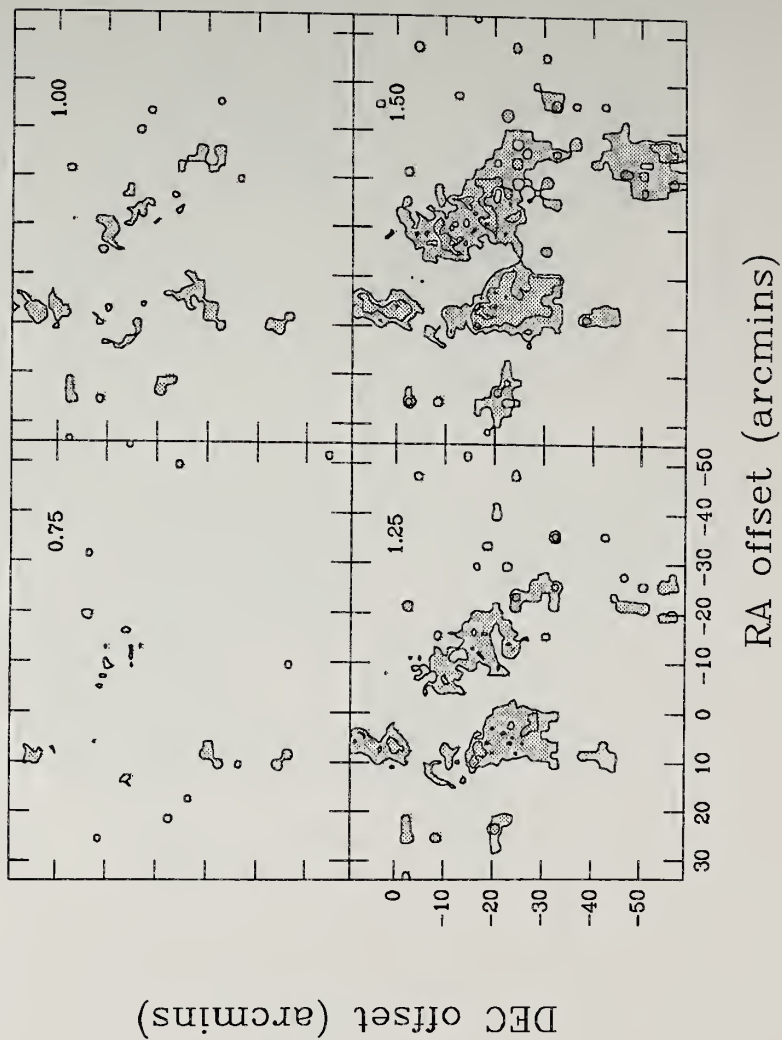


Figure 2.4 b) Velocities 1.75, 2.00, 2.25, 2.50 km s⁻¹.

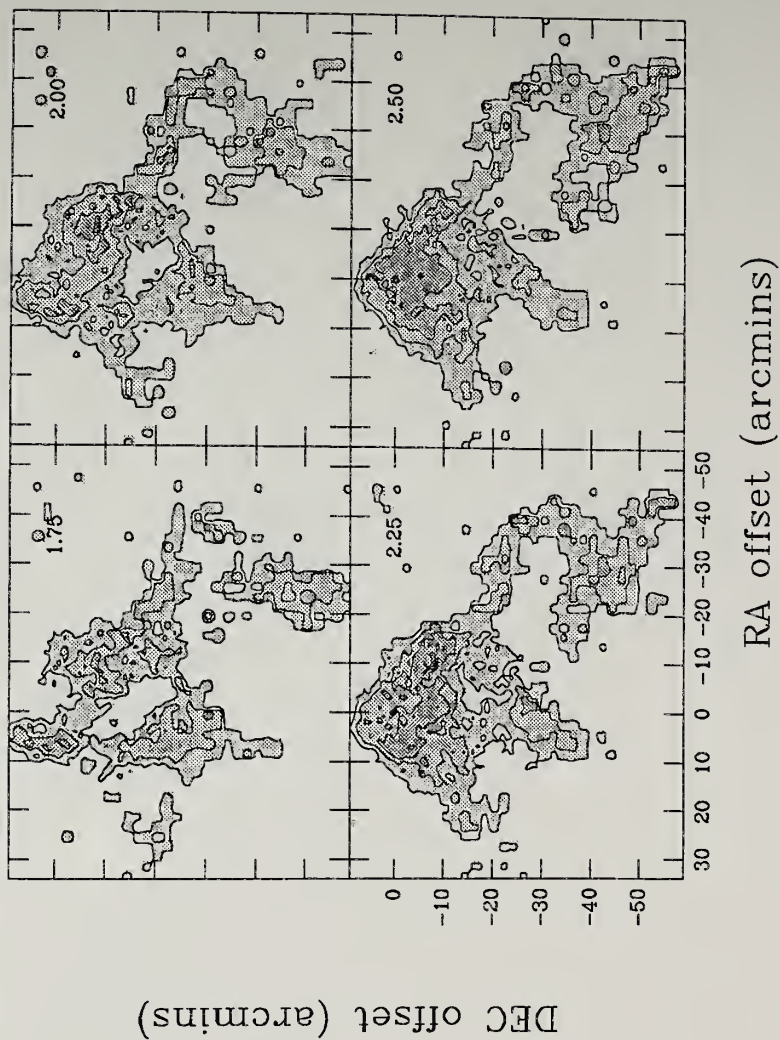


Figure 4.2 c) Velocities 2.75, 3.00, 3.25, 3.50 km s⁻¹.

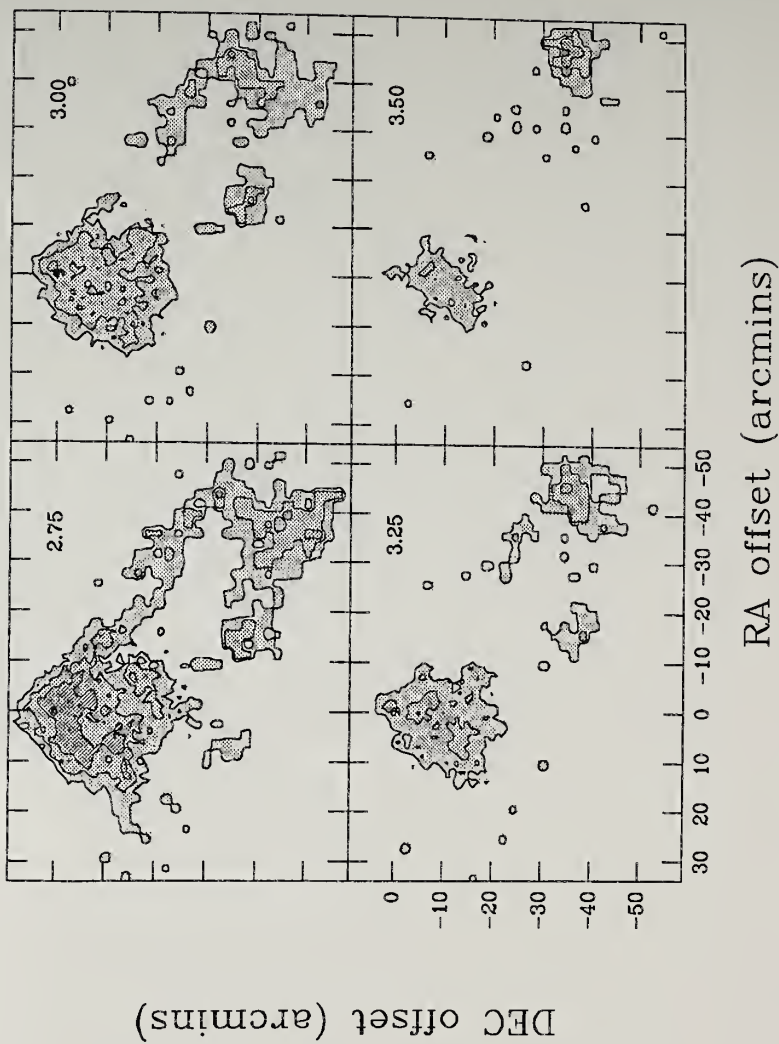


Figure 4.2 d) Velocities 3.75, 4.00, 4.25, 4.50 km s⁻¹.

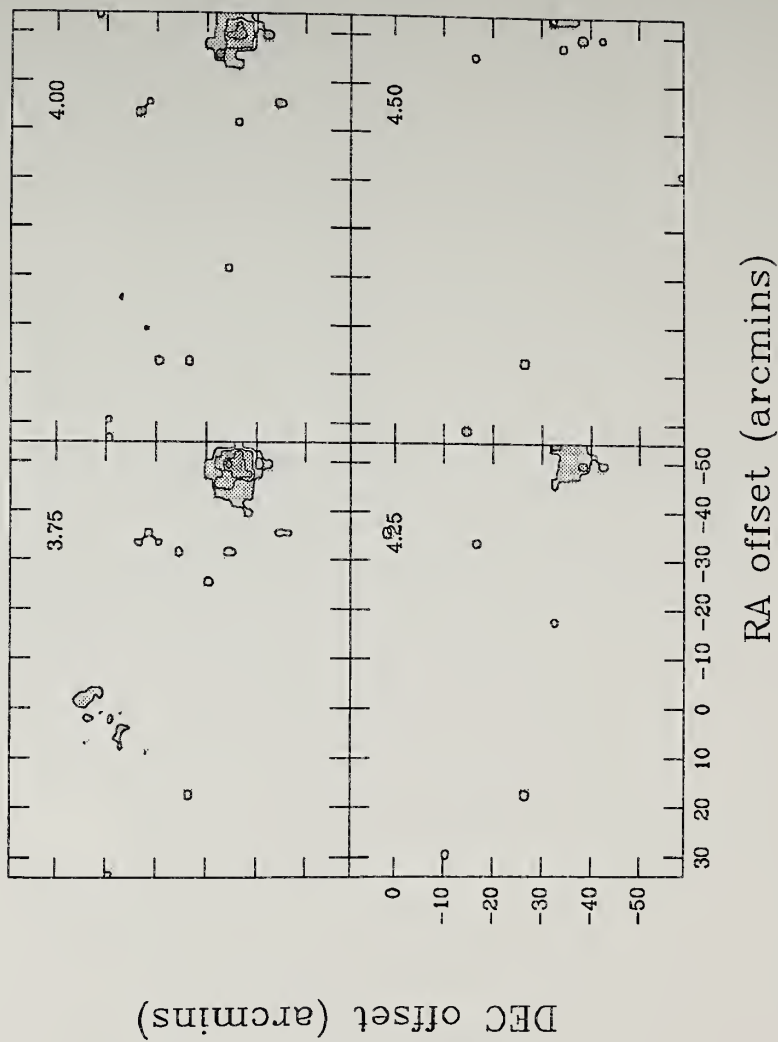
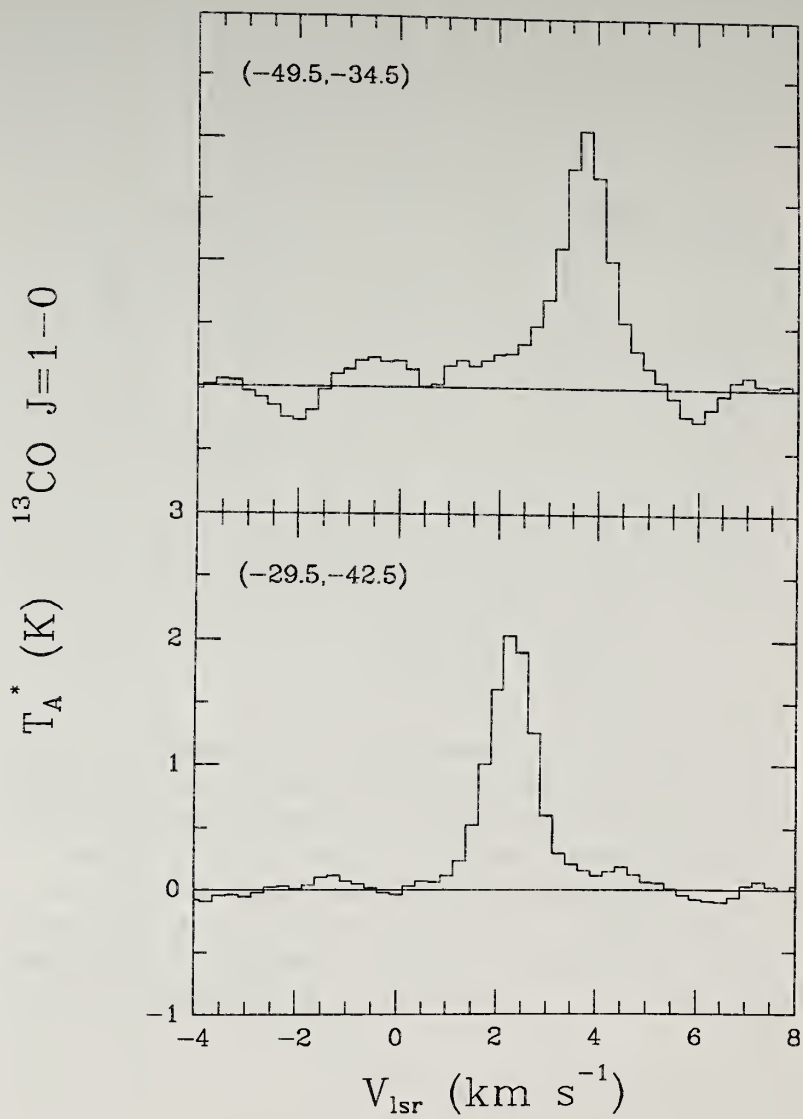


Figure 2.5 ^{13}CO J=1-0 spectra at the low velocity peak and the high velocity peak of the integrated intensity map of the subcloud in region 2. Each profile is the sum of 9 spectra from a 6 by 6' region centered on the indicated position. Shifts in the peak velocity and line asymmetry indicates that this subcloud is rotating.



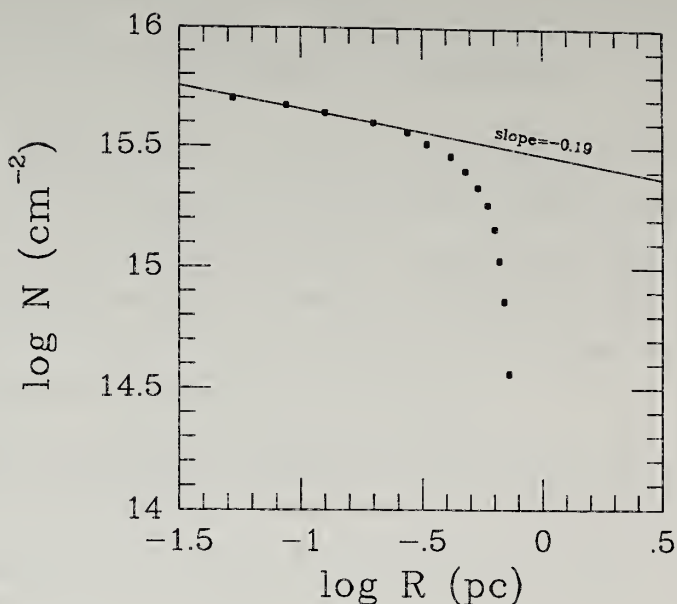


Figure 2.6 The molecular hydrogen density derived from the ^{13}CO J=1-0 column density based on integrated intensity bins as a function of projected radius for a spherically symmetric cloud. A linear fit to the five highest column density points indicates a power law column density decrease with radius at a slope of 0.19, hence a spatial density decrease with a 1.2 power. The sharp cutoff is attributed to both diminished CO excitation and abundance at low densities.

CHAPTER III

OBSERVATIONS OF THE MOLECULAR CORE

The observations of the molecular core of L134N were carried out at the Five College Radio Astronomy Observatory (FCRAO)¹, the National Radio Astronomy Observatory (NRAO)² at Greenbank, West Virginia, and the Haystack Observatory³ in Westford, Massachusetts. Table 3.1 summarizes the seven transitions mapped at the three observatories and lists observational parameters for the maps.

¹The Five College Radio Astronomy Observatory is operated with support from the National Science Foundation and with permission of the Metropolitan District Commission, Commonwealth of Massachusetts.

²The National Radio Astronomy Observatory is operated by Associated Universities, Inc., under contract with the National Science Foundation.

³Radio Astronomy at Haystack Observatory of the Northeast Radio Observatory Corporation is supported by the National Science Foundation.

a) FCRAO

The molecular mapping of the core of L134N was begun at FCRAO by observing the $C^{18}O$ J=1-0 emission. These observations were made in order to acquire a map of an isotope of carbon monoxide which was not optically thick. A map of the CS J=2-1 transition was obtained in

order to augment the CS J=1-0 map of Snell et al. (1982) and improve upon the resolution and sensitivity for a CS map. The H^{13}CO^+ J=1-0 emission line was mapped because the more optically thick HCO^+ J=1-0 emission line suffers from the effects of saturation and self-absorption (Langer et al. 1978). These observations took place during the periods March and April, 1984 and November, 1984 through January, 1985. In June, 1985 a map of the ^{12}CO J=1-0 emission line was obtained primarily to derive an excitation temperature of the core from an optically thick, thermalized species. From the results of the spectral line survey of this region, it was determined that a map of the emission from sulfur monoxide, SO, would exhibit a different morphology than the molecular emissions previously mapped, and a map of the SO N,J=2,3-1,2 emission was obtained in April and May, 1986. These maps, except for the ^{12}CO map, were constructed by position switching the antenna to a reference point eleven arcminutes west and eleven arcminutes north of the nominal reference position; RA = $15^{\text{h}}51^{\text{m}}30^{\text{s}}$, DEC = $-2^{\circ}43'31''$ (1950.0). This position was determined to be free of C^{18}O emission by frequency switching observations. The ^{12}CO map was obtained by frequency switching 5 MHz (13.0 km s^{-1}). Obtaining spectra at one arcminute spacing for the FCRAO observations produced fully sampled maps. During the mapping observations, spectra were periodically taken of the reference position to monitor the stability of the atmosphere.

The positions for the molecular line survey at FCRAO were determined from the integrated intensity peaks of the C^{18}O J=1-0, CS

J=2-1, and H^{13}CO^+ J=1-0 maps, and the NH_3 (1,1) map of Ungerechts, Walmsley, and Winnewisser (1980). This map of NH_3 was used because the FCRAO survey was begun before the map of NH_3 presented in this paper was obtained.

The transitions to observe were selected by the following criteria: (1) observability within the frequency range of the FCRAO receivers; (2) usefulness of the transition in determining the physical or chemical parameters of the cloud; and (3) detectability of the spectral line within a reasonable integration time. Spectra for the FCRAO survey were obtained by either frequency switching or position switching to the position eleven arcminutes north and eleven arcminutes west of the nominal position. Table 3.2 summarizes the transitions observed, date of observations, and relevant system parameters.

The spectra listed in Table 3.2 were obtained with the FCRAO 14 meter radio telescope using the three millimeter cooled heterodyne receiver with a Schottky diode mixer, except for the HC_3N J=5-4 spectra which was obtained with a seven millimeter cooled heterodyne receiver. The backend was a 256 x 100 kHz filterbank with a spectrum expander to provide a spectral resolution of 50 kHz in all but the ^{12}CO observations, in which a spectral resolution of 100 kHz was used. System temperatures ranged from 350 to 1500 K single sideband during the acquisition of data. Pointing, focusing, and relative calibration of the antenna were accomplished by observing standard sources, mainly Saturn and 3C 273, during each observing session. The main beam size,

aperture efficiency, beam efficiency, and forward scattering and spillover efficiency of the 14 meter antenna are give in Table 3.3 for the three millimeter and seven millimeter systems for the epoch of these observations.

The data were calibrated using the standard chopper wheel technique (Penzias and Burris 1973). An ambient load is inserted in front of the telescope feed to determine the antenna temperature, T_A^* , which is corrected for atmospheric losses and some telescope and radome losses. A further correction for spillover losses from a Cassegrain system and forward scattering losses from the antenna and radome is employed by using the correction factor, η_{fss} , the forward scattering and spillover efficiency. This value has been determined at FCRAO by measurements of the Moon and is listed in Table 3.3. Applying the correction, η_{fss} , to the observed antenna temperature produces the radiation temperature, $T_R^* = T_A^* / \eta_{fss}$, which represents the source intensity in temperature units. As suggested by Kutner and Ulich (1981), it will be this quantity which will be reported in this paper. In order to determine the line radiation temperature, T_R , a further correction, for the coupling efficiency, η_c , is necessary ($T_R = T_R^* / \eta_c$). Computation of the coupling efficiency requires a knowledge of how the geometry of the source couples with the telescope beam. Since the extent of L134N is much larger than the beam size, the coupling efficiency will be taken to be unity. Considering the effects of measurement errors and calibration uncertainty, the resulting line temperatures are estimated to be accurate to approximately 10%.

b) NRAO

Observations of the C_3H_2 $J_{K^-K^+}^{-+1} 1_0^{-1} 0_1$ transition were conducted with the 43 m radio telescope of the National Radio Astronomy Observatory at Greenbank, West Virginia in November, 1984. These observations were initiated during a search for interstellar ethynamine (NH_2CCH), when a strong line was detected at 18.343143 GHz, which was later identified as the $J_{K^-K^+}^{-+1} 1_0^{-1} 0_1$ transition of the three-member ring molecule cyclopropenylidene, C_3H_2 (see Matthews and Irvine 1985). The strength of this emission line enabled its mapping with 37 points over the core region of L134N within the available time. Other spectra for the NRAO phase of the survey were obtained with the NRAO 43 m radio telescope during the same observing run. The positions used for the survey at NRAO differ slightly from those used at FCRAO because the NRAO survey was conducted before the FCRAO mapping project was complete.

Observations were carried out in the linear polarization mode with the K-band maser preamplifier and noise tube calibration, which provided system temperatures of 60 to 65 K. The 43 m telescope had a peak aperture efficiency of 0.25, a beam efficiency of 0.33, and a full width half-power beam of 1.65 arcminutes, which are assumed to be constant over the frequency range of the K-band receiver. Spectra were obtained with a 1024 channel autocorrelation spectrometer in a frequency switching mode. For the C_3H_2 and HC_3N spectra a bandwidth of

10 MHz was used. For the observations of both NH_3 and C_4H , the autocorrelator was split into two ranges of 5 MHz bandwidth each, allowing simultaneous observations of two transitions. All spectra were corrected for antenna gain vs. hour angle and atmospheric attenuation. For these observations, the line radiation temperature, T_R^* , will be taken to be T_A / η_{MB} , due to the lack of a measurement of the forward scattering and spillover coefficient for an extended source with the 43 m telescope beam. Since the main beam efficiency and the forward scattering coefficient are not the same quantity, the FCRAO and NRAO data are not calibrated in an identical manner. However, comparisons of these efficiencies for the 14 m telescope (see Table 3.3) suggest that this difference would not be a significant source of error in comparisons of observations between the two telescopes. Table 3.4 lists the NRAO survey observational parameters.

At the time of the observations a new subreflector had just been installed on the 43 m telescope and had only been provisionally adjusted. As a result, the absolute calibration of the intensities of the spectra may be in error by as much as 30%; however the relative intensities should be accurate, especially for the simultaneous observations with a split autocorrelator. The relative intensity within the map points should also be accurate.

c) Haystack

A map of the NH_3 J,K=1,1 emission line at 23.6944955 GHz was constructed using data taken with the 37 m radio telescope of the Haystack Observatory during March and April, 1985. The receiver used was a cooled K-band maser preamplifier and a 1024 channel autocorrelator with a 4.444 MHz bandwidth, which was wide enough to include all the hyperfine lines in a single spectra. This configuration yielded a spectral resolution of 0.082 km s^{-1} . Data were taken in the frequency switching mode with a switching interval of 18 channels (1.24 km s^{-1}). The spectra were calibrated with a noise tube and typical system temperatures were 100 to 200 K. Telescope pointing was monitored by observing Saturn, and all spectra were corrected for the effects of atmospheric attenuation and telescope gain as a function of elevation by the standard Haystack efficiency curves. At this frequency the aperture efficiency of the 37 m radio telescope is 0.22 and the main beam efficiency is 0.25. The line radiation temperature, T_R^* , will be assumed to be the main beam antenna temperature, $T_{MB} = T_A / \eta_{MB}$. The spectra which form the map were observed with a spacing of one arcminute, so with the antenna main beam size of 1.4 arcminutes the NH_3 map is oversampled.

TABLE 3.1

L134N MAPPING SUMMARY

transition	frequency	spectral resolution	beam size	# of map points	spacing	peak S/N
	(GHz)	(km s ⁻¹)	(")		(')	
C ¹⁸ O J=1-0	109.782182	0.14	48.	161	1	12.7
CS J=2-1	97.981007	0.15	54.	180	1	12.3
H ¹³ CO ⁺ J=1-0	86.754330	0.17	60.	183	1	8.2
SO N, J=2,3-1,2	99.299867	0.15	53.	168	1	14.4
NH ₃ J, K=1, 1	23.6944955	0.082	80.	143	1	14.1
C ₃ H ₂ J _{K⁻K⁺=1₁₀⁻¹₀₁}	18.343143	0.16	99.	37	2	23.1
¹² CO J=1-0	115.271203	0.26	46.	255	1	11.9

TABLE 3.2

FCRAO MOLECULAR SURVEY OBSERVATIONAL PARAMETERS

date(s)	molecule	transition	frequency (GHz)	mode ^a	spectral ^b resolution (km s ⁻¹)
1985 JAN 31, FEB 19	C ³⁴ S	J=2-1	96.412953	FS	0.16
1985 FEB 19, MAR 20	H ¹³ CO ⁺	J=1-0	86.754330	FS	0.17
1985 FEB 21	CS	J=2-1	97.981007	FS	0.15
1985 FEB 21	C ¹⁸ O	J=1-0	109.782182	FS	0.14
1985 MAR 13, 14	HN ¹³ C	J=1-0	87.090851	FS	0.17
1985 MAR 14, 19	H ¹³ CN	J=1-0	86.340184	PS	0.17
1985 APR 11, 13	SO ₂	J _{K⁻K⁺} =3 ₁₃ -2 ₀₂	104.029398	FS	0.14
1985 APR 18	HC ₃ N	J=5-4	45.490316	PS	0.33
1985 APR 22	OCS	J=7-6	85.139081	FS	0.18
1985 APR 23	SO	N, J=2, 2-1, 1	86.093969	FS	0.17
1985 MAY 2	N ₂ H ⁺	J=1-0	93.173700 ^C	PS	0.16
1985 MAY 3	HC ₃ N	J=9-8	81.881458	FS	0.18
1985 MAY 20	C ₃ H ₂	J _{K⁻K⁺} =2 ₁₂ -1 ₀₁	85.33885	FS	0.18
1985 MAY 20, JUN 10	HCS ⁺	J=2-1	85.34790	FS	0.18
1985 JUN 25	¹² CO	J=1-0	115.271203	FS	0.26
1986 APR 14, 15	SO	N, J=2, 3-1, 2	99.299867	PS	0.15
1986 JUN 1, 25	³⁴ SO	N, J=2, 3-1, 2	97.71539	FS	0.15
1986 JUN 26	HC ¹⁸ O ⁺	J=1-0	85.162157	FS	0.18

notes to Table 3.2:

- a FS = frequency switch; PS = position switch
- b all spectra have a resolution of 50 kHz except for ^{12}CO which has a resolution of 100 kHz
- c correct $F_1=2-1$ frequency = 93.17358 GHz (Turner and Thaddeus 1977)

TABLE 3.3

FCRAO ANTENNA PERFORMANCE*

frequency (GHz)	beam size (arcsec)	η_a	η_b	η_{fss}
43.4	121	0.48	0.58	0.59
84.8	60.4	0.47	0.56	0.68
114.9	45.9	0.43	0.51	0.70

* includes radome losses (Shell 1985)

TABLE 3.4

NRAO MOLECULAR SURVEY OBSERVATIONAL PARAMETERS

molecule	transition	frequency	spectral resolution
		(GHz)	(km s ⁻¹)
C ₃ H ₂	J _{K⁻ K⁺ +1} 1 ₀ ⁻¹ 0 ₁	18.343143	0.16
HC ₃ N	J=2-1	18.196312	0.16
NH ₃	J, K=1, 1	23.694494	0.12
NH ₃	J, K=2, 2	23.722633	0.12
C ₄ H	N, J, F=2, 3/2, 1-1, 1/2, 0	19.054476	0.15
C ₄ H	N, J, F=2, 5/2, 3-1, 3/2, 2	19.015142	0.15

CHAPTER IV

MOLECULAR MAPPING AND SPECTRAL LINE SURVEY RESULTS

a) mapping

The results of the mapping of the core region of L134N are presented in Figures 4.1 to 4.3. In figure 4.1 the region of the core mapped is enclosed in a box within the larger map of ^{13}CO J=1-0. This ^{13}CO map is a subset of the more extended map of Chapter II. In Figures 4.2 a-f, maps of the integrated intensity across the emission line are presented for C^{18}O J=1-0; CS J=2-1; H^{13}CO^+ J=1-0; SO N,J=2,3-1,2; NH_3 J,K=1,1; and C_3H_2 J_K⁻ K⁺ 1₀-1₀₁; respectively. The well defined core seen in these maps is not apparent from the ^{13}CO integrated intensity map of Figure 4.1. Previous work (e.g., Dickman 1978; Frerking, Langer, and Wilson 1982; and Heyer et al. 1987) has shown that the ^{13}CO integrated intensity correlates well with the visual extinction, therefore with molecular column density, and is not sensitive to dense cores. Hence, observations of ^{13}CO J=1-0 are not as useful as a means of tracing high density cores in nearby dark clouds as are observations of other species. Each map in Figure 4.2 is presented on the same scale although not all maps cover the full extent of the area shown. The spatial coordinates are represented in offsets in minutes of arc from the reference position RA = 15^h 51^m 30^s and

DEC = $-2^{\circ}43'31''$ (1950.0). Figure 4.3 shows the ^{12}CO peak antenna temperatures across the core region. Individual spectra for each transition mapped are exemplified by the molecular survey results.

1) C^{18}O

The map of the Integrated Intensity of C^{18}O in the core region of L134N indicates a double peaked structure with one peak in the east and the other in the northwest edge of the extent of emission. In general, the map is relatively uniform without any steep intensity gradients. Individual spectra which constitute the C^{18}O map are mostly single peaked without any indication of a systematic velocity structure. Examples of C^{18}O J=1-0 spectra are shown in Figure 4.6. Some of the spectra indicate an extended high velocity line wing which will be discussed later.

A characteristic size for the map can be obtained from the square root of the area which contains spectra with integrated intensities greater than one half the peak value of the integrated intensity. This mean full width at half intensity of the C^{18}O emission is 7.9 arcminutes, which corresponds to 0.32 parsec at the distance of L134N of 160 parsecs (Snell 1981).

11) CS

A map of the integrated intensity of the CS J=2-1 emission is shown in Figure 4.2b. The integrated intensity map has a peak which corresponds roughly to the eastern C¹⁸O peak, but the peak in the western edge lies north and east of the northwestern C¹⁸O peak. This map is very similar to the CS J=1-0 map of Snell *et al.* (1982). The mean full width at half intensity of the CS emission is about 5.9 arcminutes (0.28 parsecs).

Examples of the individual spectra of the CS J=2-1 transition in Figure 4.7 show the effects of self-absorption by lower excitation foreground material. The fact that the self-absorption feature occurs at approximately 2.5 km s⁻¹, the local standard of rest velocity of the cloud as determined from other observed species, indicates that this is indeed self-absorption and not separate emission lines from two velocity components of the cloud core. The self-absorption may have considerably altered the appearance of the CS map, and the true CS distribution may be better represented by the C³⁴S survey spectra in Figure 4.8. In addition, the CS J=1-0 map of Snell *et al.* (1982), in which the individual spectra are not as strongly self-absorbed, shows an northwestern peak more aligned with the northwestern peak of the C¹⁸O J=1-0 map. The eastern peak of the CS J=1-0 map, which is consistent with the C¹⁸O J=1-0 eastern peak, is approximately one arcminute east of the peak in the CS J=2-1 map.

III) H^{13}CO^+

Figure 4.2c shows a map of H^{13}CO^+ J=1-0 emission, which is similar to the lower spatial resolution H^{13}CO^+ J=1-0 map of Guellin, Langer, and Wilson (1982). The integrated intensity map indicates a north-south ridge of emission with an extension on the western side and is distinctly different from the C^{18}O and CS maps. A sharp peak in the integrated intensity occurs in the northern region of the cloud (approximately at position (1,3)) which is not apparent in either the C^{18}O or CS map. The emission peak in the southern region shows weaker, but broader spectra (hence comparable integrated intensities) and is at a lower velocity than the rest of the core. This southern peak is not as evident in the maps of other species. The mean full width half intensity of the H^{13}CO^+ J=1-0 map is determined to be about 5.3 arcminutes neglecting the far southern peak.

Examples of the H^{13}CO^+ J=1-0 individual spectra in Figure 4.10 show no signs of self-absorption. This is not true of the HCO^+ spectra observed by Guellin, Langer, and Wilson (1982). The observed HC^{18}O^+ J=1-0 spectra indicate that the H^{13}CO^+ J=1-0 transition is optically thin (see Chapter V) and may be sampling a deeper region of the core than the more optically thick C^{18}O J=1-0 and CS J=2-1 transitions. The singly peaked spectra of the H^{13}CO^+ map do not show any indication of velocity structure within the main region of the L134N core.

IV) SO

A map of the integrated intensity of the SO N,J=2,3-1,2 transition is presented in Figure 4.2d. The SO integrated emission peaks in the area of the H^{13}CO^+ western extension and does not show strong emission at the location of the H^{13}CO^+ northern peak. The SO peaks do not correspond with either the peaks in the C^{18}O or CS maps. SO emission extends somewhat to the south, but does not show the strong southern peak exhibited by H^{13}CO^+ . This distribution of emission is unique with respect to the rest of the maps in this study. The mean full width at half intensity of the SO map is 5.1 arcminutes.

As with the CS J=2-1 spectra, some of the mapped SO N,J=2,3-1,2 spectra show self-absorption indicating that this transition suffers from absorption by a lower excitation foreground gas along certain lines of sight. However, from observations of optically thin SO and ^{34}SO transitions, which will be discussed later, the effect of self-absorption in the SO N,J=2,3-1,2 emission does not seem to alter the positions of the peak intensities and cannot explain the uniqueness of the SO distribution. In addition, these observations of more optically thin transitions of SO indicate that the N,J=2,3-1,2 transition is optically thick.

v) NH_3

A map of the NH_3 (1,1) inversion transition is presented in Figure 4.2e. In this case, only the integrated intensity of the main electric quadrupole hyperfine component is mapped. The integrated intensity map is similar in morphology to the H^{13}CO^+ map in that there is a strong peak in the north and both show the same general north-south ridge structure. However, the ammonia map clearly shows a strong second peak to the south and slightly west of the slightly more dominant northern integrated emission peak. This distribution of the integrated intensity in this map follows closely that of the NH_3 (1,1) map of Ungerechts, Walmsley, and Winnewisser (1980). However, the spectra of the map presented here do not indicate the velocity structure within the core as suggested by Ungerechts, Walmsley, and Winnewisser. The NH_3 (1,1) intensities are more sharply peaked in the ridge center and fall off more rapidly than any other of the mapped distributions. The full width half intensity in the north-south direction is 8.0 arcminutes and in the east-west direction is 2.0, for a mean full width half intensity of 4.2 arcminutes. Ammonia has the most narrow emission distribution of the species mapped.

vi) C_3H_2

The C_3H_2 map is shown in Figure 4.2f. C_3H_2 has a distribution similar to that of NH_3 , although the full width half intensity of 5.1 arcminutes for the C_3H_2 map is greater than that of NH_3 (1,1). There

is a single peak which corresponds well with the northern integrated intensity peak observed in the H^{13}CO^+ and NH_3 distributions, but there is not a second peak as observed in NH_3 . The individual C_3H_2 spectra, some of which are shown in Figure 4.25, are very narrow and do not indicate any velocity structure within the core.

vii) ^{12}CO

Figure 4.3 shows a map of the peak line temperature, T_R^* , of the ^{12}CO J=1-0 line. This map does not cover the full extent of the ^{12}CO emission, but only the area mapped in the other species, and does not show evidence for the presence of the dense core. Across the region mapped there appears to be an intensity gradient in the ^{12}CO emission from northwest to southeast, similar to the ^{13}CO intensity distribution. In addition, this map compares well with the more extended ^{12}CO map of Snell (1981), which shows that the ^{12}CO emission peaks to the south of the region mapped in this study. If the ^{12}CO is assumed to be thermalized, the map of the peak intensity follows the ^{12}CO excitation temperature.

b) survey

i) FCRAO

The positions observed in the FCRAO survey were chosen from integrated intensity peak positions of maps which had been obtained

when the survey observations began. The positions surveyed are: (0.6,2.9) based on the NH_3 map of Ungerechts, Walmsley, and Winnewisser (1980) and the H^{13}CO^+ map; (0.7,0.7) based on NH_3 ; (-0.8,0.4) and (-2.3,2.0) based on the CS map; (-2.8,0.8) and (3.7,-1.2) based on the C^{18}O map; and (-1.4,-0.8) based on the H^{13}CO^+ map. All coordinate pair offsets are in arcminutes and are referenced to the position $\text{RA} = 15^{\text{h}}51^{\text{m}}30^{\text{s}}$, $\text{DEC} = -2^{\circ}43'31''$ (1950.0) and these positions are indicated in Figure 4.4. Spectra obtained in the FCRAO molecular survey are presented in Figures 4.5 to 4.22. Each figure shows spectra for a particular transition at the positions observed. Positions for the FCRAO survey are labeled: a (0.6,2.9); b (0.7,0.7); c (-0.8,0.4); d (-1.4,-0.8); e (-2.8,0.8); f (-2.3,2.0); g (3.7,-1.2).

The ^{12}CO J=1-0 spectra in Figure 4.5 are broader and not as sharply peaked as other spectra in the survey as evidenced when they are compared to the C^{18}O J=1-0 spectra in Figure 4.6. Although the C^{18}O spectra do not show a high degree of variation over the seven surveyed positions, both the C^{18}O and the ^{12}CO have their greatest intensity at the (3.7,-1.2) position in the southeast region of the dense core. Some C^{18}O spectra have broader line wings on the high velocity side which may be indicative of large scale motions (Myers 1980).

The CS J=2-1 spectra in Figure 4.7 show self-absorption and high velocity wings. The self-absorption may mask the true CS distribution, which may be more accurately represented by the optically thin C^{34}S

J=2-1 spectra of Figure 4.8. Even the $C^{34}S$ spectra indicate significant column density at the (3.7,-1.2) position at which only CO and CS seem to have high relative intensities. The weak HCS^+ J=2-1 spectra in Figure 4.9 may also trace the CS distribution within the dense core.

$H^{13}CO^+$ J=1-0 spectra presented in Figure 4.10 show a peak at the (0.6,2.9) position which is the peak of many molecular species which result from hydrocarbon chemistry. However, $H^{13}CO^+$ is still intense at the (-1.4,-0.8) position in the western edge of the core where these other hydrocarbon species are not. A $H^{13}CO^+$ J=1-0 spectra at the (-2.3,2.0) position was not obtained. A single $HC^{18}O^+$ J=1-0 spectra, shown in Figure 4.11, was obtained at the (0.6,2.9) position which determined that $H^{13}CO^+$ J=1-0 is optically thin even at its most intense position (see Chapter V).

Figures 4.12 through 4.16 show observed spectra of $H^{13}CN$ J=1-0, $HN^{13}C$ J=1-0, HC_3N J=5-4 and J=9-8, and C_3H_2 $2_{12}-1_{01}$; all of which seem to follow the same distribution. They are peaked at the (0.6,2.9) position and their intensity decreases with distance from that position. All of these species are a result of hydrocarbon chemistry suggesting that other such species would exhibit the same morphology. The N_2H^+ J=1-0 spectra shown in Figure 4.17 indicate that N_2H^+ is also strong at the (0.6,2.9) position but peaks at the (0.7,0.7) position, and perhaps has a distribution similar to that shown by the NH_3 (1,1)

map. As will be seen in Chapter VI, N_2H^+ and NH_3 may be chemically related.

Figures 4.18 through 4.21 show the SO $N, J=2,3-1,2$ and $N, J=2,2-1,1$, ^{34}SO $N, J=2,3-1,2$, and SO_2 $3_{13}-2_{02}$ spectra. These four transitions all indicate a peak at the $(-1.4, -0.8)$ position as demonstrated by the SO map. This distribution is unique from the other species observed. The SO $N, J=2,3-1,2$ spectra in Figure 4.18 show high velocity line wings similar to those exhibited by $C^{18}O$ $J=1-0$ and CS $J=2-1$ transitions all of which are shown in Chapter V not to be optically thin. Hence, these transitions may have contributions from a lower density envelope surrounding the dense core. The OCS $J=7-6$ spectrum shown in Figure 4.22 was observed only at the SO peak because it was believed to be chemically related to SO , and therefore that would be the best position to search.

The results of the FCRAO survey are tabulated in Table 4.1. Table 4.1a lists the molecule and transition observed; the position within the L134N core observed; the radiation temperature, T_R^* ; integrated intensity, $\int T_R^* dv$; the full width half-power velocity of the line, FWHP; and the velocity with respect to the local standard of rest of the centroid of the line, V_{LSR} ; for the transitions without hyperfine components. The values in parenthesis after the last four quantities are one-sigma errors. In the case where a line was detected, the quantities reported are the result of a Gaussian fit to the line. Non-

detection upper limits from the noise root-mean-square (rms) are listed as the one-sigma error in the radiation temperature.

In the FCRAO survey two of the transitions observed have hyperfine structure due to the $I=1$ spin of the ^{14}N nucleus. In the case of H^{13}CN ($J=1-0$) the results of Gaussian fits are listed in Table 4.1b for each of the three hyperfine components. Figure 4.12 shows the H^{13}CN spectra for the three positions observed. The results of Gaussian fitting for four of the seven observed N_2H^+ spectra obtained at FCRAO are listed in Table 4.1c. As shown in Figure 4.17 the N_2H^+ spectrum is complicated by the multiple splitting of the lines from hyperfine structure resulting from the $I=1$ nuclear spin of both ^{14}N atoms. Only the integrated intensities of the $F_1=J+i$ transitions for the three remaining positions are reported in Table 4.1c since they are the only marginal detections. The spectra in Figure 4.17 are based on a rest frequency for the $F=1-2$ transition of 93.17370 GHz (Saykally et al., 1976). However, Turner and Thaddeus (1977) revise this frequency to 93.17358 ± 0.00028 GHz based on high resolution observations of quiescent clouds. The Turner and Thaddeus frequency provides better agreement with the theoretical hyperfine splitting frequencies for the $F=1-1$ and $F=1-0$ lines, and the V_{LSR} of the Gaussian fits to the hyperfine components were adjusted to reflect this revised frequency. The value listed under the V_{LSR} total column is the V_{LSR} of the unsplit N_2H^+ $J=1-0$ rest frequency of 93.17330 GHz calculated from the theoretical hyperfine splitting values from Townes and Schawlow (1955).

11) NRAO

The positions used for the NRAO survey were selected before the FCRAO mapping project was complete and differ slightly from those used in the FCRAO survey. The positions chosen for the NRAO survey are (0,0), the nominal reference position; (-2,-1), (-3,1), (4,-1), and (0,2) based on a preliminary $C^{18}O$ map; (1,1) and (1,3) based on the NH_3 map of Ungerechts, Walmsley, and Winnewisser (1980). These positions are indicated along with the FCRAO survey positions in Figure 4.4. Also HC_3N J=2-1 was observed at the (0.6,3.3) position to compare with the observation of Churchwell, Nash, and Walmsley (1984). Again the coordinate pairs are offsets in units of arcminutes and are referenced to the position $RA = 15^h 51^m 30^s$, $DEC = -2^{\circ} 43' 31''$ (1950.0). Spectra obtained in the NRAO survey are presented in Figures 4.22 to 4.28. Positions for the NRAO survey are labeled: a (1,3); b (1,1); c (0,2); d (0,0); e (-2,-1); f (-3,1); g (4,-1).

Figures 4.23 and 4.24 show the NH_3 (1,1) and NH_3 (2,2) spectra simultaneously observed. The intensity distribution from the surveyed spectra follow closely the distribution from the NH_3 map, except for the (1,1) position which is anomalously weak in the surveyed NH_3 spectra, as seems to be the case for all other NRAO survey spectra at the (1,1) position. Figures 4.25 through 4.28 show the C_3H_2 $1_{10}-1_{01}$, HC_3N J=2-1, and C_4H N=2-1, F=3-2 and F=2-1 spectra. These all follow the intensity distribution indicated by the C_3H_2 map and FCRAO surveyed hydrocarbon species. The HC_3N J=2-1 spectra observed at the (0.6,3.3)

position and shown in Figure 4.29 has a greater intensity than observed at the (1,3) position which may indicate a sharply peaked nature for the emission.

The results of the NRAO survey are tabulated in Table 4.2a. As in Table 4.1a, Table 4.2a lists the molecule and transition observed, the position within the L134N core that was observed, the radiation temperature, integrated intensity, full width half-power velocity of the line, and the velocity with respect to the local standard of rest of the centroid of the line. Except where indicated by an asterisk, the values listed in Table 4.2a are the results of a Gaussian fit to the observed line profile.

The NH_3 (1,1) results are tabulated in Table 4.2b. Each of the NH_3 (1,1) spectra in the NRAO survey was fit by a function of eleven Gaussians which represented the eleven of the eighteen hyperfine components whose local thermodynamic equilibrium (LTE) relative intensities would predict an absolute peak intensity greater than the rms noise of the spectra. The fitting function had twenty-three free parameters; the peak intensity and velocity of each of the eleven hyperfine line plus one line width common to all components. The LTE relative intensities and positions were taken from Ungerechts, Walmsley, and Winnewisser (1980). In the case of all seven spectra, the $F_1=1-1$, $F=3/2-3/2$ line was not properly fit indicating a nondetection, despite the fact that other components with smaller LTE relative intensities were fit. Also, the $F_1=2-2$, $F=3/2-3/2$ line, which

is the secondary component of the main electronic quadrupole group, was fit to a higher V_{LSR} than predicted by Ungerechts, Walmsley, and Winnewisser by $0.07 \pm 0.04 \text{ km s}^{-1}$ in all seven cases. The nondetection of $F_1=1-1$, $F=3/2-3/2$ line means each electric quadrupole group was fit by two Gaussian components and the values of T_{R}^* , V_{LSR} , and line width listed in Table 4.2b are the results of this fitting. The listed value for the total V_{LSR} is the average of the ten fitted lines weighted by the relative intensity of the hyperfine line.

For a comparison with the FCRAO survey, Table 4.2c contains the line parameters for the $\text{C}_3\text{H}_2 \text{ J}_{\text{K}^-\text{K}^+} = 1_{10}^{-1} 0_1$ transition at the FCRAO survey positions as interpolated from the NRAO map.

c) discussion

Some maps, such as NH_3 , H^{13}CO^+ , and C_3H_2 , are similar, but others, such as C^{18}O , CS, and SO, are strikingly different with respect to these and each other. Certain CS and SO spectra suffer self-absorption and have high velocity line wings, which may indicate that they are probing outer regions of the core where there are large scale motions; while spectra which are narrow and symmetric seem to probe into the core peak near position (0.6,2.9) indicating they emanate from a very quiescent region. Infrared observations by Snell (1981), Sargent *et al.* (1983), and the Infrared Astronomical Satellite (IRAS) (1985) show no indication of any infrared sources within the core region which may be affecting the distribution of molecular material. Hence, the

differences in distributions must be attributed to either different physical conditions, such as temperature, number density, or molecular column density, varying the excitation of the molecular emission or a chemical abundance difference within different regions of the core. In order to investigate these possibilities, the results of the mapping and survey will be used to determine physical conditions within the core and will be examined in the context of chemical models of the gas phase chemistry of dark clouds.

Table 4.3 lists molecular parameters of the transitions observed in both surveys. Listed are the molecule and transition observed; the rest frequency of the line; the rotational constants, B_0 ; the centrifugal distortion constant, D_0 ; the hyperfine splitting constant, eQq ; the dipole moment, μ ; the Einstein coefficient for spontaneous emission for the transition, A_{ul} ; the line strength of the transition, S ; a constant of proportionality between the integrated intensity of the line and the column density of the upper level of the transition in the optically thin limit, q_v ; the critical density for excitation which is obtained by balancing collisional rates with the Einstein spontaneous emission rate, n^* ; and the energy of the upper level of the transition in Kelvin, T_u . These parameters will be used in later calculations and are tabulated here for completeness.

TABLE 4.1a
FCRAO OBSERVATIONAL RESULTS

transition	position	T_R^* (K)	$\int T_R^* dv$ (K km s ⁻¹)	FWHM (km s ⁻¹)	V_{LSR} (km s ⁻¹)
¹² CO J=1-0	(0.6, 2.9)	5.02(0.35)	9.82(0.40)	1.84(0.15)	2.16(0.78)
	(0.7, 0.7)	5.70(0.45)	15.18(0.51)	2.50(0.21)	2.51(1.06)
	(-0.8, 0.4)	5.53(0.33)	13.26(0.38)	2.26(0.15)	2.34(0.96)
	(-1.4, -0.8)	5.27(0.41)	11.89(0.47)	2.12(0.19)	2.41(0.90)
	(-2.8, 0.8)	5.57(0.38)	10.25(0.44)	1.73(0.14)	2.23(0.73)
	(-2.3, 2.0)	5.17(0.38)	10.14(0.44)	1.84(0.16)	2.39(0.78)
(3.7, -1.2)	7.72(0.35)	13.98(0.40)	1.70(0.09)	2.05(0.72)	
¹³ CO J=1-0	(0.6, 2.9)	1.96(0.15)	1.05(0.10)	0.51(0.06)	2.47(0.21)
	(0.7, 0.7)	2.25(0.10)	1.20(0.07)	0.50(0.04)	2.53(0.21)
	(-0.8, 0.4)	2.14(0.15)	1.41(0.10)	0.62(0.06)	2.55(0.26)
	(-1.4, -0.8)	2.42(0.12)	1.55(0.08)	0.60(0.04)	2.54(0.25)
	(-2.8, 0.8)	2.01(0.15)	1.20(0.09)	0.56(0.06)	2.48(0.24)
	(-2.3, 2.0)	1.37(0.12)	1.33(0.08)	0.91(0.09)	2.55(0.39)
(3.7, -1.2)	2.68(0.09)	1.85(0.06)	0.65(0.03)	2.40(0.27)	
CS J=2-1	(0.6, 2.9)	0.77(0.06)	0.61(0.04)	0.74(0.07)	2.66(0.32)
	(0.7, 0.7)	0.61(0.06)	0.71(0.04)	1.09(0.12)	2.78(0.46)
	(-0.8, 0.4)	0.88(0.06)	1.04(0.04)	1.10(0.09)	2.76(0.47)
	(-1.4, -0.8)	0.89(0.06)	0.91(0.04)	0.96(0.08)	2.74(0.41)
	(-2.8, 0.8)	0.91(0.06)	0.77(0.04)	0.79(0.06)	2.71(0.33)
	(-2.3, 2.0)	0.94(0.06)	1.04(0.04)	1.04(0.08)	2.72(0.44)
(3.7, -1.2)	0.86(0.08)	0.70(0.05)	0.76(0.09)	2.63(0.32)	
³⁴ S J=2-1	(0.6, 2.9)	0.19(0.03)	0.11(0.02)	0.53(0.14)	2.49(0.23)
	(0.7, 0.7)	0.21(0.04)	0.14(0.03)	0.64(0.20)	2.51(0.27)
	(-0.8, 0.4)	0.08(0.04)	0.04(0.03)	0.51(0.39)	2.56(0.22)
	(-1.4, -0.8)	0.17(0.03)	0.09(0.02)	0.50(0.13)	2.47(0.21)
	(-2.8, 0.8)	0.19(0.03)	0.14(0.02)	0.67(0.16)	2.47(0.29)
	(-2.3, 2.0)	0.07(0.03)	0.03(0.02)	0.39(0.30)	2.56(0.17)
(3.7, -1.2)	0.16(0.03)	0.07(0.02)	0.41(0.12)	2.40(0.18)	
HCS ⁺ J=2-1	(0.6, 2.9)	0.13(0.04)	0.09(0.03)	0.67(0.28)	2.37(0.28)
	(0.7, 0.7)	0.16(0.03)	0.11(0.02)	0.62(0.16)	2.59(0.26)
	(-0.8, 0.4)	0.18(0.04)	0.07(0.03)	0.37(0.17)	2.53(0.16)
	(-1.4, -0.8)	0.16(0.04)	0.07(0.03)	0.43(0.23)	2.57(0.18)
	(-2.8, 0.8)	0.27(0.05)	0.16(0.04)	0.55(0.16)	2.63(0.23)
	(-2.3, 2.0)	0.09(0.04)	0.04(0.03)	0.49(0.39)	2.25(0.21)
(3.7, -1.2)	0.08(0.04)	0.10(0.03)	1.26(0.83)	2.65(0.53)	

H^{13}CO^+ J=1-0	(0.6, 2.9)	1.20(0.08)	0.61(0.06)	0.48(0.06)	2.55(0.20)
	(0.7, 0.7)	1.04(0.05)	0.79(0.04)	0.71(0.05)	2.56(0.30)
	(-0.8, 0.4)	0.66(0.08)	0.35(0.05)	0.50(0.09)	2.60(0.21)
	(-1.4, -0.8)	0.66(0.06)	0.42(0.04)	0.60(0.08)	2.56(0.26)
	(-2.8, 0.8)	0.22(0.04)	0.11(0.03)	0.48(0.15)	2.54(0.20)
	(3.7, -1.2)	0.19(0.04)	0.11(0.03)	0.53(0.18)	2.51(0.22)
HC^{18}O^+ J=1-0	(0.6, 2.9)	0.16(0.04)	0.08(0.03)	0.47(0.19)	2.20(0.20)
HN^{13}C J=1-0	(0.6, 2.9)	0.81(0.05)	0.49(0.04)	0.56(0.06)	2.46(0.24)
	(0.7, 0.7)	0.63(0.06)	0.47(0.04)	0.69(0.08)	2.49(0.29)
	(-0.8, 0.4)	0.32(0.05)	0.25(0.04)	0.72(0.17)	2.66(0.31)
	(-1.4, -0.8)	0.22(0.06)	0.10(0.05)	0.42(0.23)	2.41(0.18)
	(-2.8, 0.8)	... (0.07)
	(-2.3, 2.0)	0.10(0.06)	0.04(0.05)	0.35(0.49)	2.66(0.15)
	(3.7, -1.2)	0.09(0.06)	0.04(0.04)	0.43(0.54)	2.67(0.18)
HC_3N J=5-4	(0.6, 2.9)	1.62(0.19)	1.20(0.19)	0.70(0.13)	2.50(0.30)
	(0.7, 0.7)	1.20(0.17)	0.66(0.17)	0.52(0.15)	2.46(0.22)
	(-0.8, 0.4)	0.62(0.18)	0.53(0.18)	0.81(0.37)	2.34(0.35)
	(-1.4, -0.8)	0.61(0.18)	0.52(0.18)	0.80(0.37)	2.58(0.34)
	(-2.8, 0.8)	0.31(0.14)	0.35(0.14)	1.06(0.62)	2.27(0.45)
	(-2.3, 2.0)	... (0.29)
	(3.7, -1.2)	... (0.16)
HC_3N J=9-8	(0.6, 2.9)	0.65(0.05)	0.22(0.04)	0.31(0.06)	2.36(0.13)
	(0.7, 0.7)	0.34(0.07)	0.15(0.05)	0.41(0.16)	2.34(0.17)
	(-0.8, 0.4)	... (0.06)
C_3H_2 $2_{12}^{-1}0_1$	(0.6, 2.9)	1.44(0.07)	0.63(0.05)	0.41(0.04)	2.28(0.17)
	(0.7, 0.7)	1.21(0.09)	0.68(0.06)	0.53(0.06)	2.21(0.22)
	(-0.8, 0.4)	0.85(0.08)	0.38(0.06)	0.42(0.07)	2.29(0.18)
	(-1.4, -0.8)	0.52(0.09)	0.23(0.06)	0.41(0.14)	2.27(0.18)
	(-2.8, 0.8)	0.24(0.13)	0.21(0.09)	0.79(0.54)	2.49(0.34)
	(-2.3, 2.0)	0.23(0.10)	0.11(0.07)	0.44(0.36)	2.46(0.19)
	(3.7, -1.2)	... (0.08)
SO 2, 2-1, 1	(0.6, 2.9)	0.21(0.10)	0.08(0.07)	0.36(0.36)	2.45(0.15)
	(0.7, 0.7)	0.72(0.07)	0.37(0.05)	0.49(0.08)	2.49(0.21)
	(-0.8, 0.4)	0.70(0.09)	0.32(0.06)	0.43(0.10)	2.55(0.18)
	(-1.4, -0.8)	0.92(0.07)	0.51(0.05)	0.52(0.07)	2.42(0.22)
	(-2.8, 0.8)	0.26(0.10)	0.07(0.07)	0.26(0.28)	2.48(0.11)
	(-2.3, 2.0)	... (0.16)
	(3.7, -1.2)	... (0.08)

SO 2,3-1,2	(0.6,2.9)	1.44(0.09)	0.74(0.06)	0.48(0.05)	2.41(0.20)
	(0.7,0.7)	1.37(0.08)	0.99(0.05)	0.68(0.05)	2.42(0.29)
	(-0.8,0.4)	1.80(0.07)	1.79(0.05)	0.93(0.04)	2.50(0.40)
	(-1.4,-0.8)	2.00(0.07)	1.63(0.05)	0.76(0.03)	2.41(0.32)
	(-2.8,0.8)	1.39(0.08)	1.05(0.05)	0.71(0.05)	2.46(0.30)
	(-2.3,2.0)	1.02(0.08)	0.85(0.05)	0.79(0.08)	2.57(0.33)
SO 2,3-1,2	(3.7,-1.2)	1.23(0.08)	0.69(0.05)	0.52(0.05)	2.33(0.22)
	(0.6,2.9)	0.24(0.08)	0.09(0.05)	0.37(0.25)	2.34(0.16)
	(0.7,0.7)	0.44(0.08)	0.23(0.05)	0.49(0.15)	2.37(0.21)
	(-0.8,0.4)	0.25(0.08)	0.08(0.06)	0.31(0.24)	2.59(0.13)
	(-1.4,-0.8)	0.63(0.05)	0.33(0.03)	0.49(0.06)	2.33(0.21)
	(-2.8,0.8)	0.22(0.07)	0.14(0.04)	0.61(0.27)	2.64(0.26)
SO 2 3 ₁₃ ⁻² 0 ₂	(-2.3,2.0)	0.21(0.07)	0.06(0.05)	0.29(0.23)	2.29(0.12)
	(3.7,-1.2)	0.17(0.07)	0.12(0.04)	0.67(0.36)	2.21(0.28)
	(0.6,2.9)	... (0.08)
	(0.7,0.7)	0.41(0.07)	0.17(0.04)	0.39(0.12)	2.34(0.16)
	(-0.8,0.4)	0.32(0.11)	0.34(0.07)	1.00(0.39)	2.37(0.43)
	(-1.4,-0.8)	0.74(0.07)	0.32(0.05)	0.41(0.07)	2.27(0.18)
OCS J=7-6	(-2.8,0.8)	... (0.08)
	(-2.3,2.0)	... (0.33)
	(3.7,-1.2)	... (0.07)
	(-1.4,-0.8)	0.16(0.03)	0.15(0.02)	0.88(0.23)	2.38(0.37)

TABLE 4.1b
 $H^{13}CN$ $J=1-0$ HYPERFINE LINES

transition	position	T_R^* (K)	$\int T_R^* dv$ (K km s $^{-1}$)	FWHM (km s $^{-1}$)	V_{LSR} (km s $^{-1}$)
F=2-1	(0.6, 2.9)	0.245(0.034)	0.092(0.011)	0.35(0.06)	2.44(0.15)
F=1-1		0.111(0.034)	0.081(0.016)	0.69(0.25)	7.08(0.29)
F=0-1		0.086(0.034)	0.026(0.010)	0.28(0.15)	-4.78(0.12)
total			0.199(0.089)		
F=2-1	(0.7, 0.7)	0.159(0.042)	0.166(0.023)	0.99(0.29)	2.43(0.42)
F=1-1		0.147(0.042)	0.147(0.022)	0.94(0.30)	7.51(0.40)
F=0-1		0.110(0.042)	0.036(0.013)	0.31(0.16)	-4.78(0.13)
total			0.349(0.145)		
F=2-1	(-0.8, 0.4)	0.046(0.070)	0.013(0.020)	0.26(0.56)	2.43(0.42)
F=1-1		0.116(0.070)	0.071(0.029)	0.57(0.41)	7.66(0.24)
F=0-1		0.085(0.070)	0.059(0.031)	0.65(0.64)	-5.32(0.28)
total			0.143(0.240)		

TABLE 4.1c

 N_2H^+ J=1-0 HYPERFINE LINES

transition	position	T_R^* (K)	$\int T_R^* dv$ (K km s ⁻¹)	FWHP (km s ⁻¹)	V_{LSR}^a (km s ⁻¹)
$F_1=1-1, F=0-1$	(0.6, 2.9)	0.21(0.20)	0.10(0.10)	0.44(0.16)	8.00(1.42)
$F=2-2$		0.67(0.20)	0.31(0.15)		6.76(0.31)
$F=1-1$		0.66(0.20)	0.30(0.14)		6.43(0.30)
total			0.71(0.16)		
$F_1=2-1, F=2-1$		1.10(0.20)	0.51(0.20)		1.83(0.17)
$F=3-2$		1.13(0.20)	0.52(0.21)		0.87(0.17)
$F=1-0$		0.52(0.20)	0.21(0.11)		0.18(0.21)
total			1.24(0.16)		
$F_1=0-1, F=1-2$		0.44(0.20)	0.21(0.11)		-7.13(0.48)
total			2.16(0.25)		2.53(0.14)
$F_1=1-1, F=0-1$	(0.7, 0.7)	0.82(0.15)	0.41(0.12)	0.47(0.11)	7.81(0.32)
$F=2-2$		1.04(0.15)	0.52(0.14)		6.92(0.30)
$F=1-1$		0.86(0.15)	0.43(0.13)		6.42(0.27)
total			1.36(0.12)		
$F_1=2-1, F=2-1$		1.00(0.15)	0.50(0.14)		1.80(0.21)
$F=3-2$		1.52(0.15)	0.76(0.19)		0.93(0.14)
$F=1-0$		0.86(0.15)	0.43(0.13)		0.24(0.20)
total			1.69(0.12)		
$F_1=0-1, F=1-2$		1.01(0.15)	0.51(0.09)		-7.12(0.22)
total			3.55(0.19)		2.54(0.07)
$F_1=1-1, F=0-1$	(-0.8, 0.4)	0.18(0.11)	0.09(0.06)	0.48(0.18)	8.00(2.11)
$F=2-2$		0.79(0.11)	0.40(0.16)		6.93(0.31)
$F=1-1$		0.47(0.11)	0.24(0.11)		6.37(0.52)
total			0.72(0.09)		
$F_1=2-1, F=2-1$		0.76(0.11)	0.39(0.16)		1.90(0.24)
$F=3-2$		1.01(0.11)	0.51(0.20)		0.92(0.20)
$F=1-0$		0.54(0.11)	0.27(0.12)		0.27(0.31)
total			1.67(0.09)		
$F_1=0-1, F=1-2$		0.55(0.11)	0.27(0.06)		-6.97(0.37)
total			2.16(0.14)		2.60(0.12)
$F_1=1-1$	(-1.4, -0.8)		0.08(0.10)		
2-1			0.22(0.10)		
0-1			0.27(0.07)		
total			0.57(0.15)		
$F_1=1-1$	(-2.8, 0.8)		0.08(0.08)		
2-1			0.18(0.08)		
0-1			0.11(0.06)		
total			0.37(0.13)		

$F_1=1-1$	$(-2.3, 2.0)$	
2-1		0.19(0.08)
0-1		0.14(0.08)
total		0.12(0.06)
		0.45(0.13)
$F_1=1-1$	$(3.7, -1.2)$	
2-1		0.06(0.07)
0-1		0.12(0.07)
total		0.13(0.05)
		0.31(0.10)

notes to Table 4.1c:

a based on a $J=1-0$ rest frequency = 93.17330 GHz

TABLE 4.2a

NRAO OBSERVATIONAL RESULTS

transition	position	T_R^* (K)	$\int T_R^* dv$ (K km s ⁻¹)	FWHM (km s ⁻¹)	V_{LSR} (km s ⁻¹)
C_3H_2 $1_{10}^{-1}0_1$	(0,0)	2.13(0.15)	0.68(0.10)	0.30(0.05)	2.36(0.13)
	(-2,-1)	1.06(0.15)	0.39(0.11)	0.35(0.11)	2.36(0.15)
	(-3,1)	0.72(0.15)	0.16(0.11)	0.20(0.14)	2.32(0.09)
	(4,-1)	0.65(0.14)	0.19(0.10)	0.27(0.15)	2.22(0.12)
	(0,2)	2.44(0.15)	0.80(0.10)	0.31(0.04)	2.44(0.13)
	(1,1)	2.28(0.14)	0.77(0.10)	0.32(0.05)	2.39(0.13)
	(1,3)	3.83(0.15)	1.04(0.10)	0.25(0.03)	2.39(0.11)
HC_3N $J=2-1, F=3-2$	(0,0)	0.22(0.07)	0.08(0.04)	0.35(0.22)	2.44(0.15)
	(-2,-1)	... (0.08)
	(-3,1)	0.18(0.08)	0.07(0.04)	0.37(0.27)	2.55(0.16)
	(4,-1)	... (0.08)
	(0,2)	0.88(0.08)	0.19(0.04)	0.20(0.05)	2.44(0.08)
	(1,1)	0.62(0.18)	0.17(0.09)	0.26(0.16)	2.51(0.11)
	(1,3)	0.91(0.08)	0.19(0.04)	0.20(0.05)	2.41(0.08)
	(0.6, 3.3)*	0.94(0.06)	0.28(0.03)	0.30(0.04)	2.46(0.08)
HC_3N $J=2-1, F=2-1$	(0,0)	0.23(0.07)	0.04(0.04)	0.17(0.16)	3.95(0.07)
	(-2,-1)	... (0.08)
	(-3,1)	... (0.08)
	(4,-1)	... (0.08)
	(0,2)*	0.33(0.08)	0.06(0.04)	0.19(0.13)	3.95(0.10)
	(1,1)	... (0.18)
	(1,3)	0.46(0.08)	0.13(0.04)	0.25(0.09)	3.96(0.11)
	(0.6, 3.3)	0.61(0.06)	0.17(0.03)	0.26(0.05)	3.98(0.11)
NH_3 $(2,2)_{main}$	(0,0)	0.51(0.09)	0.13(0.06)	0.23(0.12)	2.42(0.10)
	(-2,-1)	... (0.10)
	(-3,1)	... (0.10)
	(4,-1)	... (0.11)
	(0,2)	0.34(0.10)	0.10(0.06)	0.29(0.19)	2.46(0.12)
	(1,1)	... (0.09)
	(1,3)	0.27(0.09)	0.10(0.06)	0.36(0.25)	2.40(0.15)
C_4H $N=2-1$	(0,0)	... (0.06)
	(-2,-1)	0.15(0.06)	0.07(0.04)	0.41(0.29)	2.41(0.18)
$J, F=3/2, 2-1/2, 1$	(-3,1)*	0.18(0.07)	0.11(0.04)	0.58(0.31)	2.33(0.68)
	(4,-1)	... (0.06)
	(0,2)	... (0.06)
	(1,1)	... (0.07)
	(1,3)	0.20(0.06)	0.04(0.04)	0.21(0.21)	2.50(0.20)

C_4H N=2-1	(0,0)	...	(0.06)
	(-2,-1)	...	(0.06)
J, F=5/2, 3-3/2, 2	(-3,1)	...	(0.06)
	(4,-1)	...	(0.07)
	(0,2)*	0.26	(0.07)	0.12	(0.05)	0.48	(0.24)
	(1,1)	...	(0.07)	2.43
	(1,3)*	0.29	(0.06)	0.12	(0.04)	0.43	(0.17)
							2.59
							(0.29)
C_4H N=2-1	(0,0)	...	(0.06)
	(-2,-1)	...	(0.06)
J, F=5/2, 2-3/2, 1	(-3,1)	...	(0.06)
	(4,-1)	...	(0.07)
	(0,2)	0.21	(0.07)	0.06	(0.05)	0.27	(0.23)
	(1,1)	...	(0.07)	9.25
	(1,3)	0.18	(0.06)	0.08	(0.04)	0.41	(0.27)
							9.08
							(0.17)

* line parameters determined from line moments because Gaussian fit would not converge

TABLE 4.2b

NH₃ (1,1) HYPERFINE LINES

position / transition	T _R [*] (K)	V _{LSR} (km s ⁻¹)	∫ T _R [*] dv (K km s ⁻¹)	FWHM (km s ⁻¹)
(0,0) total		2.42(0.03)	5.87(0.13)	0.38(0.05)
F ₁ =1-0, F=3/2-1/2	1.40(0.10)	-17.13(0.28)	0.79(0.06)	
F=1/2-1/2	0.55(0.10)	-16.96(0.70)		
F ₁ =1-2, F=3/2-5/2	1.63(0.10)	-5.38(0.11)	1.07(0.06)	
F=1/2-3/2	1.11(0.10)	-4.84(0.14)		
F ₁ =2-2, F=5/2-5/2	2.83(0.10)	2.26(0.36)	2.10(0.06)	
F=3/2-3/2	2.07(0.10)	2.66(0.08)		
F ₁ =2-1, F=5/2-3/2	1.60(0.10)	9.90(0.16)	1.04(0.06)	
F=3/2-1/2	0.85(0.10)	10.30(0.30)		
F ₁ =0-1, F=1/2-3/2	1.46(0.10)	21.71(0.33)	0.87(0.05)	
F=1/2-1/2	0.87(0.10)	22.24(0.59)		
(-2,-1) total		2.41(0.04)	2.10(0.12)	0.43(0.16)
F ₁ =1-0, F=3/2-1/2	0.41(0.10)	-17.16(0.97)	0.28(0.06)	
F=1/2-1/2	0.14(0.10)	-17.05(3.23)		
F ₁ =1-2, F=3/2-5/2	0.38(0.10)	-5.39(0.44)	0.23(0.06)	
F=1/2-3/2	0.24(0.10)	-4.86(0.65)		
F ₁ =2-2, F=5/2-5/2	1.04(0.10)	2.24(0.17)	0.98(0.06)	
F=3/2-3/2	0.79(0.10)	2.68(0.27)		
F ₁ =2-1, F=5/2-3/2	0.45(0.10)	9.91(0.60)	0.38(0.06)	
F=3/2-1/2	0.29(0.10)	10.31(0.94)		
F ₁ =0-1, F=1/2-3/2	0.29(0.10)	21.87(1.56)	0.23(0.05)	
F=1/2-1/2	0.26(0.10)	22.21(1.88)		
(-3,1) total		2.44(0.09)	1.68(0.13)	0.47(0.23)
F ₁ =1-0, F=3/2-1/2	0.29(0.10)	-17.17(1.53)	0.24(0.06)	
F=1/2-1/2		
F ₁ =1-2, F=3/2-5/2	0.34(0.10)	-5.39(0.54)	0.27(0.06)	
F=1/2-3/2	0.16(0.10)	-4.80(1.66)		
F ₁ =2-2, F=5/2-5/2	0.75(0.10)	2.33(0.26)	0.68(0.06)	
F=3/2-3/2	0.50(0.10)	2.79(0.40)		
F ₁ =2-1, F=5/2-3/2	0.31(0.10)	9.86(0.80)	0.26(0.06)	
F=3/2-1/2	0.16(0.10)	10.42(1.59)		
F ₁ =0-1, F=1/2-3/2	0.39(0.10)	21.62(1.33)	0.24(0.05)	
F=1/2-1/2	0.21(0.10)	22.27(2.22)		

(4,-1) total		2.43(0.07)	0.59(0.13)	0.42(0.46)
$F_1=1-0, F=3/2-1/2$	0.10(0.10)	-17.13(4.25)	0.03(0.06)	
$F=1/2-1/2$	0.07(0.10)	-17.05(6.14)		
$F_1=1-2, F=3/2-5/2$	0.04(0.06)	
$F=1/2-3/2$	0.11(0.10)	-4.87(1.39)		
$F_1=2-2, F=5/2-5/2$	0.36(0.10)	2.37(0.51)	0.39(0.06)	
$F=3/2-3/2$	0.27(0.10)	2.65(0.76)		
$F_1=2-1, F=5/2-3/2$	0.16(0.10)	9.75(1.23)	0.02(0.06)	
$F=3/2-1/2$		
$F_1=0-1, F=1/2-3/2$	0.17(0.10)	21.76(2.63)	0.11(0.05)	
$F=1/2-1/2$		
(0,2) total		2.45(0.03)	4.48(0.12)	0.39(0.06)
$F_1=1-0, F=3/2-1/2$	0.89(0.09)	-17.13(0.43)	0.48(0.05)	
$F=1/2-1/2$	0.46(0.09)	-16.95(0.80)		
$F_1=1-2, F=3/2-5/2$	1.13(0.09)	-5.36(0.16)	0.80(0.05)	
$F=1/2-3/2$	0.95(0.09)	-4.81(0.17)		
$F_1=2-2, F=5/2-5/2$	2.31(0.09)	2.33(0.08)	1.82(0.05)	
$F=3/2-3/2$	1.64(0.09)	2.71(0.10)		
$F_1=2-1, F=5/2-3/2$	1.29(0.09)	9.91(0.19)	0.75(0.05)	
$F=3/2-1/2$	0.61(0.09)	10.29(0.40)		
$F_1=0-1, F=1/2-3/2$	1.07(0.09)	21.73(0.45)	0.63(0.05)	
$F=1/2-1/2$	0.66(0.09)	22.28(0.75)		
(1,1) total		2.43(0.05)	2.81(0.11)	0.39(0.11)
$F_1=1-0, F=3/2-1/2$	0.65(0.09)	-17.10(0.59)	0.36(0.05)	
$F=1/2-1/2$	0.26(0.09)	-16.91(1.54)		
$F_1=1-2, F=3/2-5/2$	0.61(0.09)	-5.37(0.29)	0.50(0.05)	
$F=1/2-3/2$	0.60(0.09)	-4.82(0.26)		
$F_1=2-2, F=5/2-5/2$	1.43(0.09)	2.27(0.13)	1.11(0.05)	
$F=3/2-3/2$	1.05(0.09)	2.67(0.16)		
$F_1=2-1, F=5/2-3/2$	0.77(0.09)	9.88(0.32)	0.49(0.05)	
$F=3/2-1/2$	0.35(0.09)	10.28(0.71)		
$F_1=0-1, F=1/2-3/2$	0.57(0.09)	21.72(0.86)	0.35(0.04)	
$F=1/2-1/2$	0.30(0.09)	22.37(1.90)		
(1,3) total		2.42(0.04)	4.42(0.12)	0.37(0.07)
$F_1=1-0, F=3/2-1/2$	0.91(0.10)	-17.13(0.43)	0.50(0.06)	
$F=1/2-1/2$	0.41(0.10)	-16.99(0.90)		
$F_1=1-2, F=3/2-5/2$	1.04(0.10)	-5.37(0.17)	0.70(0.06)	
$F=1/2-3/2$	0.79(0.10)	-4.84(0.19)		
$F_1=2-2, F=5/2-5/2$	2.17(0.10)	2.30(0.09)	1.64(0.06)	
$F=3/2-3/2$	1.56(0.10)	2.68(0.10)		
$F_1=2-1, F=5/2-3/2$	0.90(0.10)	9.88(0.20)	0.84(0.06)	
$F=3/2-1/2$	0.56(0.10)	10.30(0.43)		
$F_1=0-1, F=1/2-3/2$	1.09(0.10)	21.66(0.47)	0.75(0.05)	
$F=1/2-1/2$	0.81(0.10)	22.25(0.61)		

TABLE 4.2c

C_3H_2 $J_K^-K^+=1$ 10^{-1} 0_1 DATA AT POSITIONS OF FCRAO SURVEY
AS INTERPOLATED FROM NRAO MAP

position	T_R^* (K)	$\int T_R^* dv$ (K km s ⁻¹)	FWHP (km s ⁻¹)
(0.6, 2.9)	3.27 (0.15)	0.94 (0.11)	0.29 (0.04)
(0.7, 0.7)	2.18 (0.15)	0.73 (0.11)	0.33 (0.05)
(-0.8, 0.4)	1.64 (0.15)	0.55 (0.11)	0.33 (0.07)
(-1.4, -0.8)	1.09 (0.15)	0.48 (0.11)	0.44 (0.12)
(-2.8, 0.8)	<0.91 (0.15)	<0.27 (0.11)	...
(-2.3, 2.0)	<0.91 (0.15)	0.27 (0.11)	>0.3 (0.1)
(3.7, -1.2)	<0.91 (0.15)	<0.27 (0.11)	...

TABLE 4.3

PARAMETERS OF MOLECULES OBSERVED IN L134N

molecule	transition	frequency	B_0	D_0
		(GHz)	(GHz)	(kHz)
C_3H_2	$J_K^-K^+=1_{10}^{-1}0_1$	18.343143	(b)	(b)
C_3H_2	$J_K^-K^+=2_{12}^{-1}0_1$	85.33890	(b)	(b)
C_4H	$N=2-1$	19.054476	4.7586567	0.90
^{12}CO	$J=1-0$	115.271204	57.6359687	183.567
^{13}CO	$J=1-0$	110.201370	55.101021	167.745
$C^{18}O$	$J=1-0$	109.782182	54.891424	166.462
CS	$J=2-1$	97.981007	24.495575	40.24
$C^{34}S$	$J=2-1$	96.412953	24.103551	38.77
$H^{13}CN$	$J=1-0$	86.339944	43.170140	83.8
$H^{13}CO^+$	$J=1-0$	86.754341	(c)	(c)
$HC^{18}O^+$	$J=1-0$	85.162157	(d)	(d)
HC_3N	$J=2-1$	18.196226	4.5490579	0.54311
HC_3N	$J=5-4$	45.490307	4.5490579	0.54311
HC_3N	$J=9-8$	81.881458	4.5490579	0.54311
HCS^+	$J=2-1$	85.34790	21.33715	21.4
$HN^{13}C$	$J=1-0$	87.090851	43.545616	95.5
NH_3	$J, K=1, 1$	23.6944955	(e)	(e)
NH_3	$J, K=2, 2$	23.722633	(e)	(e)
N_2H^+	$J=1-0$	93.17358	(f)	(f)
OCS	$J=7-6$	85.139107	6.08149239	1.30180
SO	$N, J=2, 2-1, 1$	86.09395	21.523561	34.2
SO	$N, J=2, 3-1, 2$	99.299867	21.523561	34.2
^{34}SO	$N, J=2, 3-1, 2$	97.71539	21.102722	32.8
SO_2	$J_K^-K^+=3_{13}^{-2}0_2$	104.029417	(h)	(h)

TABLE 4.3 (cont.)

eqQ	μ	A_{ul}	S	q_v	n^*	T_u
(MHz)	(Db)	(s^{-1})		(a)	(cm^{-3})	(K)
-	3.3	4.15×10^{-7}	1.50	1.58×10^{12}	4.1×10^5	0.9
-	3.3	2.51×10^{-5}	1.50	5.64×10^{11}	2.3×10^6	4.1
-	0.9	2.60×10^{-8}	2.	2.71×10^{13}	1×10^4	1.4
-	0.112	7.45×10^{-8}	1.	3.47×10^{14}	4.2×10^3	5.5
-	0.112	6.51×10^{-8}	1.	3.62×10^{14}	3.8×10^3	5.3
-	0.112	6.44×10^{-8}	1.	3.64×10^{14}	3.7×10^3	5.3
-	1.958	1.68×10^{-5}	2.	1.11×10^{12}	1.5×10^6	7.1
-	1.958	1.60×10^{-5}	2.	1.13×10^{12}	1.5×10^6	6.9
-4.70789	2.9845	2.22×10^{-5}	1.	6.52×10^{11}	5.5×10^6	4.1
-	3.3	2.76×10^{-5}	1.	5.30×10^{11}	5.7×10^5	4.2
-	3.3	2.61×10^{-5}	1.	5.40×10^{11}	5.5×10^5	4.1
-4.3187	3.72	3.88×10^{-7}	2.	1.41×10^{12}	4.7×10^4	1.3
-4.3187	3.72	6.89×10^{-6}	5.	5.84×10^{11}	3.2×10^5	6.5
-4.3187	3.72	4.19×10^{-5}	9.	3.11×10^{11}	1.2×10^6	19.6
-	1.86	1.00×10^{-5}	2.	1.41×10^{12}	1.1×10^5	6.1
0.28	3.05	2.38×10^{-5}	1.	6.18×10^{11}	5.8×10^6	4.2
-4.0924	1.476	1.69×10^{-7}	1.50	1.30×10^{13}	1.9×10^4	23.4
-4.0924	1.476	2.26×10^{-7}	3.333	1.94×10^{13}	2.2×10^4	64.9
(g)	3.4	3.63×10^{-5}	1.	4.65×10^{11}	7.2×10^5	4.5
-	0.71519	1.71×10^{-6}	7.	8.22×10^{12}	6.7×10^4	16.3
-	1.55	5.35×10^{-6}	1.50	2.69×10^{12}	5×10^5	19.3
-	1.55	1.61×10^{-5}	2.933	1.19×10^{12}	1×10^6	9.2
-	1.55	1.53×10^{-5}	2.935	1.21×10^{12}	1×10^6	9.1
-	1.59	9.54×10^{-6}	2.0162	2.21×10^{12}	8×10^5	6.1

notes for Table 4.3:

(a) units are $s K^{-1} km^{-1} cm^{-2}$

(b) C_3H_2 is an asymmetric top with: $A=35.092596$, $B=32.212931$,
 $C=16.749315$ GHz

(c) $2B_0 - 4D_0 = 86.754341$ GHz

(d) $2B_0 - 4D_0 = 85.162157$ GHz

(e) inversion transition; NH_3 is a oblate symmetric top with:
 $B=298.11537$, $C=189$. GHz

(f) $2B_0 - 4D_0 = 93.173392$ GHz

(g) outer N, $eqQ = -5.666$ MHz; Inner N, $eqQ = -1.426$ MHz

(h) SO_2 is an asymmetric top with: $A=60.778516$, $B=10.317963$,
 $C=8.799808$ (GHz)

references for Table 4.3:

C_3H_2 molecular constants from Vrtilek, Gottlieb, and Thaddeus 1987

C_4H molecular constants from Guellin, Friberg, and Mezaoui 1982

line strengths, S, for SO and ^{34}SO from Tiemann 1974

line strength, S, for SO_2 from Lovas 1985

all other molecular constants from Winnewisser, Churchwell, and
 Walmsley 1979

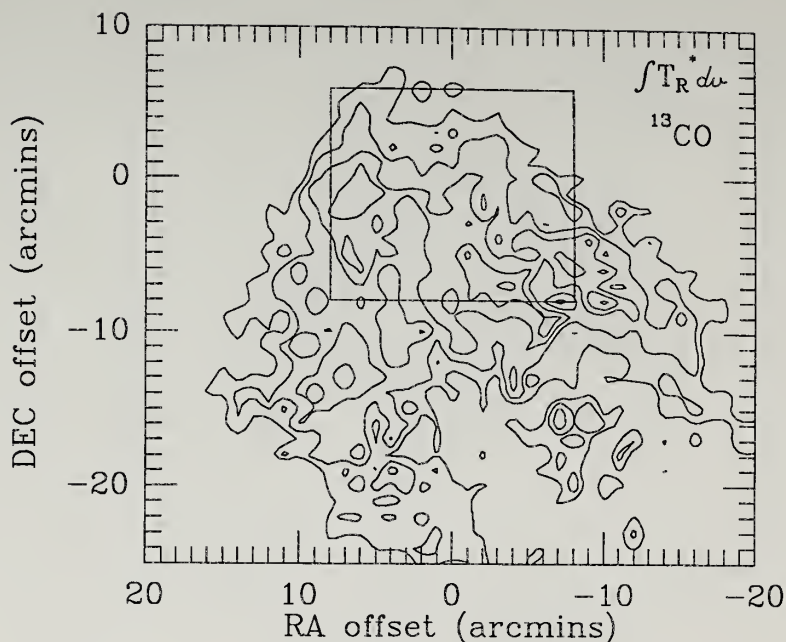


Figure 4.1 Contour map of the Integrated Intensity from ^{13}CO J=1-0 emission line in L134N. This map is a subset of the map of Figure 2.1 with the dense core region indicated by the inset box. As with all maps presented here, the x and y axes are offsets in right ascension and declination, respectively, in units of minutes of arc from a reference position; RA = $15^{\text{h}}51^{\text{m}}30^{\text{s}}$, DEC = $-2^{\circ}43'31''$ (1950.0). In this figure there are five contour levels ranging from 3 to 7 K km s^{-1} in steps of 1 K km s^{-1} . As stated in the text, the dense core is not apparent from the ^{13}CO emission.

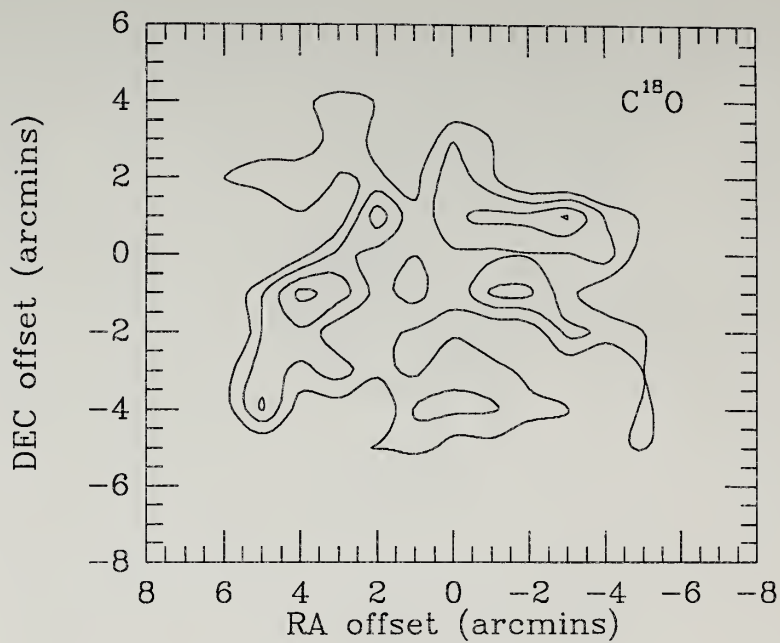


Figure 4.2a Contour map of the $C^{18}O$ J=1-0 Integrated Intensity in L134N. The contour levels in units of $K km s^{-1}$ are 1.1 to 2.0 by 0.3.

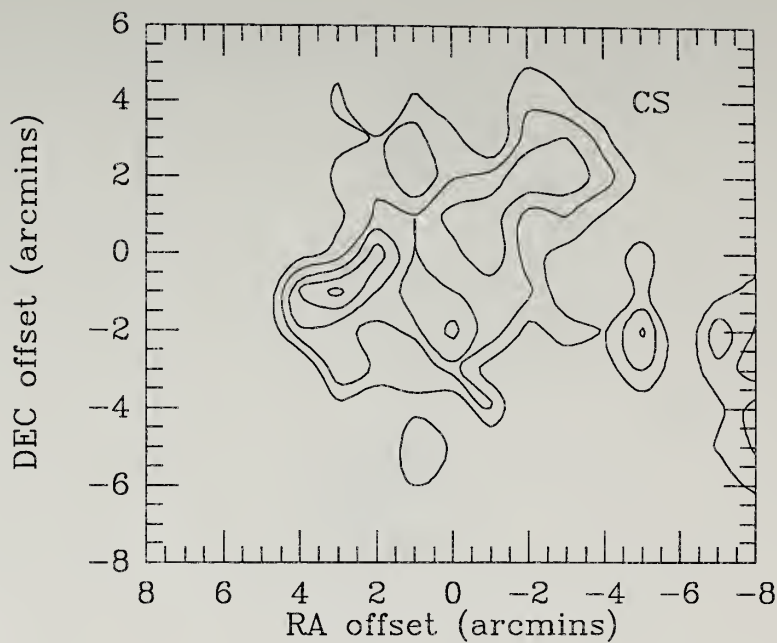


Figure 4.2b Contour map of the CS J=2-1 Integrated Intensity in L134N. The contour levels in units of K km s^{-1} are 0.5 to 1.3 by 0.2.

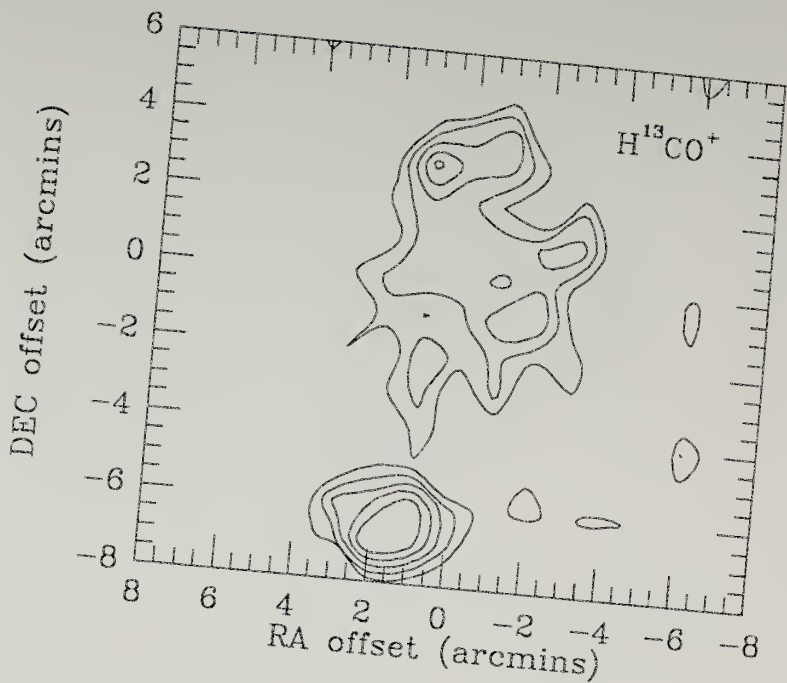


Figure 4.2c Contour map of the H^{13}CO^+ $J=1-0$ Integrated intensity in L134N. The contour levels in units of K km s^{-1} are 0.3 to 0.7 by 0.1.

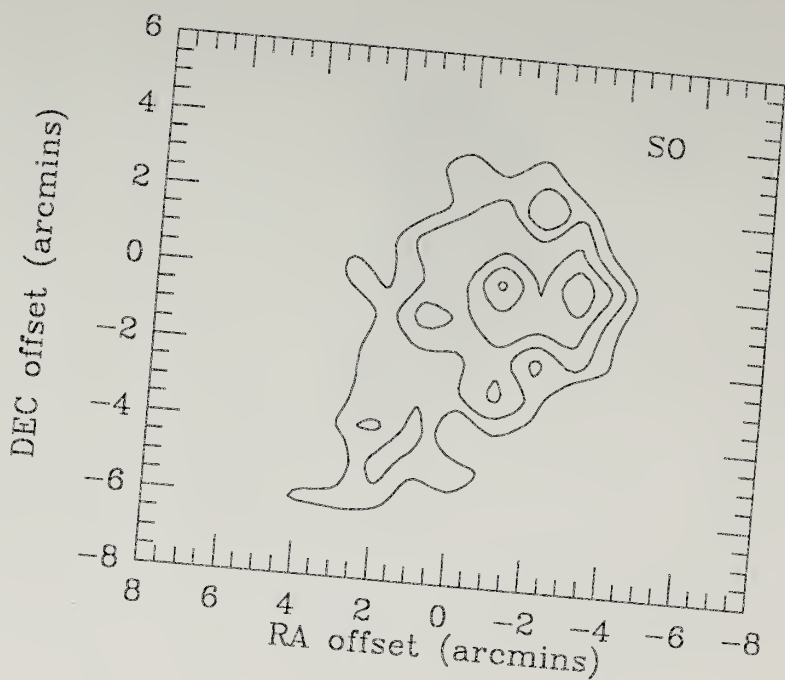


Figure 4.2d Contour map of the SO N, J=2,3-1,2 Integrated intensity in L134N. The and contour levels in units of K km s^{-1} are 0.8 to 2.0 by 0.3.

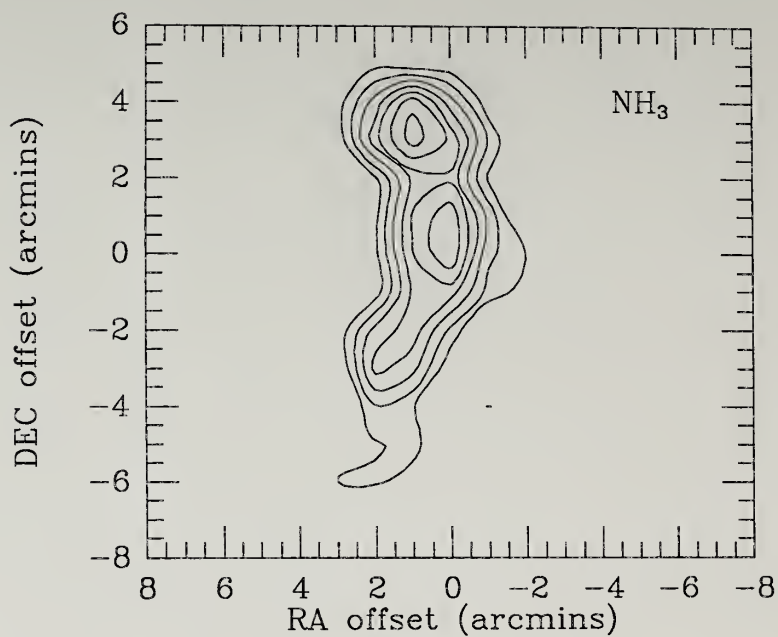


Figure 4.2e Contour map of the NH_3 (1,1) main hyperfine line integrated intensity in L134N. The contour levels in units of K km s^{-1} are 1.0 to 3.4 by 0.4.

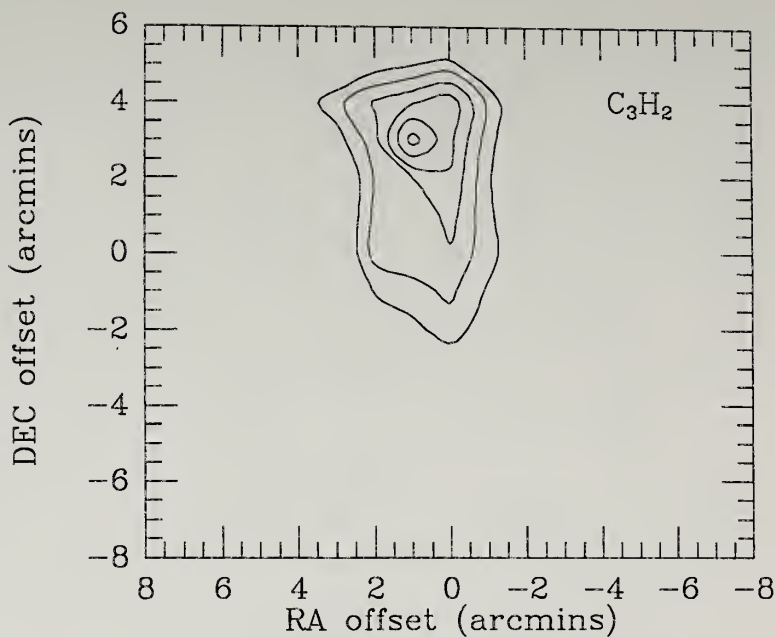


Figure 4.2f Contour map of the C_3H_2 $1_{10}-1_{01}$ integrated intensity in L134N. The contour levels in units of $K km s^{-1}$ are 0.55 to 1.05 by 0.10.

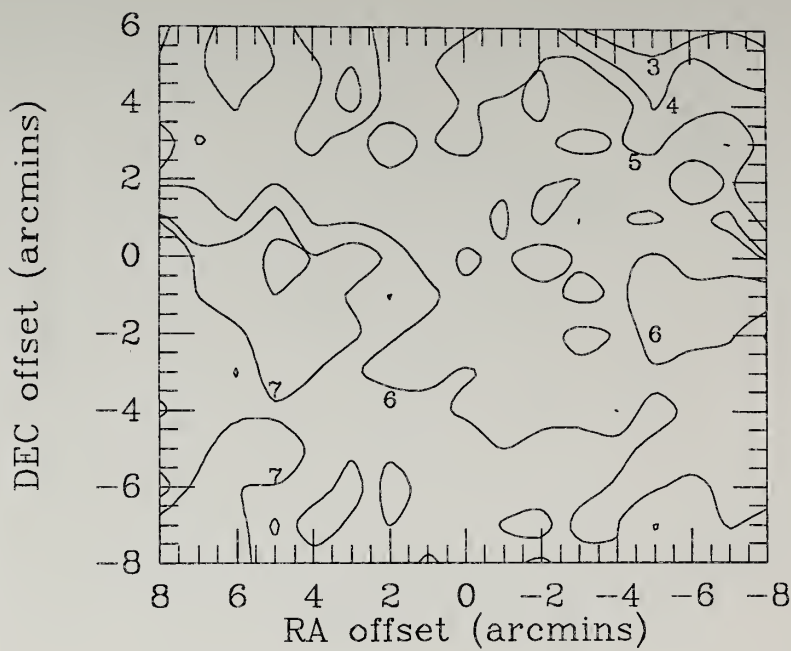


Figure 4.3 Contour map of the peak ^{12}CO J=1-0 emission across the core region. Contour levels are from 3 to 7 K in steps of 1 K.

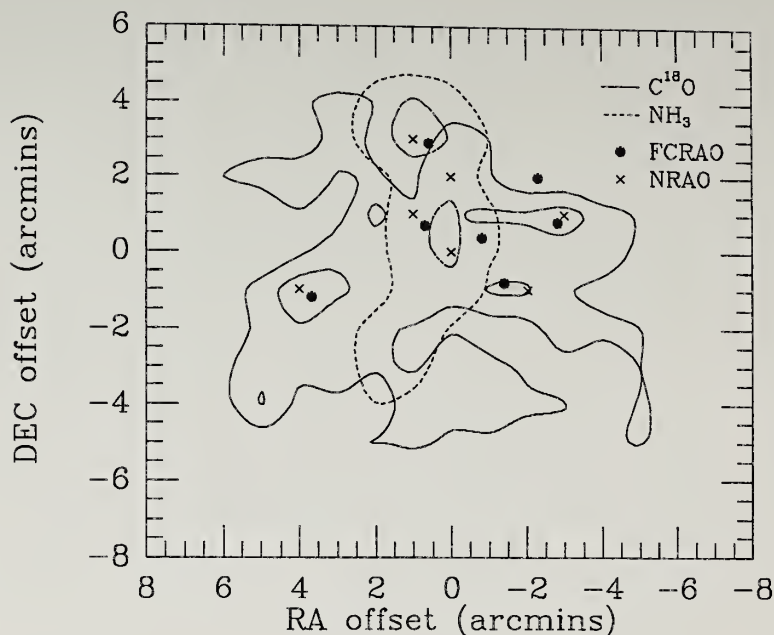


Figure 4.4 Positions observed in the FCRAO and NRAO spectral line surveys superimposed on the 1.1 and 1.7 $K km s^{-1}$ integrated intensity contours of $C^{18}O$ $J=1-0$ and the 1.4 and 3.0 $K km s^{-1}$ integrated intensity contours of NH_3 $(1,1)_M$. Each survey observed seven positions whose exact coordinates are listed in the text. Approximate beam sizes are 1 arcminute for the FCRAO survey transitions and 1.6 arcminutes for the NRAO survey transitions.

Figure 4.5 ^{12}CO J=1-0 spectra in L134N from the FCRAO survey. Each spectra is labeled with a letter corresponding to a survey position : a (0.6,2.9); b (0.7,0.7); c (-0.8,0.4); d (-1.4,-0.8); e (-2.8,0.8); f (-2.3,2.0); g (3.7,-1.2).

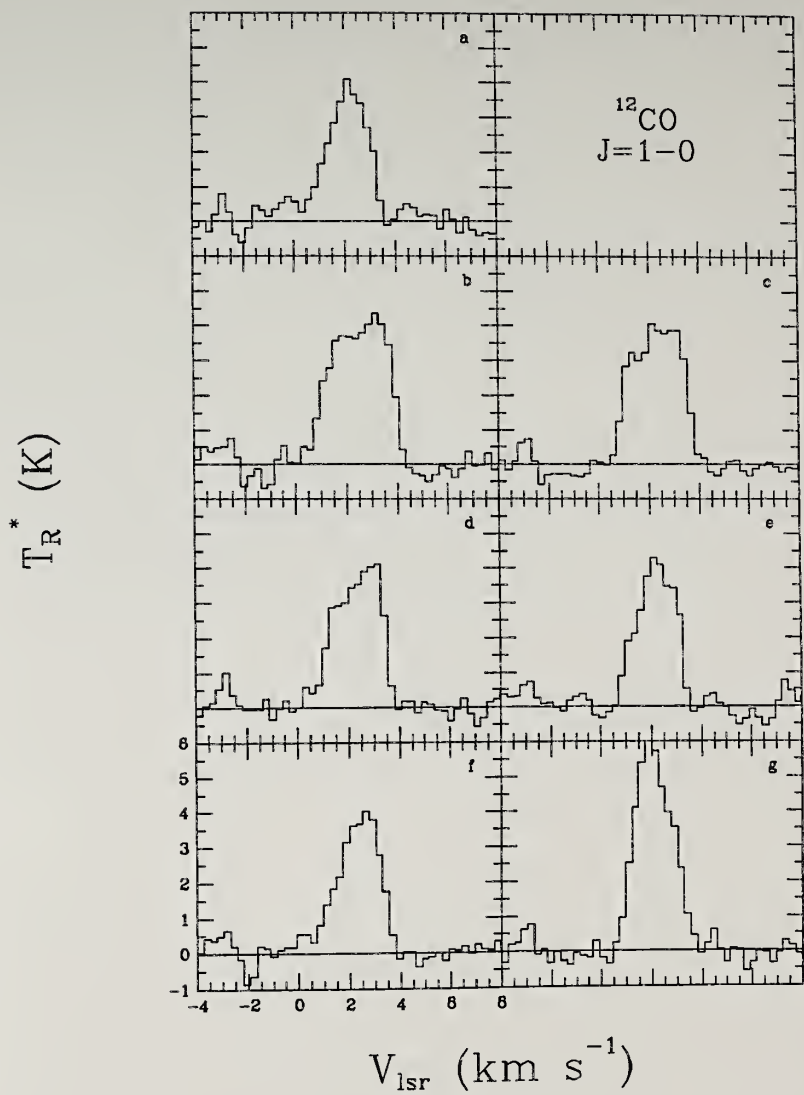


Figure 4.6 $C^{18}O$ J=1-0 spectra in L134N from the FCRAO survey. Each spectra is labeled with a letter corresponding to a survey position : a (0.6,2.9); b (0.7,0.7); c (-0.8,0.4); d (-1.4,-0.8); e (-2.8,0.8); f (-2.3,2.0); g (3.7,-1.2).

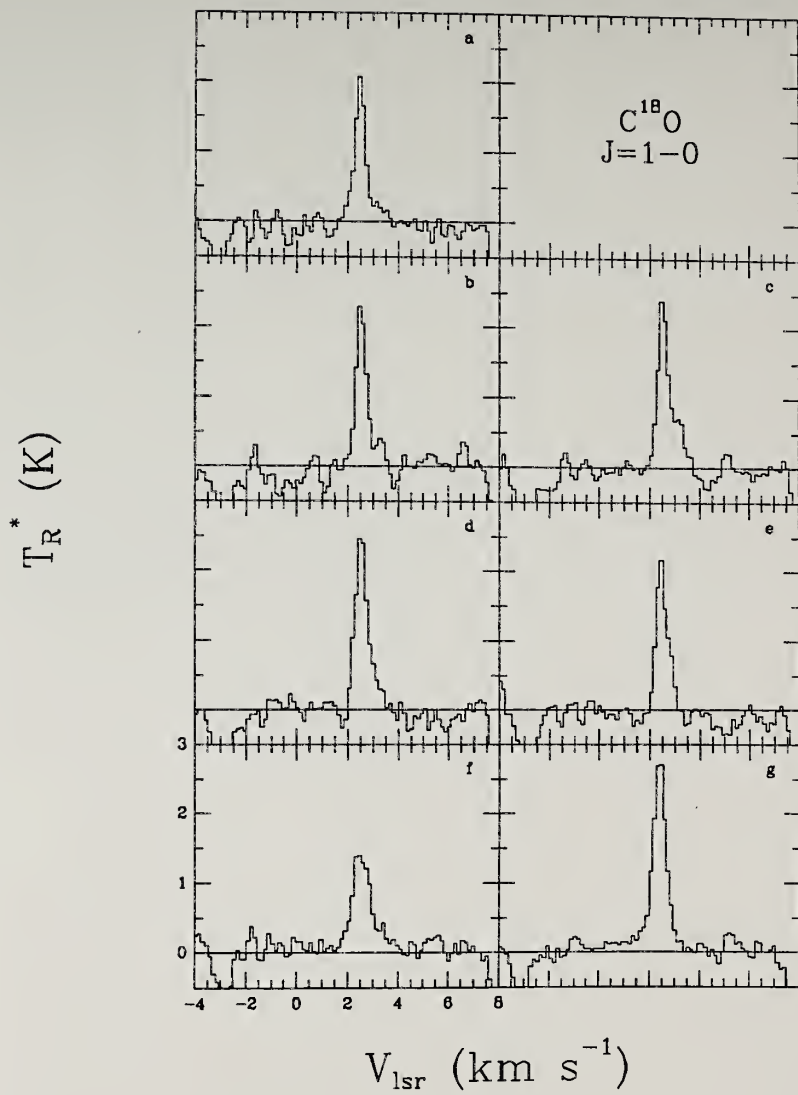


Figure 4.7 CS J=2-1 spectra in L134N from the FCRAO survey. Each spectra is labeled with a letter corresponding to a survey position : a (0.6,2.9); b (0.7,0.7); c (-0.8,0.4); d (-1.4,-0.8); e (-2.8,0.8); f (-2.3,2.0); g (3.7,-1.2).

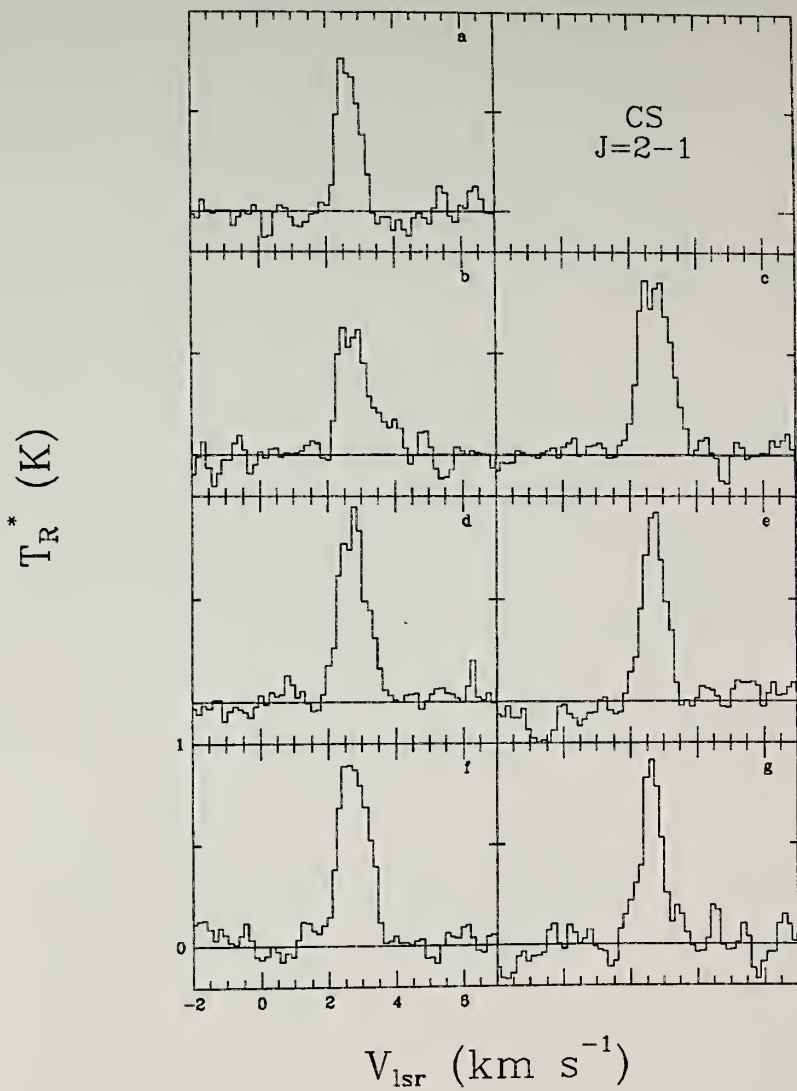


Figure 4.8 C^{34} S J=2-1 spectra in L134N from the FCRAO survey. Each spectra is labeled with a letter corresponding to a survey position : a (0.6,2.9); b (0.7,0.7); c (-0.8,0.4); d (-1.4,-0.8); e (-2.8,0.8); f (-2.3,2.0); g (3.7,-1.2).

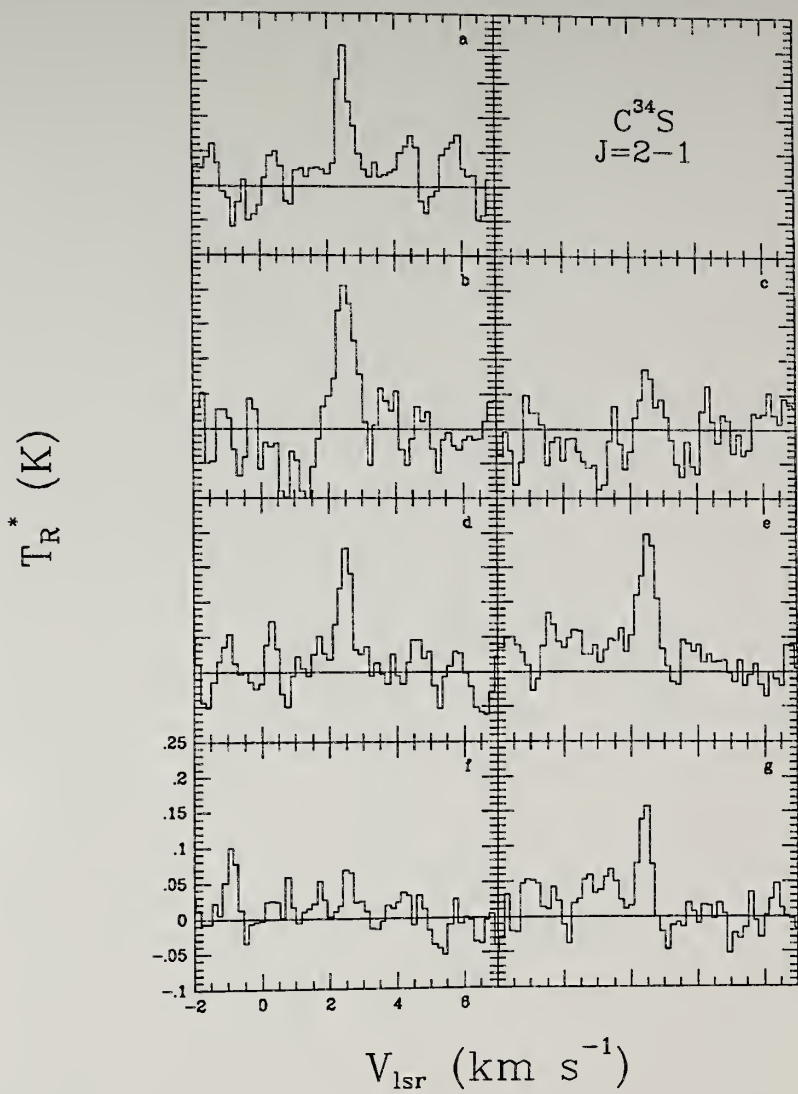


Figure 4.9 HCS^+ $J=2-1$ spectra in L134N from the FCRAO survey. Each spectra is labeled with a letter corresponding to a survey position : a (0.6,2.9); b (0.7,0.7); c (-0.8,0.4); d (-1.4,-0.8); e (-2.8,0.8); f (-2.3,2.0); g (3.7,-1.2).

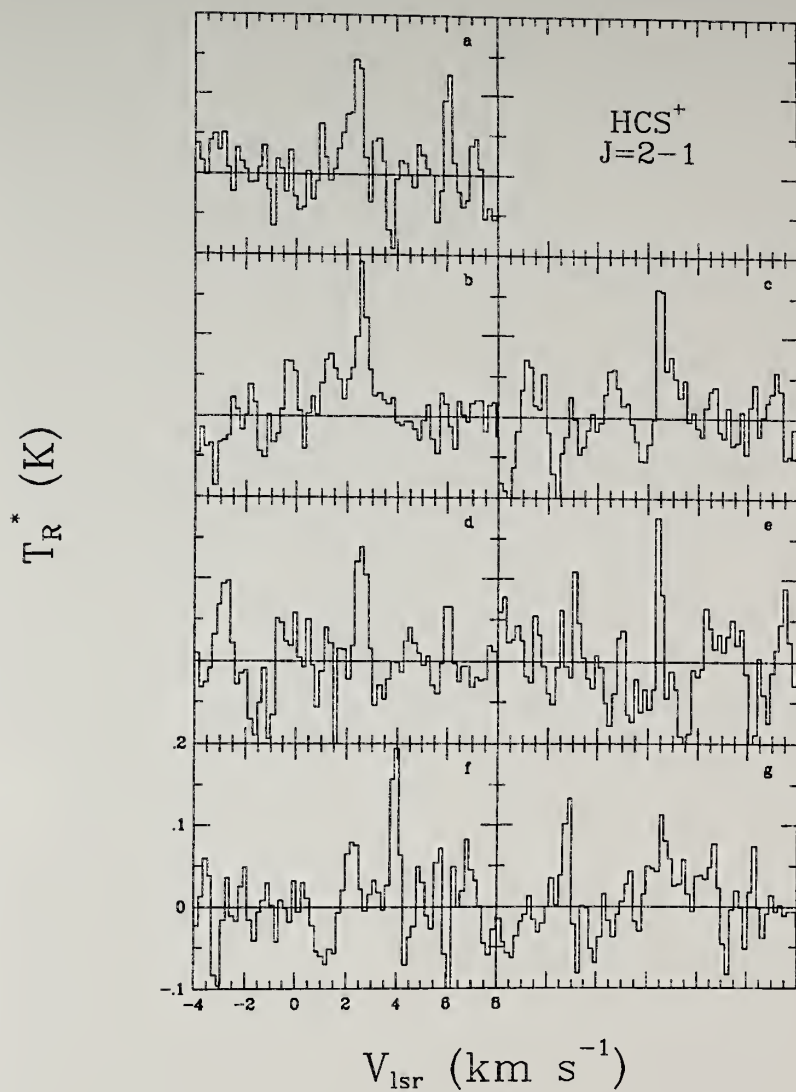
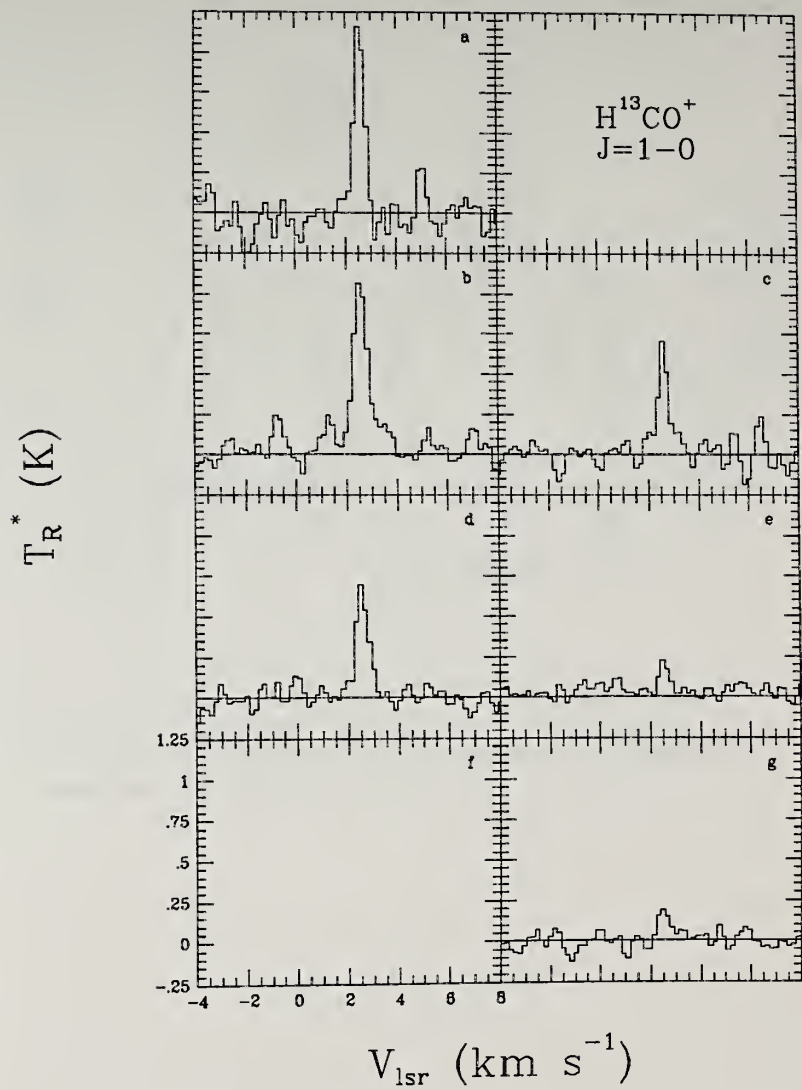


Figure 4.10 H^{13}CO^+ $J=1-0$ spectra in L134N from the FCRAO survey. Each spectra is labeled with a letter corresponding to a survey position : a (0.6,2.9); b (0.7,0.7); c (-0.8,0.4); d (-1.4,-0.8); e (-2.8,0.8); g (3.7,-1.2). The spectra at position f (-2.3,2.0) was not observed.



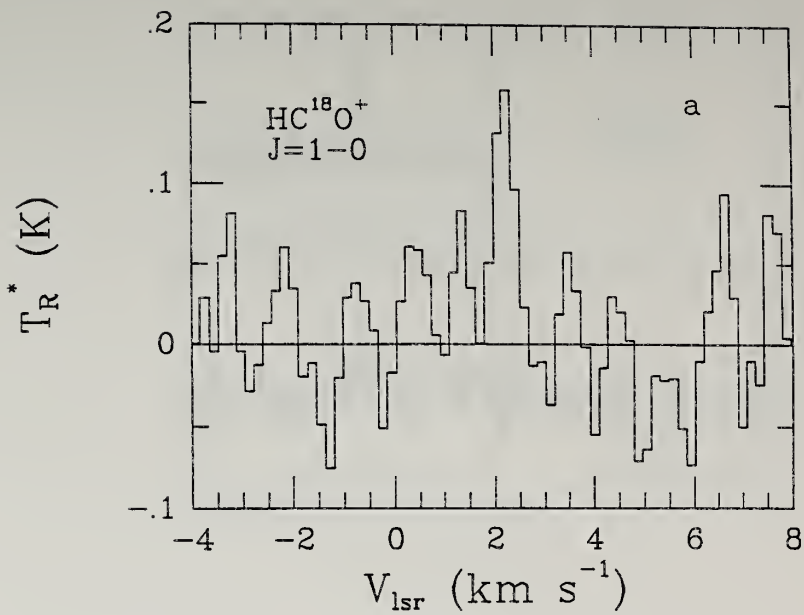


Figure 4.11 HC^{18}O^+ $J=1-0$ spectra in L134N from the FCRAO survey at position a (0.6,2.9).

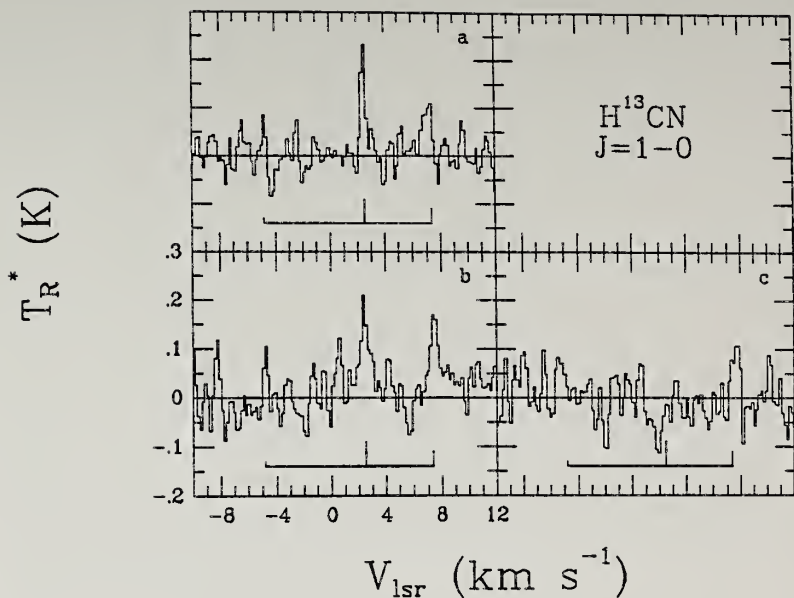


Figure 4.12 Three H^{13}CN $J=1-0$ spectra observed in L134N from the FCRAO survey at positions a (0.6,2.9); b (0.7,0.7); and c (-0.8,0.4). Bar below spectra indicates theoretical positions and LTE relative intensities of the hyperfine components.

Figure 4.13 HN^{13}C J=1-0 spectra in L134N from the FCRAO survey. Each spectra is labeled with a letter corresponding to a survey position : a (0.6,2.9); b (0.7,0.7); c (-0.8,0.4); d (-1.4,-0.8); e (-2.8,0.8); f (-2.3,2.0); g (3.7,-1.2).

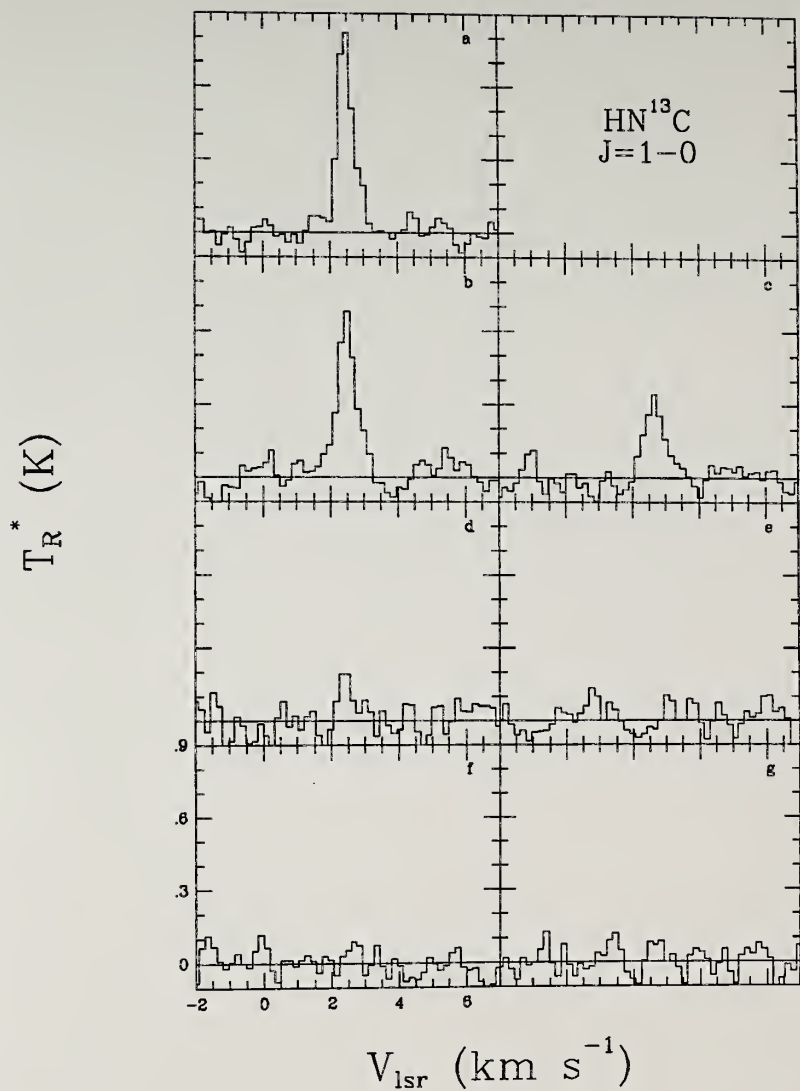
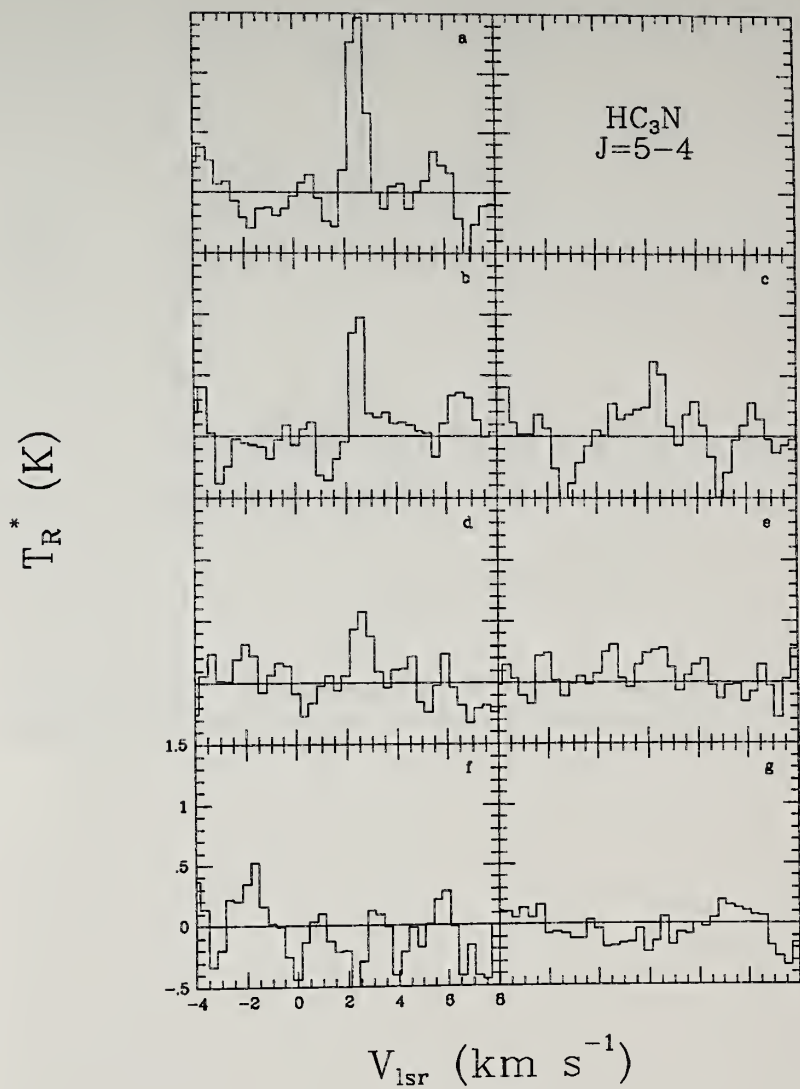


Figure 4.14 HC_3N J=5-4 spectra in L134N from the FCRAO survey. Each spectra is labeled with a letter corresponding to a survey position : a (0.6,2.9); b (0.7,0.7); c (-0.8,0.4); d (-1.4,-0.8); e (-2.8,0.8); f (-2.3,2.0); g (3.7,-1.2).



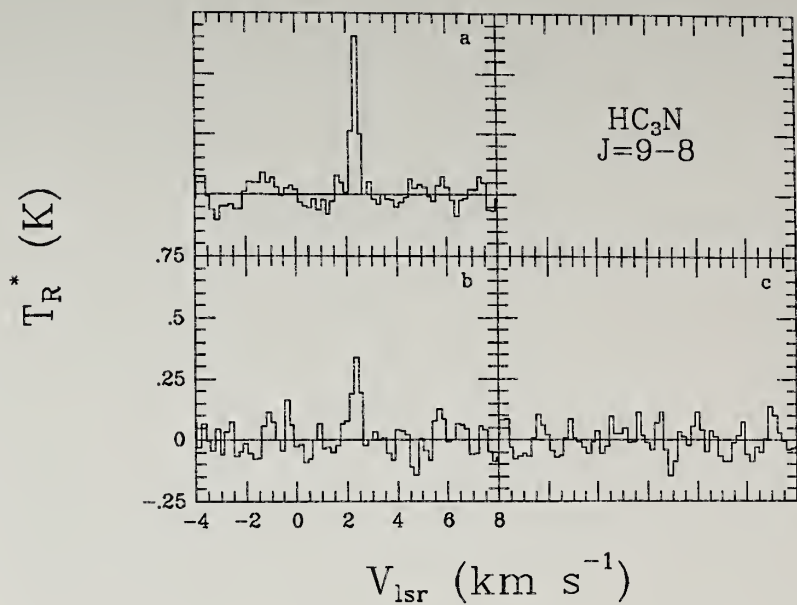


Figure 4.15 Three HC_3N $J=9-8$ spectra in L134N from the FCRAO survey. Positions a (0.6,2.9); b (0.7,0.7); and c (-0.8,0.4).

Figure 4.16 C_3H_2 $2_{12}-1_{01}$ spectra in L134N from the FCRAO survey. Each spectra is labeled with a letter corresponding to a survey position : a (0.6,2.9); b (0.7,0.7); c (-0.8,0.4); d (-1.4,-0.8); e (-2.8,0.8); f (-2.3,2.0); g (3.7,-1.2).

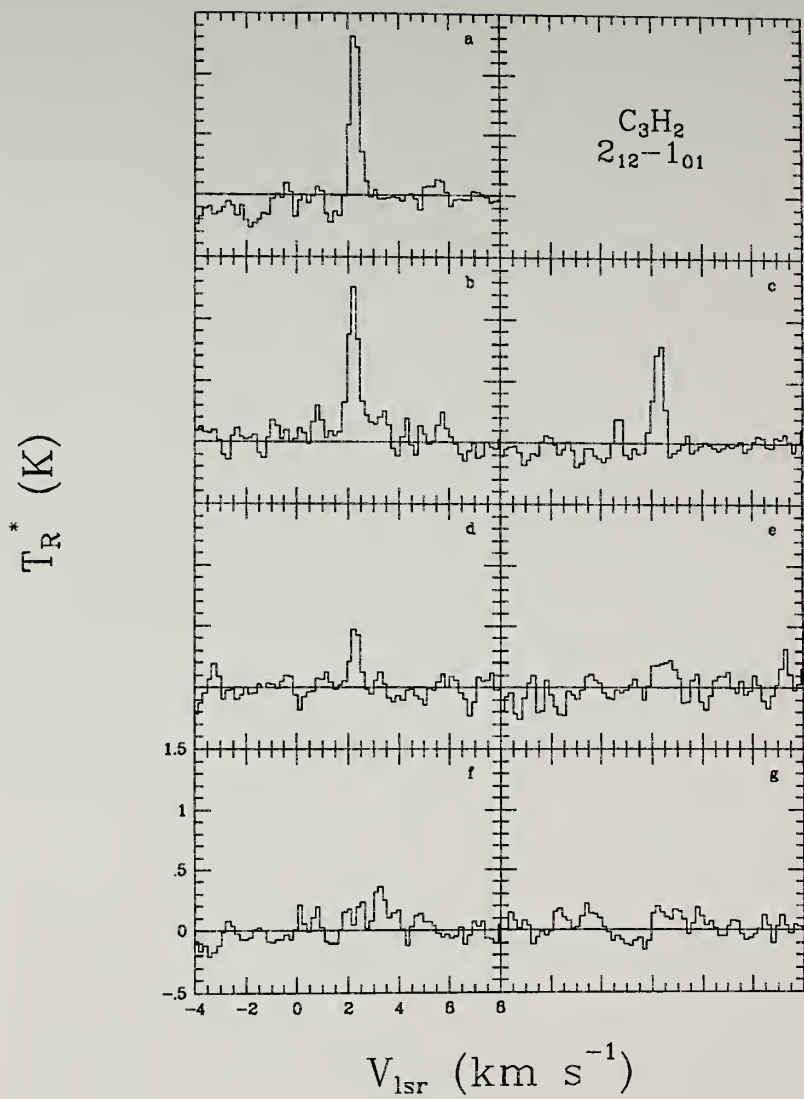


Figure 4.17 N_2H^+ J=1-0 spectra in L134N from the FCRAO survey. Each spectra is labeled with a letter corresponding to a survey position : a (0.6,2.9); b (0.7,0.7); c (-0.8,0.4); d (-1.4,-0.8); e (-2.8,0.8); f (-2.3,2.0); g (3.7,-1.2). Bar below spectra indicates theoretical positions and LTE relative intensities of the hyperfine components.

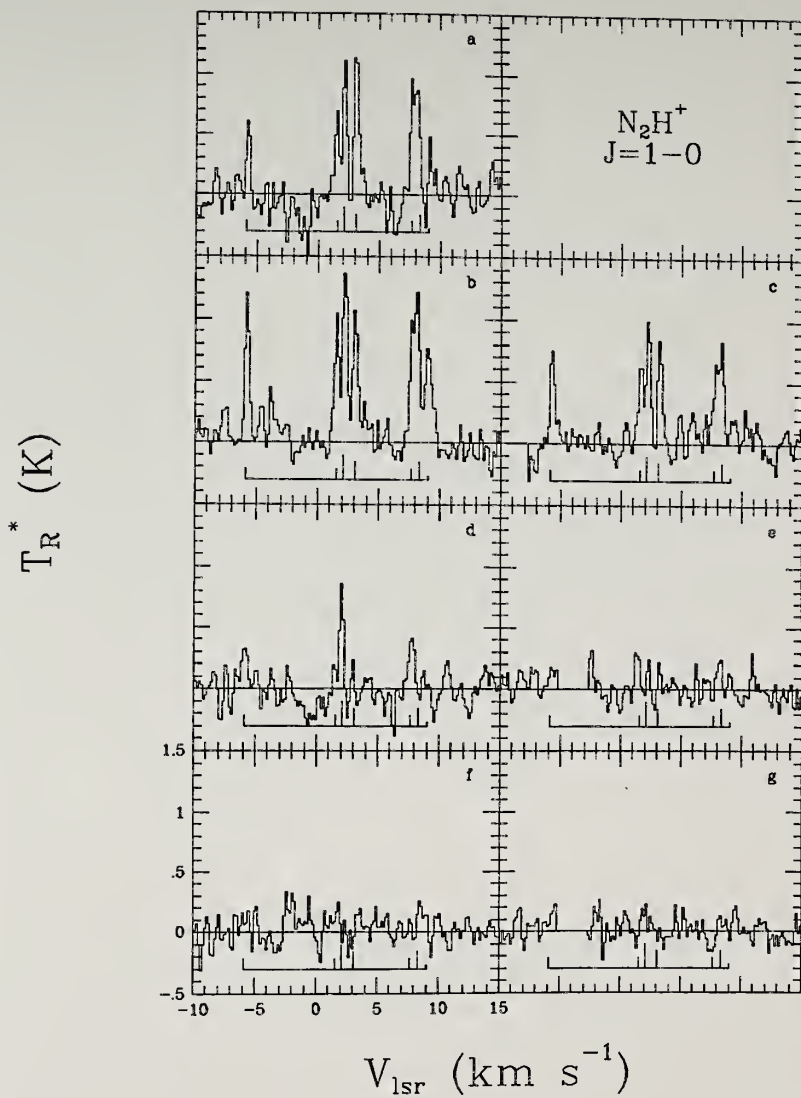


Figure 4.18 SO N,J=2,3-1,2 spectra in L134N from the FCRAO survey. Each spectra is labeled with a letter corresponding to a survey position : a (0.6,2.9); b (0.7,0.7); c (-0.8,0.4); d (-1.4,-0.8); e (-2.8,0.8); f (-2.3,2.0); g (3.7,-1.2).

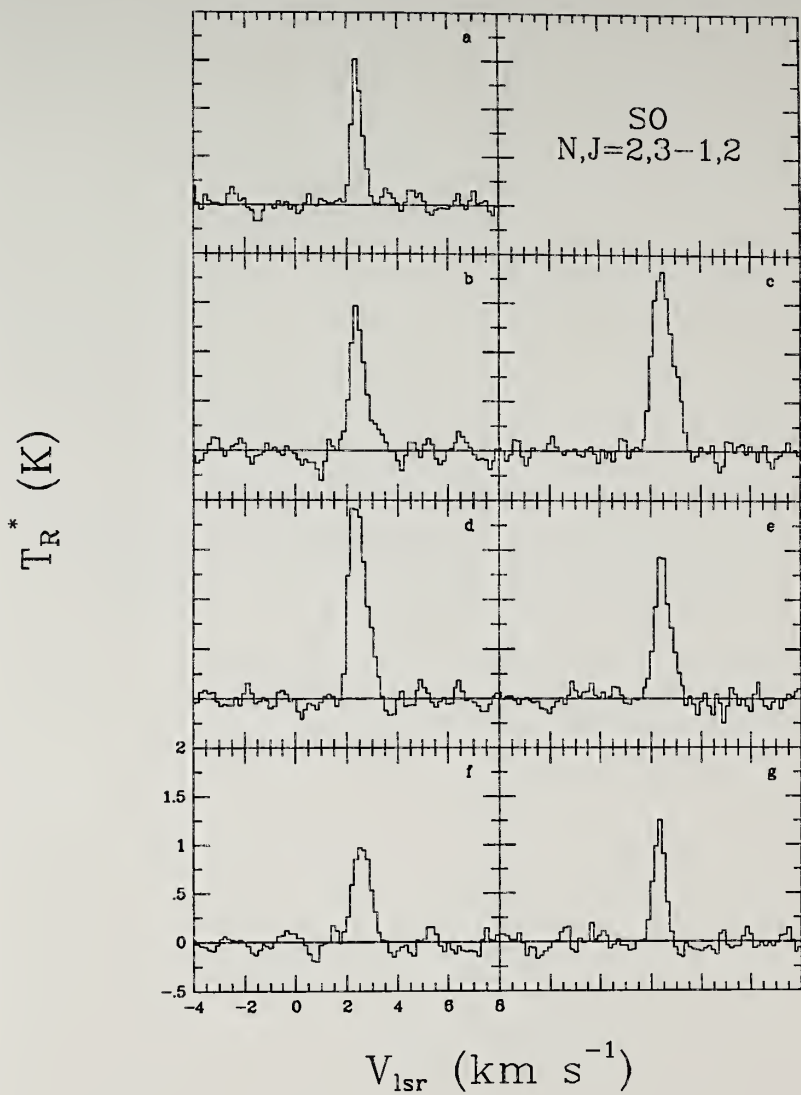


Figure 4.19 S0 N,J=2,2-1,1 spectra in L134N from the FCRAO survey. Each spectra is labeled with a letter corresponding to a survey position : a (0.6,2.9); b (0.7,0.7); c (-0.8,0.4); d (-1.4,-0.8); e (-2.8,0.8); f (-2.3,2.0); g (3.7,-1.2).

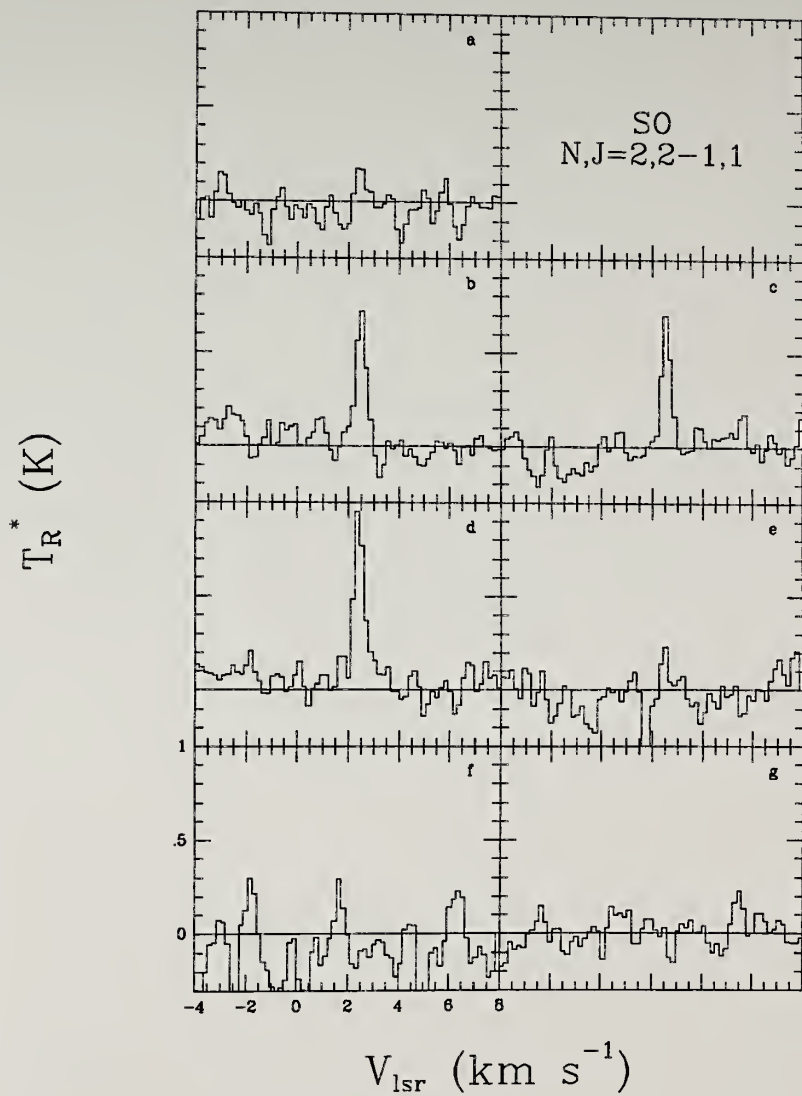


Figure 4.20 $^{34}\text{S O N, J=2,3-1,2}$ spectra in L134N from the FCRAO survey. Each spectra is labeled with a letter corresponding to a survey position : a (0.6,2.9); b (0.7,0.7); c (-0.8,0.4); d (-1.4,-0.8); e (-2.8,0.8); f (-2.3,2.0); g (3.7,-1.2).

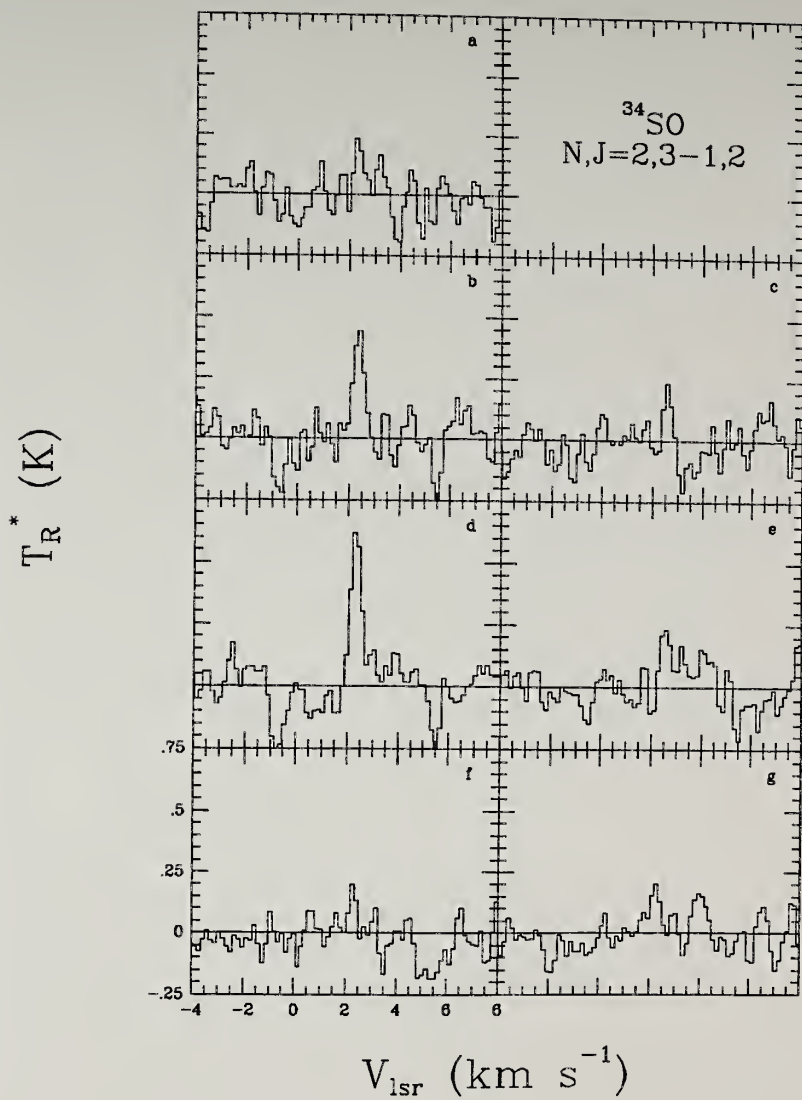
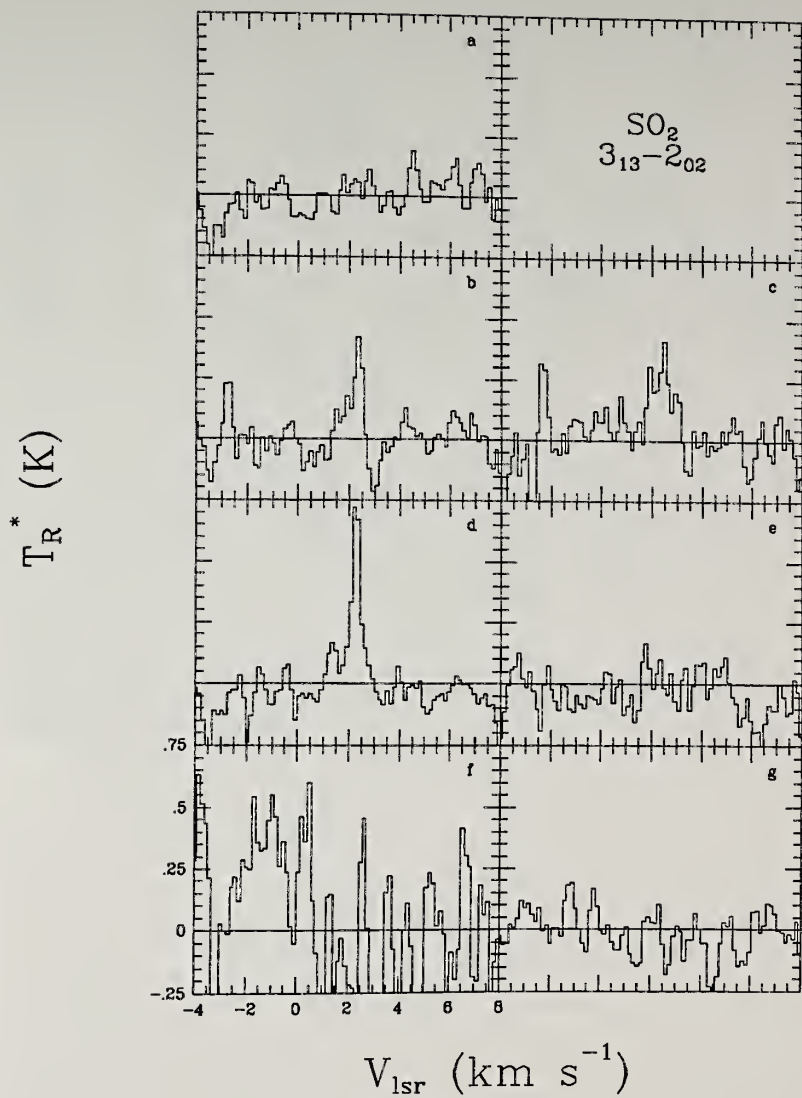


Figure 4.21 SO_2 $3_{13}-2_{02}$ spectra in L134N from the FCRAO survey. Each spectra is labeled with a letter corresponding to a survey position : a (0.6,2.9); b (0.7,0.7); c (-0.8,0.4); d (-1.4,-0.8); e (-2.8,0.8); f (-2.3,2.0); g (3.7,-1.2).



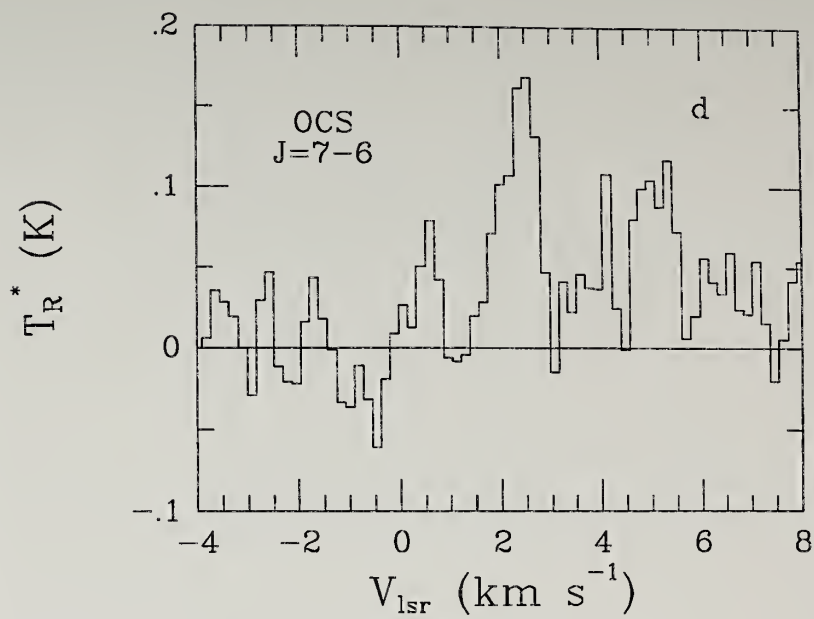


Figure 4.22 OCS J=7-6 spectra in L134N from the FCRAO survey at position d (-1.4,-0.8).

Figure 4.23 NH_3 (1,1) spectra in L134N from the NRAO survey. Each spectra is labeled with a letter corresponding to a survey position : a (1,3); b (1,1); c (0,2); d (0,0); e (-2,-1); f (-3,1); g (4,-1). Bar below spectra indicates theoretical positions and LTE relative intensities of the hyperfine components.

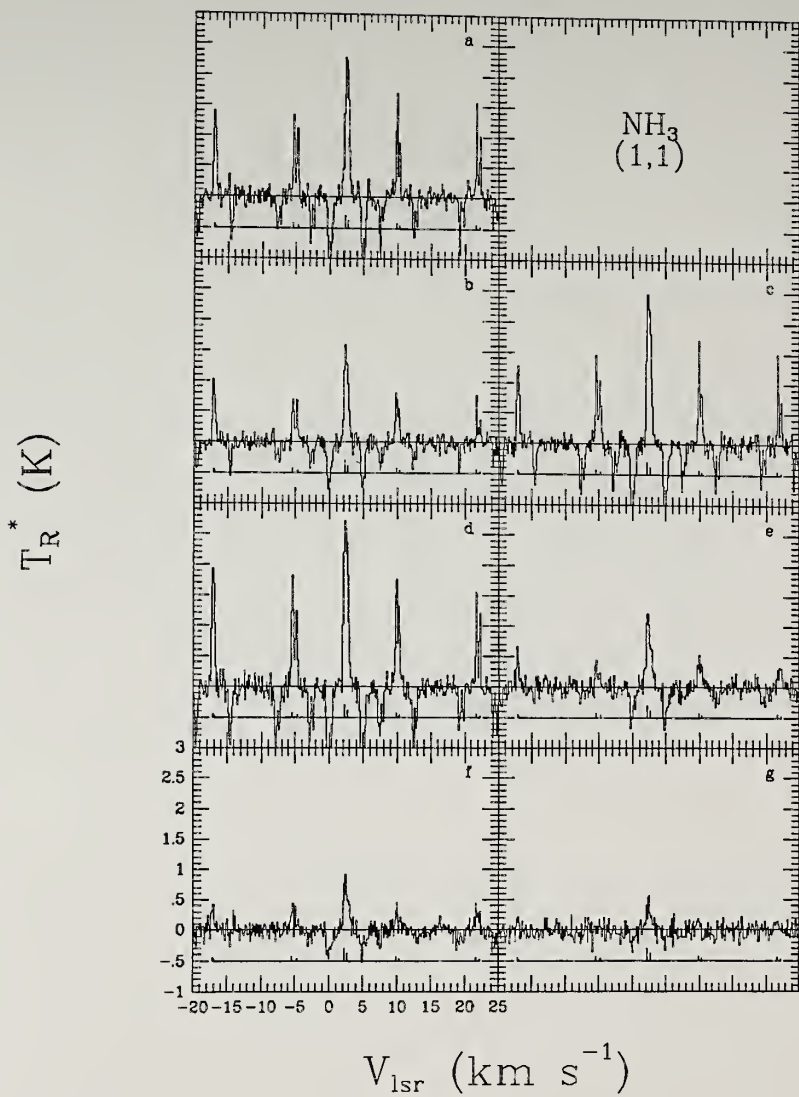


Figure 4.24 NH_3 (2,2) main hyperfine component spectra in L134N from the NRAO survey. Each spectra is labeled with a letter corresponding to a survey position : a (1,3); b (1,1); c (0,2); d (0,0); e (-2,-1); f (-3,1); g (4,-1).

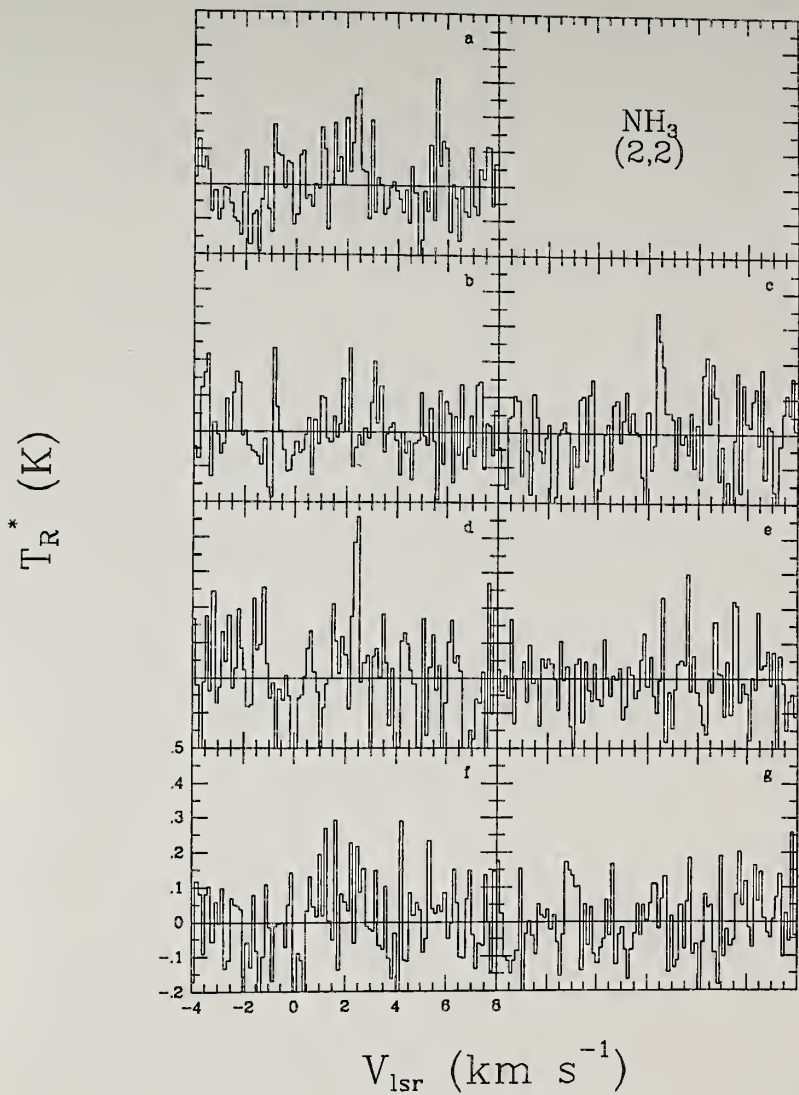


Figure 4.25 C_3H_2 $1_{10}-1_{01}$ spectra in L134N from the NRAO survey. Each spectra is labeled with a letter corresponding to a survey position : a (1,3); b (1,1); c (0,2); d (0,0); e (-2,-1); f (-3,1); g (4,-1).

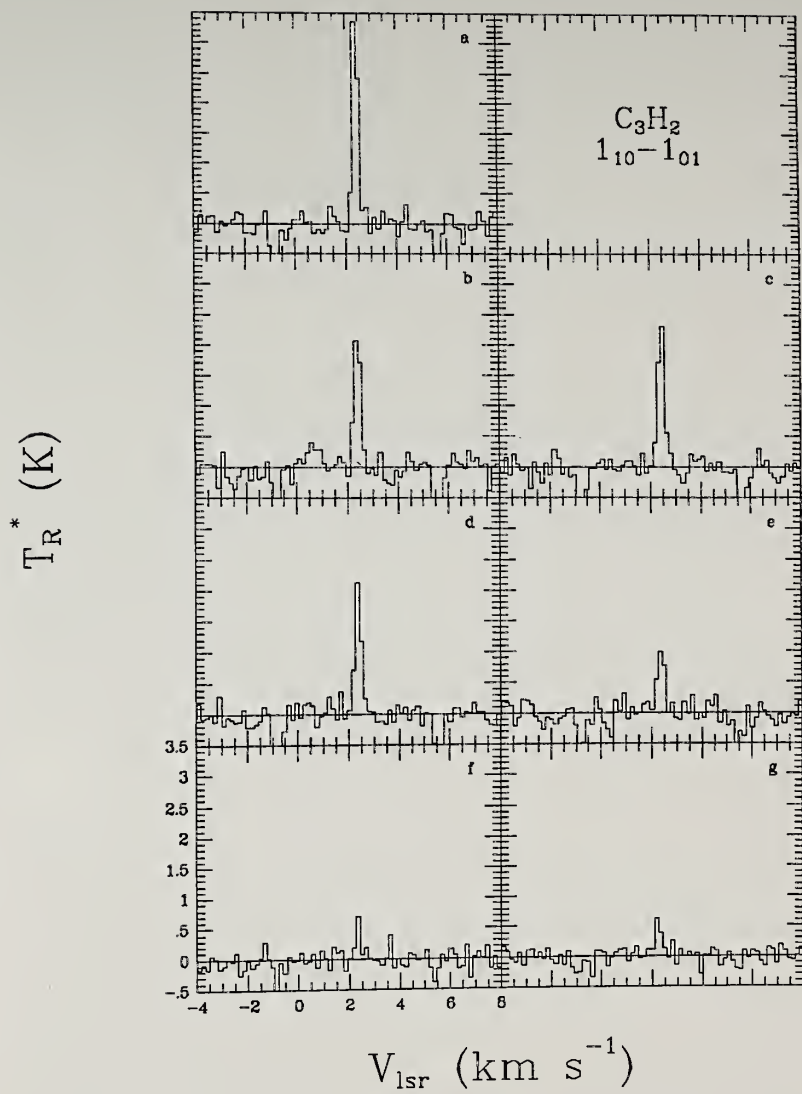


Figure 4.26 HC_3N $J=2-1$ spectra in L134N from the NRAO survey. Each spectra is labeled with a letter corresponding to a survey position : a (1,3); b (1,1); c (0,2); d (0,0); e (-2,-1); f (-3,1); g (4,-1). Bar below spectra indicates theoretical positions and LTE relative intensities for the $F=3-2$ (2.5 km s^{-1}) and $F=2-1$ (4.1 km s^{-1}) hyperfine components.

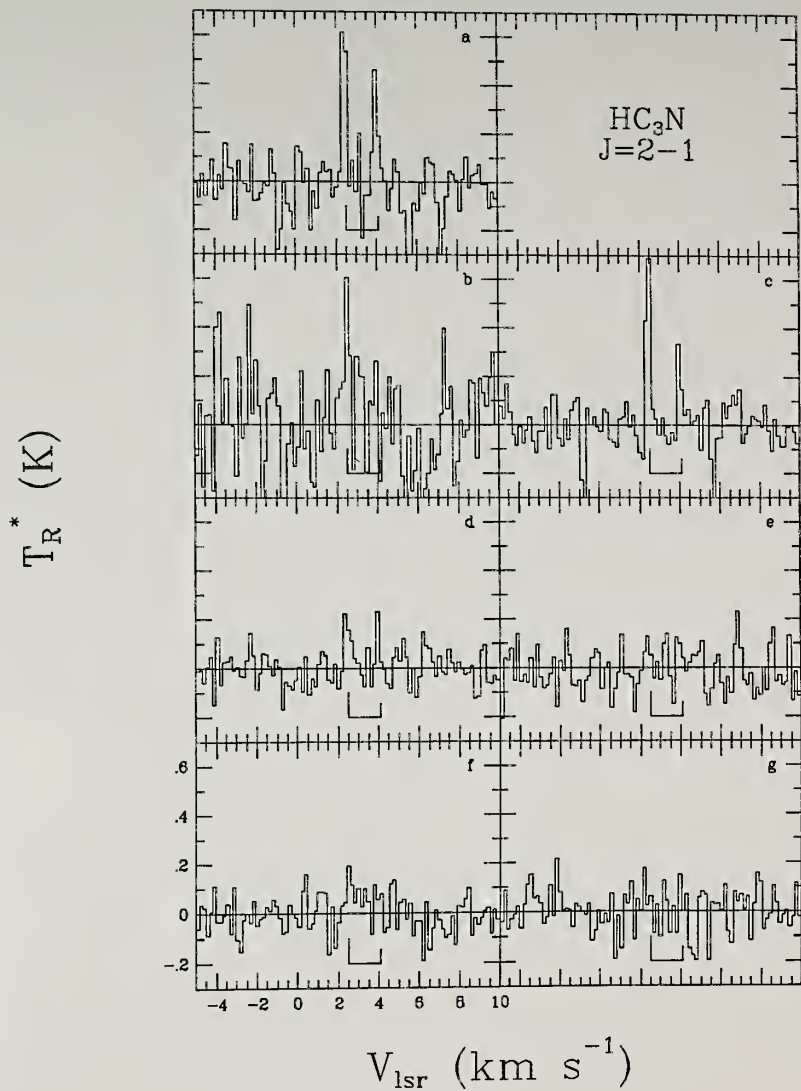


Figure 4.27 C_4H N=2-1, F=3-2 spectra in L134N from the NRAO survey. Each spectra is labeled with a letter corresponding to a survey position : a (1,3); b (1,1); c (0,2); d (0,0); e (-2,-1); f (-3,1); g (4,-1).

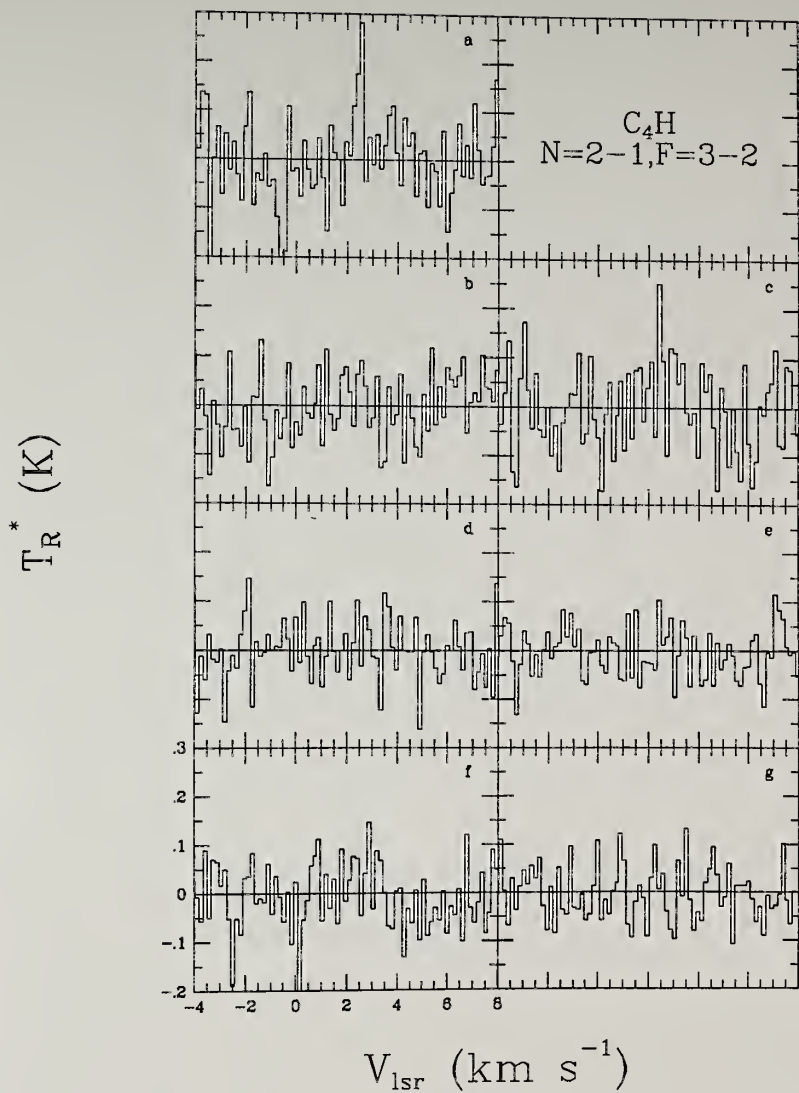
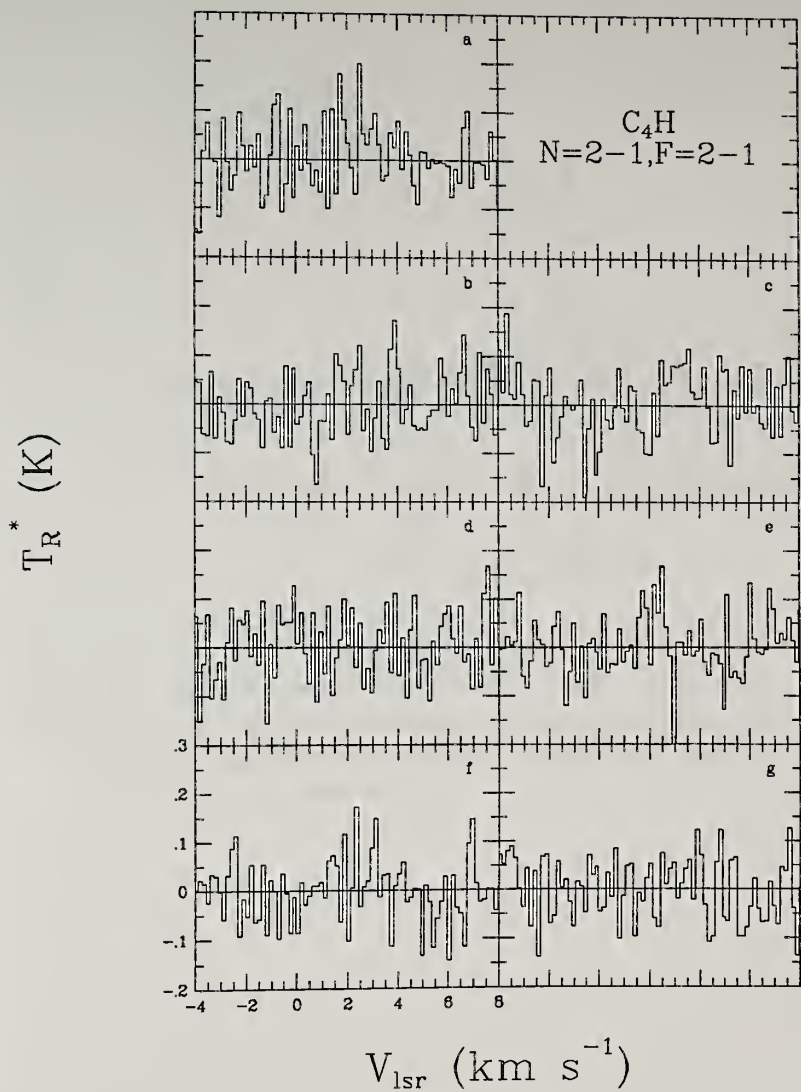


Figure 4.28 C_4H $N=2-1$, $F=2-1$ spectra in L134N from the NRAO survey. Each spectra is labeled with a letter corresponding to a survey position : a (1,3); b (1,1); c (0,2); d (0,0); e (-2,-1); f (-3,1); g (4,-1).



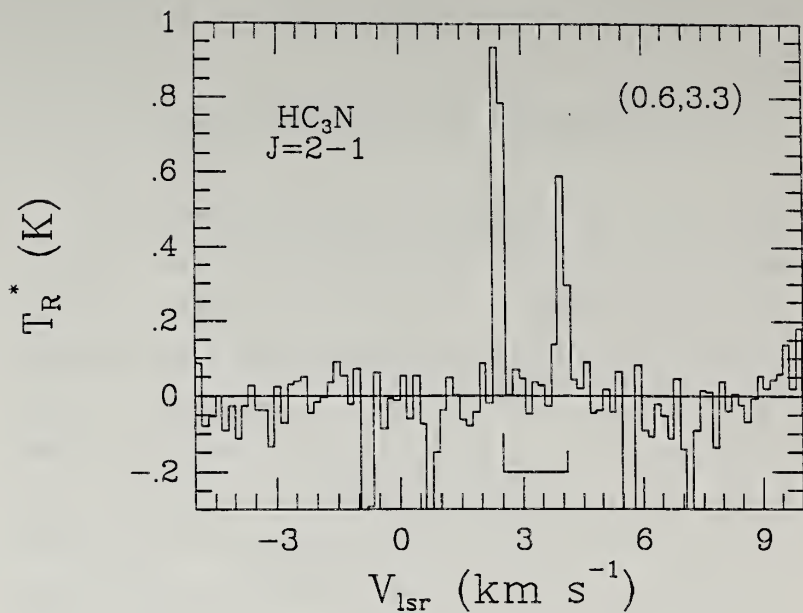


Figure 4.29 HC_3N $J=2-1$ spectra in L134N observed at the (0.6, 3.3) position. Bar below spectra indicates theoretical positions and LTE relative intensities for the $F=3-2$ (2.5 km s^{-1}) and $F=2-1$ (4.1 km s^{-1}) hyperfine components.

CHAPTER V

PHYSICAL PARAMETERS OF THE L134N MOLECULAR CORE

In this chapter the physical conditions in the L134N core are estimated. Each estimate requires that certain assumptions be made because a unique solution for physical parameters such as kinetic temperature and density is not possible. Problems which complicate the analyses include: measuring a spectral line intensity which samples all regions along a line of sight; structure may exist on size scales which are not resolved by the telescope beam, hence all observations are beam averaged; high optical depths of some transitions obscuring their emission from regions deeper within the cloud; and convolution of different effects, such as density structure, abundance gradients, and temperature variations, are difficult to separate. The combined results of the analysis of a number of spectral line observations will provide a clearer indication of the physical conditions in the L134N core.

a) CO Analysis

Carbon monoxide is the most abundant interstellar molecule with a permanent electric dipole moment and is excited under moderate densities and a wide range of temperatures. Hence, it is the most

commonly observed molecular species. In this study, the J=1-0 transition of ^{12}CO and C^{18}O were both mapped over the core region and surveyed at seven positions. When combined with the ^{13}CO J=1-0 mapping data from Chapter II, these spectra provide comparisons of the three isotopically substituted CO species with the same beam size and at over 150 of the same positions within the L134N core.

The equation which defines the line radiation temperature is,

$$T_R^* = [J_\nu(T_{\text{ex}}) - J_\nu(T_{\text{bg}})] (1 - \exp(-\tau)) \quad (5.1)$$

where

$$J_\nu(T) = hv/k (\exp(hv/kT) - 1)^{-1} \quad (5.2)$$

is the normalized Planck intensity (see Winnewisser, Churchwell, and Walmsley 1979). This equation can be solved for the excitation temperature, T_{ex} , if the ^{12}CO emission is assumed to be optically thick, that is $\tau \gg 1$. T_{bg} is the 2.78 K cosmic background radiation temperature and T_R^* is the observed line radiation temperature.

Solving equation 5.1 for the ^{12}CO excitation temperature at each map point indicates an excitation temperature gradient from about 9 K in the northwest region of the core to more than 12 K in the southeast, with a ^{12}CO excitation temperature of about 9 K in the peak emission region of NH_3 , C_3H_2 , and H^{13}CO^+ . A map of the ^{12}CO excitation temperature is shown in Figure 5.1. The ^{12}CO J=1-0 map of Sneli (1981) shows the ^{12}CO emission peaks to the south of the core region, consistent with the gradient observed here.

If the ^{12}CO is thermalized, that is collisions are the dominant means of populating the rotational levels, the excitation temperature is equal to the kinetic temperature of the molecular hydrogen gas. The degree to which all three isotopes of CO are thermalized is indicated in Figure 5.2. Plotted are the excitation temperatures for CO as a function of density. These curves were generated with a statistical equilibrium model using the large velocity gradient (LVG) approximation. In this model the column density of C^{18}O was assumed to be $1 \times 10^{15} \text{ cm}^{-2}$, and the column densities for ^{13}CO and ^{12}CO were scaled by factors of 89 and 489, respectively. These values represent the terrestrial abundance ratios of $^{13}\text{C}^{16}\text{O}/^{12}\text{C}^{18}\text{O}$ and $^{16}\text{O}/^{18}\text{O}$. The kinetic temperature within the core was chosen to be 12 K as indicated by the following NH_3 analysis. Line widths were taken to be 0.65 for C^{18}O , 1.25 for ^{13}CO , and 2.00 for ^{12}CO , which are representative of the observed spectra. The statistical equilibrium model is that used by Snell (1981) and the CO collisional cross sections were taken from Green and Chapman (1978). The basic assumption in a LVG model is that there are large velocity gradients between the cloud core and the observer such that a photon emitted in the center of the cloud, if not absorbed locally, will pass unabsorbed through the cloud because other molecules in its path are slightly Doppler shifted away from the rest frequency of emission. Although this is not necessarily true in L134N, this approximation allows for a numerical solution of the statistical equilibrium equations.

As shown in Figure 5.2, at extremely low densities the excitation temperature can be as low as that of the cosmic background, and at extremely high densities the excitation temperature approaches the kinetic temperature of the gas. Between the densities of 10 and 10^3 cm^{-3} curves for ^{12}CO $J=1-0$ and ^{13}CO $J=1-0$ undergo a steep rise as these transitions become thermalized. This rise occurs between 10^2 and 10^4 cm^{-3} for the more optically thin ^{18}O $J=1-0$ transition because the effects of photon trapping are not as important. At densities greater than 10^3 cm^{-3} , the ^{12}CO $J=1-0$ transition is thermalized and the densities in the L134N core regions are considered to be at least that high.

A central issue in the analysis of CO data is the optical depth of the observed transitions. The combination of the ^{12}CO data with the ^{13}CO and ^{18}O data allow a determination of the excitation temperature and optical depth of the observed spectral lines. In order to determine the optical depth of the ^{13}CO $J=1-0$ transition, equation 5.1 can be solved for the optical depth assuming the ^{13}CO excitation temperature is equal to the ^{12}CO excitation temperature. This may overestimate the ^{13}CO excitation temperature, since the ^{13}C isotope is less abundant than the ^{12}C isotope and ^{13}CO is less thermalized, but the error should not be very significant (Frerking, Langer, and Wilson 1982). The curves of Figure 5.2 also support this assumption for densities greater than about 10^3 cm^{-3} . The ^{13}CO optical depths determined in this manner over the region of the ^{12}CO map lie between 0.8 and 1.6 and a map of the ^{13}CO optical depth is shown in Figure

5.3a. An interesting feature of this map is that it shows ^{13}CO has the greatest optical depth in the region of the core where other molecular emission is observed, despite the fact that this region is not apparent in the ^{13}CO integrated intensity maps.

Similarly, the optical depth of the C^{18}O $J=1-0$ transition can be estimated by assuming the C^{18}O excitation temperature is the same as the ^{12}CO excitation temperature. In the case of C^{18}O this assumption is less valid than for ^{13}CO , particularly for densities less than 10^4 cm^{-3} where the C^{18}O excitation curve in Figure 5.2 is seen to be rising rapidly. The optical depths of C^{18}O derived in this manner at the survey positions range from 0.30 to 0.61, for a range of excitation temperatures from 8.5 K to 11.1 K determined from ^{12}CO at the survey positions, and are listed in Table 6.1. These values are typical of those obtained using the entire ^{12}CO and C^{18}O maps, hence an assumption of the C^{18}O $J=1-0$ transition being optically thin does not produce a significant error. Figure 5.3b shows a map of the C^{18}O optical depth. In general, the optical depth of C^{18}O correlates well with the C^{18}O integrated intensity, but peaks in the western extension of the core where the SO integrated intensity was shown to peak. Since, in the optically thin case, the integrated intensity, optical depth, and molecular column density are linearly proportional, the C^{18}O integrated intensity map must be indicative of the total C^{18}O column density provided the C^{18}O fractional abundance is constant across the region mapped.

Under the optically thin approximation the $C^{18}O$ column density is related to integrated line intensity by the equation:

$$N(\text{cm}^{-2}) = q_v / f_1 * \int T_R^* dv \text{ (K km s}^{-1}\text{)}. \quad (5.3)$$

The quantity

$$q_v = 3k \times 10^5 / 8\pi^3 \nu^3 \mu_{ul}^2 \text{ (s K}^{-1}\text{km}^{-1}\text{cm}^{-2}\text{)} \quad (5.4)$$

is the proportionality constant between the observed integrated intensity and the column density in the upper level of the transition and is listed in Table 4.3. The fractional population of the $J=1$ state, f_1 , is 0.44 assuming local thermodynamic equilibrium (LTE) at a typical excitation temperature of 9 K. A fractional abundance of 1.7×10^{-7} for $C^{18}O/H_2$ was found for the Taurus and rho Ophiuchus clouds by Frerking, Langer, and Wilson (1982). Since both of these clouds are in the solar neighborhood at approximately the same distance as L134N and have the same physical characteristics as L134N, the same $C^{18}O/H_2$ value will be assumed. The mass of the L134N core is determined to be 23 solar masses by summing the emission over the fully sampled map. Since the $C^{18}O$ $J=1-0$ line is not strictly optically thin, this mass represents a lower limit.

The extent to which the LTE column density, as described above, is a good approximation for $C^{18}O$ is represented in Figure 5.4. Plotted is the ratio of LTE column density to LVG column density as a function of density. The LVG modeling used in this figure assumed a constant $C^{18}O$ column density of $1. \times 10^{15} \text{ cm}^{-2}$ and a kinetic temperature of 12 K. The model generated the integrated intensity for the $C^{18}O$ $J=1-0$ transitions and a peak line temperature of the ^{12}CO $J=1-0$ transition for a ^{12}CO

column density of $5 \times 10^{17} \text{ cm}^{-2}$. A LTE column density for C^{18}O was determined using the C^{18}O J=1-0 integrated intensity and an LTE fractional population, f_1 , with the peak ^{12}CO J=1-0 line temperature used to determine the excitation temperature. This method mimics the above calculations and assumptions. It can be seen in Figure 5.4 that for densities greater than 10^3 cm^{-3} , both the LVG and the LTE methods yield comparable column densities. The LTE column density is less than the LVG column density at high densities because of the three assumptions inherent in equation 5.3. These are: (1) the Rayleigh-Jeans approximation is used for the Planck functions, (2) the cosmic background temperature is assumed to be much less than the line excitation temperature, and (3) the C^{18}O J=1-0 lines are taken to be optically thin.

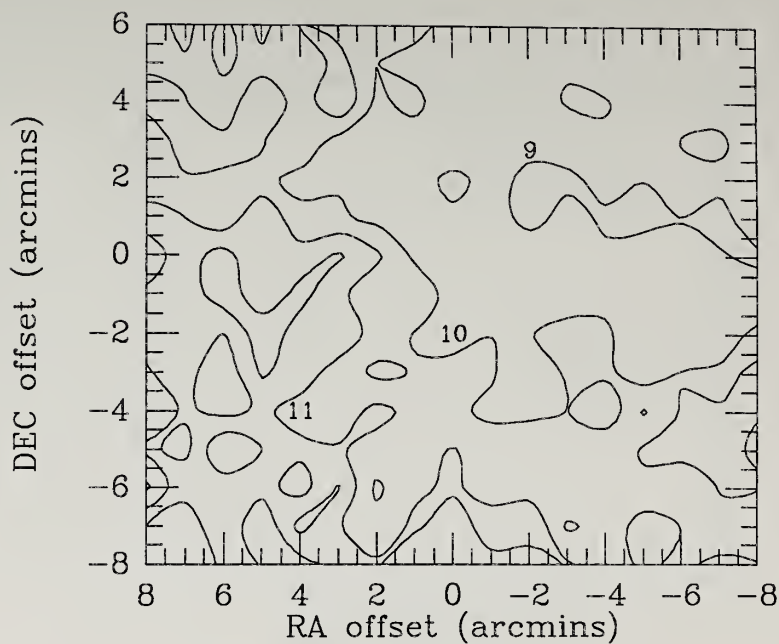


Figure 5.1 ^{12}CO J=1-0 excitation temperature across the L134N core. There appears to be a gradient from 9 K in the northwest to greater than 11 K in the southeast. Offset positions on the x and y axes are as previously defined.

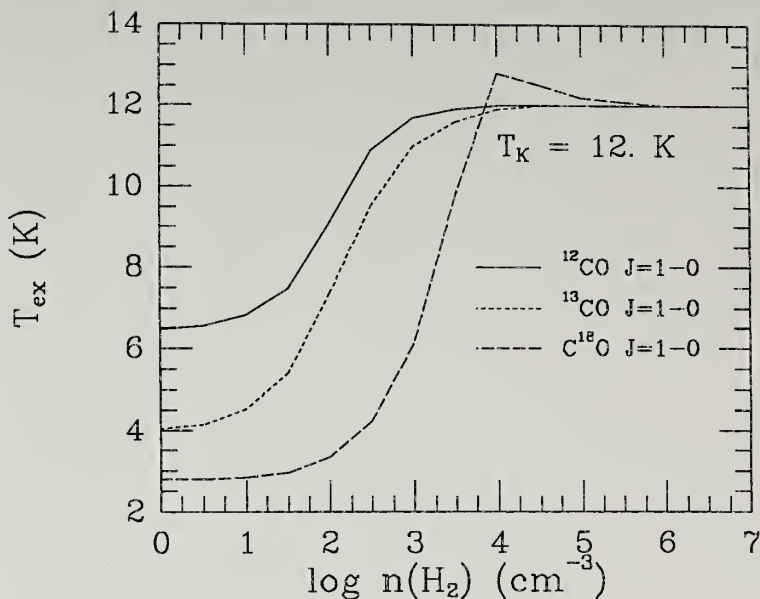
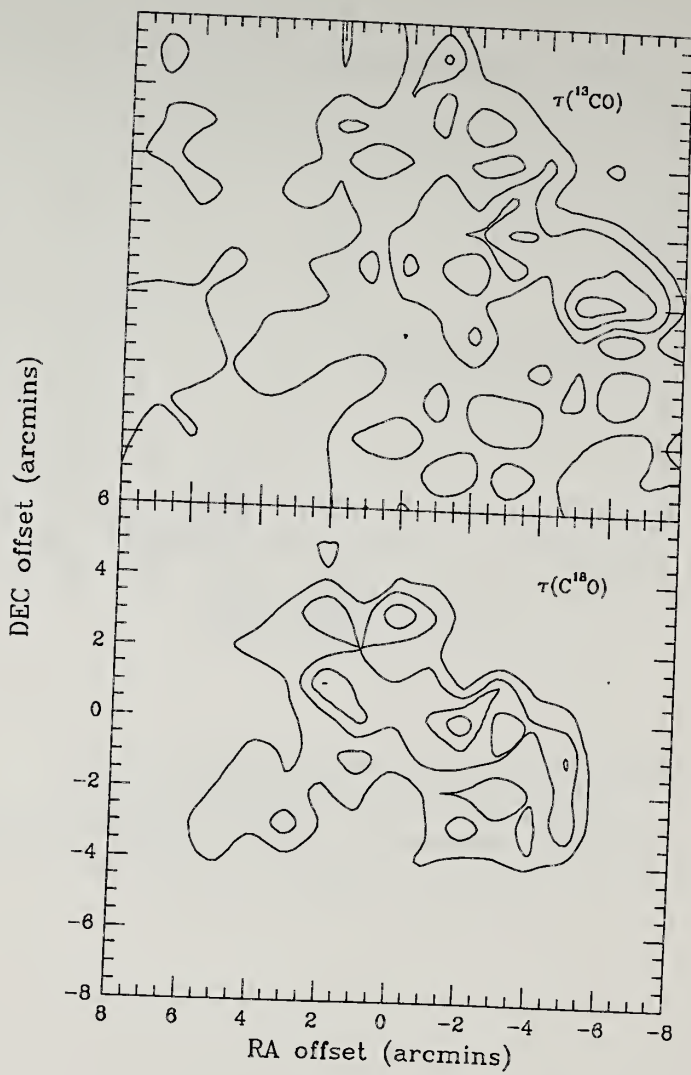


Figure 5.2 Excitation temperature as a function of density for three isotopes of CO. Curves were generated using a statistical equilibrium model in the large velocity gradient approximation for a kinetic temperature of 12 K; line widths of 0.65, 1.25, and 2.00 km s^{-1} ; and column densities of 1×10^{15} , 9×10^{16} , and $5 \times 10^{17} \text{ cm}^{-2}$ for C^{18}O , ^{13}CO , and ^{12}CO , respectively.

Figure 5.3 Maps of the optical depth of a) ^{13}CO $J=1-0$ and b) C^{18}O $J=1-0$ transitions. Contour levels for ^{13}CO are: 0.8, 1.1, 1.4, and 1.7. Contour levels for C^{18}O are: 0.40, 0.55, 0.70, and 0.85, one-half the values for ^{13}CO . Offset positions for the x and y axes are as previously defined.



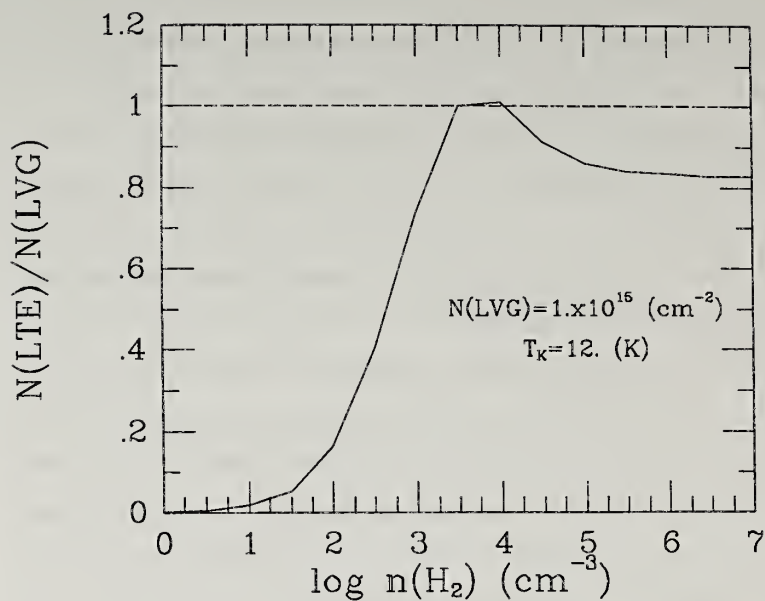


Figure 5.4 Ratio of LTE column density to LVG column density as a function of density. Methods for determination of column densities is described in the text. At densities greater than 10^3 cm^{-3} the LTE approximation appears to be valid.

b) ammonia analysis

The physical and chemical properties of the ammonia molecule have been reviewed by Ho and Townes (1983) and Switzer (1978). Despite low abundance predictions from models of ion-molecule chemistry (e.g., Graedel, Langer, and Frerking 1982; Millar and Freeman 1984a; Prasad and Huntress 1980b), the ammonia molecule is observed to be one of the most abundant species present in molecular clouds. A series of inversion transitions around 1.3 cm wavelength have long been regarded as excellent probes of the densest regions of cloud cores because of the high values of molecular hydrogen densities derived from their observations. These inversion transitions occur when the ^{14}N nucleus quantum mechanically tunnels through the plane formed by the three hydrogen atoms, which splits the (J,K) state into a doublet (except the (0,0) level). Such transitions are labelled by the molecular quantum numbers J and K.

An added advantage to observations of ammonia inversion transitions is that the ^{14}N nucleus has a nuclear spin angular momentum, $i=1$, which causes hyperfine splitting of the emission lines due to interactions of the electric quadrupole moment of the ^{14}N nucleus with the electric field of the orbiting electrons. Including higher order magnetic dipole interactions, the NH_3 (1,1) transition has a total of 18 hyperfine components (Rydbeck *et al.* 1977). However, only the five components caused by the electric quadrupole splitting are clearly resolved at the spectral resolution used in obtaining the

spectra in the L134N map, but the other components are visible as multiple peaks in five electric quadrupole lines. The NH_3 (1,1) spectra from the NRAO survey are shown in Figure 4.23.

The hyperfine components of the NH_3 (1,1) line allow for an independent measure of the optical depth of this transition if LTE is assumed (Ho and Townes 1983), which in turn allows for a determination of the excitation temperature. Analysis of the NH_3 (1,1) and NH_3 (2,2) spectra will be accomplished with the 'standard' model (Stutski and Winnewisser 1985b), since a full statistical equilibrium analysis (e.g., Sweltzer 1978; Stutski and Winnewisser 1985b) is beyond the scope of this study. Considerations of hyperfine anomalies (Stutski and Winnewisser 1985a) will also be neglected.

As with CO, the line radiation temperature is related to the excitation temperature and opacity of the emission line by equations 5.1 and 5.2. A beam filling factor might be included to account for the possibility that the ammonia is clumped into dense knots which are much smaller than the beam size such that the ammonia emission would not fill the beam. This effect is used to explain the NH_3 (1,1) excitation temperatures observed in giant molecular clouds (e.g., Wilson, Downes, and Biegling 1979; Ungerechts, Walmsley, and Winnewisser 1986). However, clumping on size scales smaller than the beam is not observed to occur in nearby dark clouds (Ungerechts, Walmsley, and Winnewisser 1980; Ho and Townes 1983), hence it is assumed here that the NH_3 emission uniformly fills the beam. In the case where hyperfine

components arise from the same transition, it is assumed that the excitation temperature for the satellite lines is the same as for the main line, and neglecting the small energy difference between the main and satellite lines, equation 5.1 gives:

$$T_{RM}^*/T_{RS}^* = (1 - \exp(-\tau_M)) / (1 - \exp(-\tau_S)) \quad (5.5)$$

and

$$\tau_M = a * \tau_S \quad (5.6)$$

where a is the LTE relative intensity of the satellite line to the main line. Therefore, the relative strengths of the hyperfine components allow for a solution of the optical depths of the line emission by the numerical solution of equations 5.5 and 5.6. Once the optical depth of a transition is determined, the excitation temperature can be found from equation 5.1. This method yields only an approximation for the optical depths since in reality the hyperfine satellite lines will have different excitation temperatures than the main line.

Since the inversion transitions occur much faster than the rotational and collisional transitions out of the (J,K) level, the inversion doublet can be well approximated by a two-level system. By balancing collisions, stimulated emission, and spontaneous emission into and out of the two inversion levels, a relation between the excitation temperature and molecular hydrogen density can be obtained:

$$n(H_2) = \frac{\beta A (J_v(T_{ex}) - J_v(T_{bg})) (1 + J_v(T_k))}{c (J_v(T_k) - J_v(T_{ex})) (h\nu/k)} \quad (5.7)$$

where A is the Einstein spontaneous emission coefficient from the upper to lower inversion level, T_k is the gas kinetic temperature, and C is the collisional cross section between the upper and lower levels (Green 1980). The factor of β is included to account for trapping of the NH_3 (1,1) photons. In a spherical LVG approximation, $\beta = (1 - \exp(-\tau))/\tau$ (Stutski and Winnewisser 1985b). Once the excitation temperature is calculated, the molecular hydrogen density in this approximation can be determined if a kinetic temperature is assumed.

1) map

In Figure 5.5 the total integrated intensity over all the hyperfine components is shown. This map is similar to the NH_3 (1,1) integrated intensity of Figure 4.2e which was only taken over the main hyperfine component, but the contour levels are approximately doubled for the total integrated intensities. Local thermodynamic equilibrium predicts that the main component of the electric quadrupole components should contain the same integrated intensity as the sum of the other four components, and that seems to be the case for these ammonia spectra.

The maps of Figure 5.6 show the results of the conversion of the measured line intensities into an optical depth, excitation temperature, and density distribution by analysis of the five electric quadrupole hyperfine lines from the NH_3 mapping observations. Figure

5.6a shows the optical depth of the main component as derived by the above procedure. The optical depth used to construct this map was actually the average optical depth of the main component derived from the integrated intensity of the four satellite lines. A map of the derived excitation temperature for the main hyperfine transition is shown in Figure 5.6b. This map closely mimics the maps of the peak line temperatures and integrated intensities in the previous maps. This result is not surprising since the optical depths of the main component are determined to be greater than one in spectra of significant line intensity. In such a case, the excitation temperature is approximately proportional to the line temperature plus a constant from the contribution of the cosmic background radiation.

Figure 5.6c shows a map which results from the calculation of the molecular hydrogen density derived from the NH_3 (1,1) inversion transition. The kinetic temperature was taken to be 12 K and the collision cross section coefficient is $1.0 \times 10^{-10} \text{ cm}^3 \text{ s}^{-1}$ (Green 1980). This map indicates two dense peaks in the core region and a general, narrow, dense filamentary structure from north to south. Two approximately equal density condensations occur at the positions (2,3) and (0,0).

ii) survey

The ammonia spectra surveyed at NRAO have a higher signal to noise than the spectra used in the map and, hence, are useful for a more detailed analysis. Of particular use is the fact that the NH_3 (1,1) and NH_3 (2,2) inversion transitions are very closely spaced in frequency. For example, during the NRAO survey, the autocorrelator was split such that the NH_3 (1,1) transition was observed in half the receiver, while the NH_3 (2,2) transition was simultaneously observed in the other half. Thus the relative intensities between the two transitions are independent of atmospheric fluctuations and telescope gain providing very accurate line strength ratios.

Parameters of NH_3 excitation and physical parameters for the L134N cloud core are derived from Gaussian lines fitted to the NRAO survey data. The optical depth and excitation temperature of the main NH_3 (1,1) line, and the molecular hydrogen density from the two level molecule approximation have been calculated for the NRAO survey data using the equations detailed above. These results are presented in Table 5.1, where the molecular hydrogen density is calculated based on the kinetic temperatures derived below. Also presented in Table 5.1 are the ^{12}CO J=1-0 excitation temperatures derived in the previous section for comparison to the temperatures associated with the NH_3 emission at the surveyed positions. It should be noted that the values tabulated in Table 5.1 reflect a scaling of the NRAO NH_3 data by a factor of 1.42. This was done in order to account for the fact that

the NRAO line temperatures are lower than those of the corresponding positions in the Haystack map by a mean of 42 ± 18 percent, although the NH_3 (1,1) main line temperature between the two sets of observations are highly correlated with a correlation coefficient, $R = 0.832$. Explanations for this include the possibility that maladjustment of the NRAO 43 m subreflector had defocused the NRAO observations as previously discussed. Considering the low aperture efficiencies of both antenna (0.25 and 0.33), this line temperature difference represents only about a 10 to 20 percent difference in antenna temperature. Since the NH_3 optical depths, excitation temperature, rotation temperature between levels (1,1) and (2,2), and kinetic temperature derived from the rotation temperature depend only on line ratios, these values are unaffected by the scaling.

Levels in which $J=K$ are called metastable levels, and the $K=J$ level is the lowest K level for any K -ladder. Radiative transitions have the selection rule $\Delta K=0$, hence only collisional transitions can change the relative populations among the K -ladders. Radiative transitions within a K -ladder occur much more rapidly than collisional transitions both within and between K -ladders, hence the $J=K$ metastable levels become heavily populated.

In addition, the possibility of the nuclear spins of the three hydrogen atom being parallel or not parallel gives rise to two different species of NH_3 . The ortho (spins parallel; $K=3n$, n an integer) and the para (spins not parallel; $K=3n+1, 3n+2$) species cannot

be mixed by either radiative or collisional transitions, since neither of these transitions are capable of changing spin orientation. In light of these considerations, the two lowest para NH_3 levels can be expected to be significantly populated in cold (10 K) clouds. These are the (1,1) level at 23.4 K and the (2,2) level at 64.9 K above the ground (0,0) level, however the (1,1) level is the ground state for para NH_3 . Since only collisional transitions are allowed between the (1,1) and (2,2) levels, the excitation temperature relating them in a Boltzmann distribution, T_{12} , should be a very good indicator of the kinetic temperature in the region of NH_3 excitation.

The rotation temperature, T_{12} , is defined by the Boltzmann distribution:

$$N_{22}/N_{11} = g_{22}/g_{11} \exp(-E_{12}/T_{12}), \quad (5.8)$$

where N is the column density of the specified level, g is the statistical weight of the specified level, and E_{12} is the energy difference between the (1,1) and (2,2) level, 41.5 K. The optical depth of the (J,K) level is related to the column density of the (J,K) level by the relation:

$$\tau_{JK} = 16\pi^3/3h (\int \ln 2/\pi) (1/\Delta\nu) \mu^2 K^2 J(J+1) N_{JK} X(T_{ex}), \quad (5.9)$$

where

$$X(T) = (1 - \exp(-h\nu/kT)) / (1 + \exp(-h\nu/kT)). \quad (5.10)$$

All quantities are as previously defined and $\Delta\nu$ is the full width half-power width of the NH_3 lines. Assuming that T_{ex} and $\Delta\nu$ are the same for the (1,1) and (2,2) inversion transitions, it can be shown using the above equations that:

$$T_{12} = \frac{-41.5 \text{ K}}{\ln\left\{\left(-0.2826/\tau_{M11}\right) \ln\left[1 - \left(T_{R22}^*/T_{R11}^*\right) \left(1 - \exp(-\tau_{M11})\right)\right]\right\}} \quad (5.11)$$

where τ_{M11} is the optical depth of the main line of the (1,1) transition. The calculated values of T_{12} for the seven positions observed in the NRAO survey are presented in Table 5.1.

The kinetic temperature of the cloud can be derived from T_{12} by solving the statistical equilibrium equations for the (1,1) and (2,2) levels assuming a two level molecule (Ungerechts, Walmsley, and Winnewisser 1980), which gives:

$$T_k = T_{12} / \{1 - (T_{12}/E_{12}) \ln[1 + C_{22-21}/C_{22-11}]\}. \quad (5.12)$$

The collisional rates between the (2,2) and (2,1) levels, C_{22-21} , and the (2,2) and (1,1) levels, C_{22-11} , can be estimated from the rates tabulated by Green (1980), such that the ratio C_{22-21}/C_{22-11} is approximately 0.45 at 12 K. The values of the kinetic temperature determined by this method are tabulated in Table 5.1. As previously noted, since the kinetic temperature determined in this manner depends only on the ratio of the NH_3 (1,1) and (2,2) lines, it should be relatively accurate and independent of any possible calibration errors. The results of this calculation are consistent with a constant kinetic temperature of 12 K across the core. Also listed in Table 5.2 are the NH_3 (1,1) column densities calculated using equation 5.9.

TABLE 5.1

NRAO NH₃ MODELING RESULTS

position	τ_{M11}	T_{ex} (NH ₃)	T_{ex} (¹² CO)	T_{12}	T_k	$\log n(H_2)$	N_{11}
		(K)	(K)	(K)	(K)	$\log(\text{cm}^{-3})$	(cm^{-2})
(0,0)	1.53	7.9	8.2	11.6	13.0	4.04	2.6×10^{14}
(-2,-1)	0.75	5.6	8.7	<10.6	<11.7	<3.77	1.0×10^{14}
(-3,1)	0.79	4.7	8.3	<11.5	<12.8	<3.51	9.9×10^{13}
(4,-1)	0.91	3.7	11.3	<14.9	<17.2	<3.04	6.9×10^{13}
(0,2)	1.20	7.5	9.3	11.3	12.6	4.02	2.0×10^{14}
(1,1)	1.06	5.9	8.7	<9.2	<10.1	<3.86	1.4×10^{14}
(1,3)	1.34	7.0	8.5	10.7	11.8	3.95	2.0×10^{14}

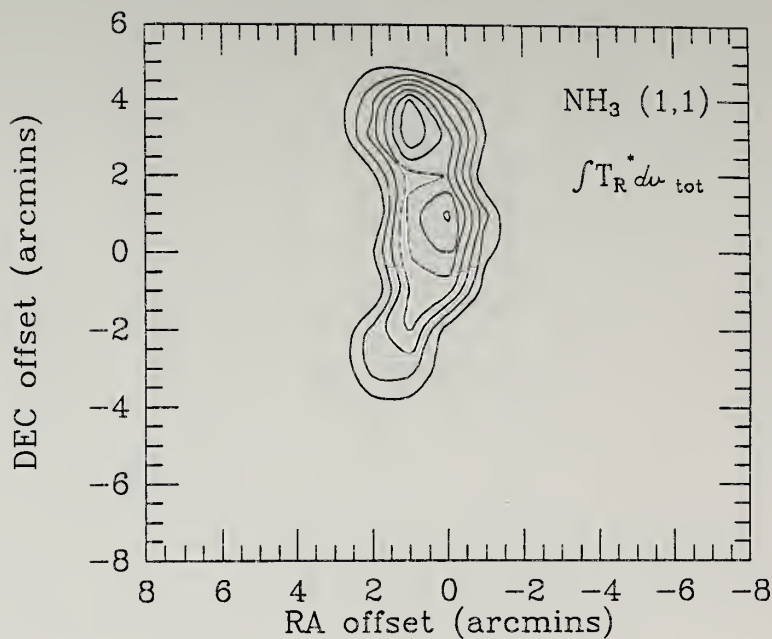


Figure 5.5 Contour map of the total integrated intensity of all NH_3 (1,1) hyperfine lines. Contour levels range from 3 to 9 K km s^{-1} in steps of 1 K km s^{-1} .

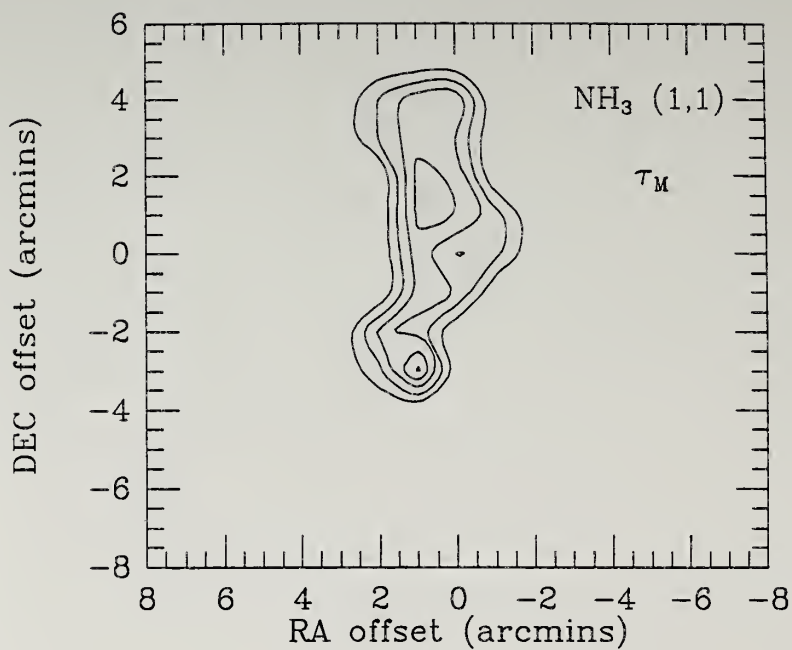


Figure 5.6 Series of contour maps which show NH_3 excitation parameters. a) NH_3 (1,1) main line optical depth which is the average of the main line optical depth determined from the four satellite lines. Contours range from 0.5 to 3.5 by 0.5.

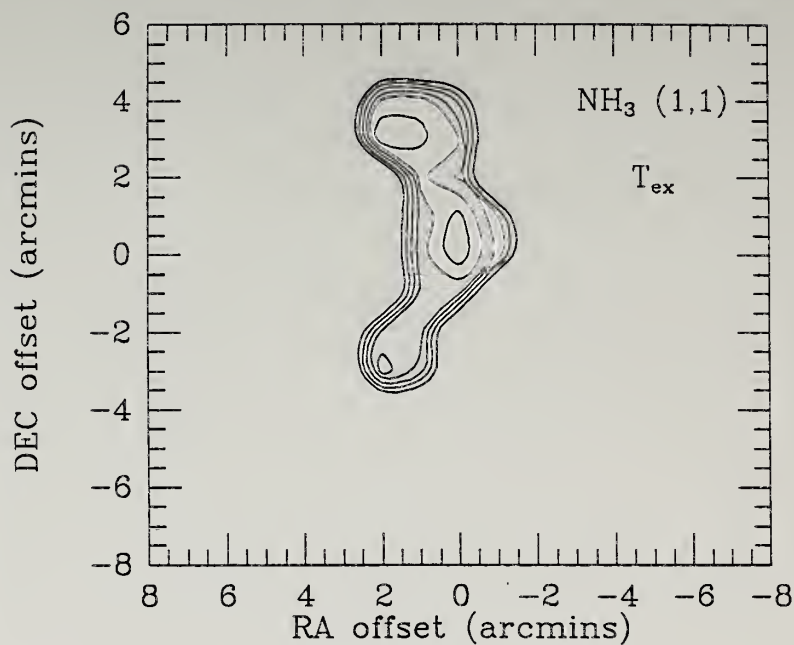


Figure 5.6 b) NH_3 (1,1) main line excitation temperature derived from the preceding optical depth map. Contours range from 4 to 9 K by 1 K.

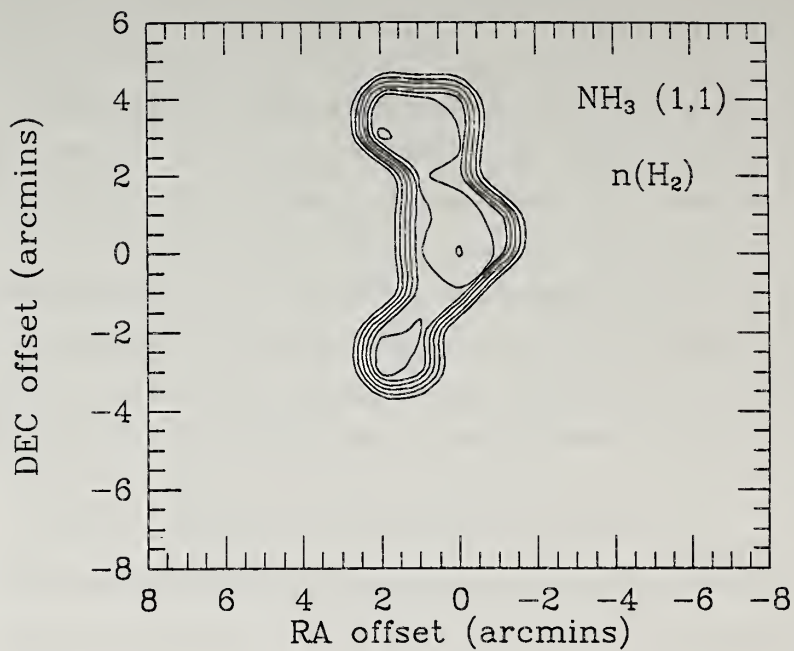


Figure 5.6 c) Molecular hydrogen density determined from the NH_3 (1,1) transition. Logarithmic contour levels range from $10^{1.5}$ to $10^{4.5} \text{ cm}^{-3}$ by $10^{0.5} \text{ cm}^{-3}$.

c) HC_3N analysis

Studies of more than one transition of a particular molecule can be beneficial in view of the fact that all the level populations of a molecule may not be in local thermodynamic equilibrium. Among the disadvantages of this type of analysis are that observations of different transitions taken with the same telescope often have vastly different beam sizes. On the other hand, if the observations are taken with different diameter telescopes so that the beam sizes are similar, calibration between the different telescopes becomes a problem.

HC_3N is a particularly useful molecule to observe for a multitransitional analysis since it has a small rotational constant, hence many accessible rotational transition lines in the centimeter and millimeter region of the electromagnetic spectrum. Also, the low value of the rotation constant allows for the LTE population of high J levels even in cold clouds. Relatively low populations in many levels means that the individual rotational transitions will all tend to be optically thin. In the molecular line survey of L134N, three transitions of the linear molecule HC_3N were observed. The $J=5-4$ and $J=9-8$ transitions were observed at FCRAO and the $J=2-1$ transition was observed at NRAO.

A major problem with these observations is that the $J=5-4$ beam size is twice as large as the $J=9-8$ beam size, with the $J=2-1$ beam size falling at an intermediate value. If the HC_3N emission is sharply

peaked within the area of the largest beam, comparisons of the intensities from these three transitions would be affected. Since the HC_3N emission has not been mapped in L134N the magnitude of this effect cannot be estimated, and uniform excitation across the beams of the three transitions observed will be assumed.

A single HC_3N J=2-1 spectra was observed at the position (0.6,3.3) where Churchwell, Nash, and Walmsley (1984) also observed HC_3N J=2-1 in L134N. Comparison of the values of T_R^* , V_{LSR} , and line width for both the F=2-1 and F=3-2 hyperfine components from those listed by Churchwell, Nash, and Walmsley with the observed spectra indicate excellent agreement to well within the listed formal errors. This would argue for at least the HC_3N observations being well calibrated.

1) rotation diagram

A multitransitional rotation diagram can be constructed from the observations of a number of optically thin transitions of a species (e.g., Schloerb et al. 1983). All the rotational energy levels are assumed to be populated by a Boltzmann distribution characterized by a rotational temperature, T_{rot} , such that,

$$N_l/g_l = N/Q_{\text{rot}} \exp(-E_l/T_{\text{rot}}), \quad (5.13)$$

where N is the total column density of the species, Q_{rot} is the partition function evaluated at the rotational temperature, and N_l , g_l , and E_l are the column density, statistical weight, and energy above the ground state, respectively, for the l^{th} energy level. For optically

thin transitions the column density of the l^{th} level can be represented by equation:

$$N_l = q_\nu \int T_R^* dv, \quad (5.14)$$

which leads to the equation

$$\ln \left| \frac{3k \int T_R^* dv}{8\pi^3 \nu S \mu^2} \right| = \ln \left| \frac{N}{Q_{\text{rot}}} \right| - \frac{E_l}{kT_{\text{rot}}}. \quad (5.15)$$

In this case, S is the line strength of the transition, ν is the frequency of the transition, μ is the molecular dipole moment, and the other quantities are as previously defined. Thus, a straight line can be fit to the data in which the slope of the line is $-1/T_{\text{rot}}$ and the y-intercept is $\ln [N/Q_{\text{rot}}]$.

The results of this analysis performed on the three observed transitions of HC_3N are presented in Figure 5.7. At the (0.6,2.9) position, the total HC_3N column density is found to be $4.7(\pm 0.3) \times 10^{12} \text{ cm}^{-2}$ for a rotational temperature of $4.9(\pm 0.3) \text{ K}$ and at the (0.7,0.7) position, the total HC_3N column density is found to be $3.3(-0.4,+0.6) \times 10^{12} \text{ cm}^{-2}$ for a rotational temperature of $4.7(-0.7,+0.8) \text{ K}$. The fact that these three transitions are fit very well by a straight line indicates the assumption of a Boltzmann distribution for the level populations is reasonable.

ii) statistical equilibrium calculations

Although the assumption of local thermodynamic equilibrium is the most simple means for determining level populations for the molecules observed, conditions that exist in the cores of molecular clouds may not, in general, support local thermodynamic equilibrium. Hence, as an alternative means of determining the physical conditions within the core of L134N, statistical equilibrium calculations using the large velocity gradient (LVG) approximation were performed to model the cloud. This is the same statistical equilibrium model used by Snell (1981) and the details of the model are presented there. Collisional cross sections for HC_3N are taken from Green and Chapman (1978). The techniques used here are the same as those used by Vanden Bout *et al.* (1983).

Using the statistical equilibrium model, a determination of the molecular hydrogen density as a function of the integrated line intensity ratio of the HC_3N 5-4 and the HC_3N 9-8 transitions was computed. Figure 5.8 shows the results of this calculation. For a HC_3N column density of $4.7 \times 10^{12} \text{ cm}^{-2}$ at the (0.6,2.9) position, the observed integrated intensity line ratio gives a molecular hydrogen density of $10^{4.3} \text{ cm}^{-3}$. At the (0.7,0.7) position the molecular hydrogen density is determined to be $10^{4.5}$. These values of the density from HC_3N transitions agree very well with those obtained from the NH_3 map and the scaled NH_3 survey results. A possible overestimation of the molecular hydrogen density by this method may be

attributed to the approximation of uniform emission across the different beam sizes. If the emission is peaked within the two arcminute J=5-4 beam, the J=5-4 integrated intensity would be larger if the beam size were smaller. This would lead to a smaller value for the molecular hydrogen density, and may be especially true at the (0.6,2.9) position where the NH_3 map is sharply peaked. Hence, the values determined here must be considered upper limits. Since these densities agree well with those determined at the positions from the NH_3 (1,1) mapping observations, it would seem that both molecules are probing the same region of the cloud.

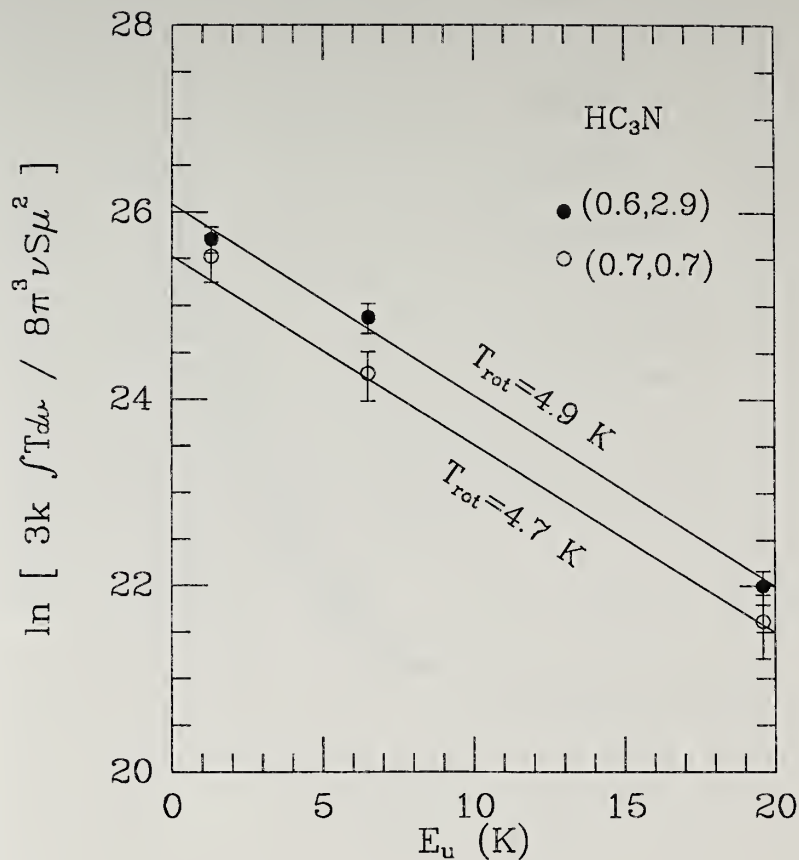


Figure 5.7 Rotation diagram for three HC₃N transition at two positions in L134N. Slope of the line indicates rotation temperature of a Boltzmann distribution for the level populations. The y-intercept indicates column density divided by the partition function.

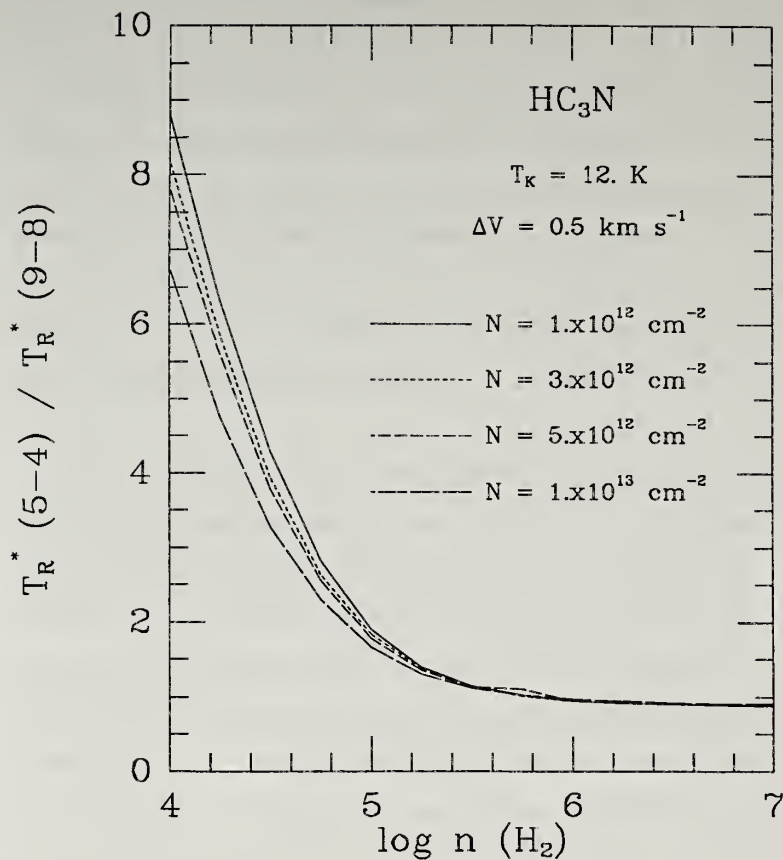


Figure 5.8 $\text{HC}_3\text{N } J=5-4 / \text{HC}_3\text{N } J=9-8$ line ratio as a function of density derived using the LVG model. The kinetic temperature was fixed at 12 K and the line widths were chosen to be 0.5 km s^{-1} . Four curves span the range of column densities at positions where both lines were detected in L134N.

d) hyperfine structure

Under the circumstance that a transition exhibits one or more hyperfine lines, the relative intensity of the hyperfine lines can be used to determine the optical depth and excitation temperature of that transition. In the case of all molecules in the spectral line survey where hyperfine splitting occurs, except for C_4H , it is due to the $i=1$ nuclear spin of the ^{14}N nucleus. For N_2H^+ , the two nitrogen nuclear spins produce nested line splitting.

The basic premise used in the optical depth determination is that at high optical depths, the stronger of the hyperfine lines saturates and the relative intensity of the other hyperfine components increases. Under these conditions, the main line can never have an intensity less than that of the satellite lines. However, self-absorption from low density foreground gas can produce anomalous line intensities (Irvine and Schloerb 1984). When the optical depth of the main line is low, the hyperfine lines should be in their LTE ratios.

Using equation 5.1 and the assumption that the excitation temperature of the satellite lines is the same as the main line, the optical depths are related to the measured line intensities by equation 5.1 if $Q = T_{R M}^*/T_{R S}^*$ and $\tau_S = a\tau_M$ where a is the LTE relative intensity of the satellite line with respect to the main line. Solving the equation,

$$(Q-1) - Q \exp(-a\tau_M) + \exp(-\tau_M) = 0, \quad (5.16)$$

for τ_M produces the main line optical depth. In the limit that τ_M becomes very large, Q approaches one. That is to say that the main line saturates and the satellite line approaches the main line intensity. In the limit that the optical depth becomes very small, Q approaches $1/a$. This is the limit where all lines are optically thin. Figure 5.9 shows the solution of equation 5.16 for three values of a . In practice, when Q becomes small and the optical depth becomes large it is difficult to accurately determine τ_M . It can be seen from Figure 5.9 that, in this regime, a small error in the measurement of the line intensities produces a large error in the derived optical depth. This is especially true for the larger values of a . Hence, it is much easier to determine the optical depth of the NH_3 (1,1) transition where $a=0.2$ and the main/satellite intensity ratio is large, than it is to determine the optical depth from the H^{13}CN $J=1-0$, $F=1-1$ transition where $a = 0.6$. The $F=0-1$ lines are too weak for an accurate determination of optical depth, which is unfortunate because of their low value of $a = 0.2$. Use of the integrated intensity ratios eliminates the possibility of a spike in line giving a spurious optical depth, but assumes equivalent line widths for the main and satellite lines.

This technique has already been employed in the determination of the NH_3 (1,1) optical depths in the previous section. Of the other transitions in both the FCRAO and NRAO surveys, the HN^{13}C $J=1-0$, HC_3N $J=5-4$, and HC_3N $J=9-8$ hyperfine splitting is not resolved. This leaves

H^{13}CN $J=1-0$, HC_3N $J=2-1$, N_2H^+ $J=1-0$, and C_4H $N=2-1$ transitions with observable hyperfine splitting.

Solution of the above equations for the H^{13}CN $J=1-0$, $F=2-1$ and $F=1-1$ lines yields main line ($F=2-1$) optical depths of 3.1 (-0.4,+0.6) at (0.6,2.9) and 3.0 (-0.5,+0.7) at (0.7,0.7) for a LTE ratio of integrated intensity ratio of $F=2-1/F=1-1 = 0.6$. This indicates that this transition is not necessarily optically thin, at least in the densest region of the core, and the derived optically thin column densities are actually lower limits. Corresponding excitation temperatures derived from equation 5.1 are 3.1 K at (0.6,2.9) and 3.0 K at (0.7,0.7). Errors in the optical depth of the magnitude indicated do not produce significant errors in the excitation temperature. The H^{13}CN spectrum at the (-0.8,0.4) position is too weak to attempt a measurement of hyperfine ratios.

The HC_3N $J=2-1$ transition has two strong components, the main $F=3-2$ line, with 46.7% of the total $J=2-1$ emission, and the satellite $F=2-1$ line, with 25% of the total $J=2-1$ emission (Townes and Schawlow 1955), that can be used to determine the optical depth of the transition ($a=0.536$ in equation 5.16). At the NRAO survey (1,3) position and the (0.6,3.3) position the optical depth of the $F=3-2$ line is determined to be 1.0 and 0.5, and the excitation temperatures 3.8 K and 5.0 K, respectively. Formal errors for these optical depths are difficult to determine, but relatively large, due to the high value of a and its sensitivity to changes in Q (see Figure 5.9). The excitation

temperatures agree well with the HC_3N rotation temperature previously found at the nearby FCRAO survey position. The $(-2,-1)$ position had a non-detection of both hyperfine lines and at the other five positions surveyed in HC_3N $J=2-1$ the lines are consistent with the $F=3-2$ line being optically thin.

The hyperfine structure of the N_2H^+ $J=1-0$ transition is complicated by the two ^{14}N atoms. However, the first order splitting occurs as if there were only one ^{14}N atom and the integrated intensity of the ΔF_1 transitions are in the LTE ratios of 5:3:1. Using the integrated intensities of the $F_1=2-1$ and $F_1=1-1$ line groups only two N_2H^+ spectra indicate high optical depths. These are the $(0.7,0.7)$ and the $(-0.8,0.4)$ positions where the optical depths are determined to be 1.8 ± 0.2 and 1.9 ± 0.2 and the excitation temperatures are 4.6 K and 4.1 K, respectively.

As listed in Table 4.2a, three hyperfine components of the $N=2-1$ transition of C_4H were detected at the $(1,3)$ position and two components were detected at the $(0,2)$ position. At the two other positions of the NRAO survey only a single hyperfine component was detected. Based on the theoretical LTE hyperfine ratios given by Guellin, Friberg, and Mezaoui (1982), there is no saturation of the main component, hence the hyperfine lines are consistent with C_4H $N=2-1$ being optically thin in the L134N core.

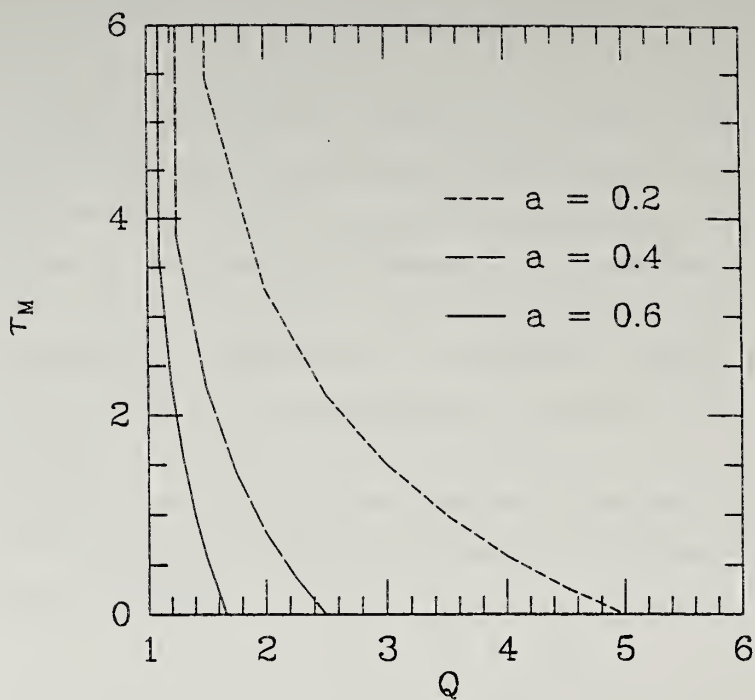


Figure 5.9 Plot of main hyperfine line optical depth as a function of main line to hyperfine intensity ratio. Three curves are for different LTE line ratio values.

e) Isotopic variations

Observations of isotopically substituted transitions of the same molecule can be useful in estimating the optical depths of transitions without having to resort to the optically thin approximation. However, an assumption about the relative abundance of the isotopically substituted atom must be made. Studies (e.g., McCutcheon et al. 1980; Wilson, Langer, and Goldsmith 1981) have shown that in local dark clouds the elemental isotopic abundances are consistent with terrestrial values. Hence, due to the lack of any contrary evidence about such variations in local dark clouds and the proximity of L134N to our solar system, a terrestrial abundance for all isotopes will be assumed in this study.

Using equation 5.5 and assuming that the excitation temperature is the same for both isotopic species, the optical depth can be numerically solved for from equation 5.16. In this case, τ becomes the inverse of the fractional abundance of the isotopically substituted atom and $Q = T_R^*(1) \nu(2) / T_R^*(2) \nu(1)$ where (1) represents the most abundant species and (2) represents the isotopically substituted species. In the FCRAO survey three cases exist where isotopically substituted species were observed along with the main species. In both CS J=2-1 and SO N, J=2,3-1,2 transitions, the ^{34}S atom is substituted for the more common ^{32}S atom and for H^{13}CO^+ J=1-0, the double substitution ^{12}C for ^{13}C and ^{18}O for ^{16}O results in HC^{18}O^+ . The

terrestrial abundance ratio of $^{34}\text{S}/^{32}\text{S}$ is 22.5, $^{13}\text{C}/^{12}\text{C}$ is 89.1, $^{16}\text{O}/^{18}\text{O}$ is 489, and hence the double ratio $^{13}\text{C}^{16}\text{O}/^{12}\text{C}^{18}\text{O}$ is 5.5.

The results of solving equation 5.16 for the CS and SO transitions are presented in Table 5.2. Once the optical depth is known, equation 5.1 can be used to find the corresponding excitation temperature. These values are actually lower limits to the optical depths since self-absorption is evident in some of the CS and SO spectra and an undeterminable amount may exist in the other spectra. A correction for the self-absorption would produce a higher value for the peak and integrated intensity of the main isotope, hence a higher value of Q , and a lower optical depth. Rydbeck *et al.* (1980) find a slightly lower value of 2.8 for the optical depth of the $N, J=0, 1-1, 0$ transitions of SO at 30 GHz. However, this is consistent with the results obtained here since the 30 GHz spectra do not show self-absorption.

If the values obtained for the optical depths of SO and CS are upper limits, the values obtained for the excitation temperatures are lower limits. Again, this is consistent with the results of Rydbeck *et al.*, who found a value of 5 K for the excitation temperature of the 30 GHz line of SO. It seems reasonable to assume that the SO and CS line observed in this study are subthermally excited at excitation temperatures of approximately 5 K.

For the case of the single HC^{18}O^+ $J=1-0$ observation at the (0.6, 2.9) position, there is no solution to equation 5.16 for the

observed radiation temperature ratios. This indicates that to within the errors of the observation, both the H^{13}CO^+ $J=1-0$ and the HC^{18}O^+ $J=1-0$ transitions are optically thin at the (0.6,2.9) position and the double abundance ratio $^{13}\text{C}^{16}\text{O}/^{12}\text{C}^{18}\text{O}$ is given by the ratio of the H^{13}CO^+ and HC^{18}O^+ integrated intensities to be 7.4 ± 2.6 . This ratio is consistent with the terrestrial value of 5.5.

TABLE 5.2

RESULTS OF ISOTOPIC VARIATIONS

position	$\tau(\text{CS})$	$\tau(\text{C}^{34}\text{S})$	$T_{\text{ex}}(\text{CS})$ (K)	$\tau(\text{SO})$	$\tau(\text{S}^{34}\text{O})$	$T_{\text{ex}}(\text{SO})$ (K)
(0.6, 2.9)	6.3	0.28	3.7	4.0	0.18	4.5
(0.7, 0.7)	9.5	0.43	3.5	9.0	0.40	4.4
(-0.8, 0.4)	1.9	0.08	4.0	3.3	0.15	4.9
(-1.4, -0.8)	4.9	0.22	3.8	8.7	0.39	5.0
(-2.8, 0.8)	5.3	0.24	3.9	3.8	0.17	4.4
(-2.3, 2.0)	1.3	0.06	4.3	5.3	0.24	4.0
(3.7, -1.2)	4.8	0.21	3.8	3.2	0.14	4.3

f) excitation summary

In the previous sections, excitation of various molecular line emission has been used to probe the physical conditions within the molecular core of L134N. The two physical parameters which have been addressed are the gas kinetic temperature and the molecular hydrogen density. Parameters which specify line emission have also been investigated in cases where either isotopic line measurements or hyperfine structure have permitted a determination of the optical depth and excitation temperature of a transition. In all cases a degree of subthermal excitation exists in which the line excitation temperature is less than the 12 K kinetic temperature of the core region as determined from the two level approximation for para-ammonia. Except for CO, the determined excitation temperatures are all approximately 5 K. CO excitation temperatures are higher over the core region, but this is expected since the optically thick ^{12}CO is thermalized at high densities and does not probe the dense core. Since the less optically thick C^{18}O samples deeper into the core, the C^{18}O excitation temperature estimates may be too high.

Peak densities as determined from the NH_3 (1,1) inversion transition and the statistical equilibrium calculations of two transitions of HC_3N are about $3 \times 10^4 \text{ cm}^{-3}$. This value is consistent with the densities determined in L134N from the formaldehyde observations by Snell (1981). In addition, estimates from the H^{13}CN $J=1-0$ and N_2H^+ $J=1-0$ transitions with the previously described

statistical equilibrium model also indicated densities of approximately $3 \times 10^4 \text{ cm}^{-3}$ at the (0.6,2.9) and (0.7,0.7) positions, while an estimate at the (-0.8,0.4) position using N_2H^+ indicates a slightly lower density. These density estimates were determined by matching the modeled excitation temperature for the transition with the excitation temperature determined above for a 12 K kinetic temperature, a line width of 0.5 km s^{-1} , optically thin column densities, and collision cross sections given by Green (1975) for N_2H^+ and Green and Thaddeus (1974) for HCN. A total particle density would be 1.15 times these molecular hydrogen densities assuming a H_2 fractional abundance of 0.855, a He fractional abundance of 0.145 (Allen 1981), and no atomic hydrogen in the core region.

As with any parameter determined from a spectral line used to probe the conditions in a molecular cloud, the kinetic temperature and molecular hydrogen density are averaged over the column defined by the beam size. In addition, mapping the emission from a molecular transition samples the distribution of emission and not directly any physical parameter of the cloud. Hence, densities determined from a map of NH_3 (1,1) emission do not necessarily map the density distribution of molecular hydrogen within the cloud core, but reflect densities over the region in which the NH_3 (1,1) line is excited, averaged over the area of the beam and depth of the cloud, and convolved with the molecular abundance distribution.

With this in mind, consider the notion that a certain molecule's emission probes the region of a cloud determined by its characteristic density, n^* , (Evans 1980), where

$$n^* = A/C (1 - \exp(-h\nu/kT_k))^{-1}. \quad (5.17)$$

A and C are the coefficients for spontaneous emission and collisional cross section rates, respectively, for transitions from the upper to the lower level. If this were the case, the transition with the highest n^* would probe the densest region of the core and hence be the least spatially extended. Figure 5.10 shows a plot of $\log n^*$ vs. the characteristic diameter, which is the square root of the area greater than the half power integrated intensity of each of the six maps. One would expect the transitions to lie along a line of negative slope with the highest n^* 's having the least spatial extent and the lowest n^* 's having the greatest spatial extent. The major discrepancy is $\text{NH}_3(1,1)$ which is the least spatially extended of the six despite its low value of n^* . A possible explanation for this discrepancy is that the conditions which favor the chemical production of the molecule are altering the distribution of the molecule's emission expected from purely physical arguments. For example, NH_3 might form from a precursor ion or molecule that can only exist at high densities. This notion will be further explored later in the context of chemical models for cloud cores.

As expected, $\text{C}^{18}\text{O } J=1-0$ has a low characteristic density and seems to be probing a lower density envelope around the core. $\text{H}^{13}\text{CO}^+ J=1-0$ and $\text{C}_3\text{H}_2 1_{10}-1_{01}$ have high values of n^* and probe the dense core.

Although CS J=2-1 and SO N,J=2,3-1,2 also have high values of n^* , their lines indicate high optical depths (Table 5.2), hence their emission from the high density core may be obscured by emission from lower density regions along the line of sight.

Line widths from the high signal-to-noise survey data do not show any significant indication of variation within the core region. The average line widths over the seven surveyed positions are not correlated with the characteristic density of the molecular emission. Survey spectral line widths compared with the full-width at half integrated intensities of the maps for the same transitions show only a slight correlation. Except for ^{12}CO , which at an average line width over 2 km s^{-1} is a factor of two larger than the next highest average line width, line widths unaffected by self-absorption or hyperfine broadening range from 0.26 to 0.65 km s^{-1} . These line widths are not much greater than the thermal width of 0.06 to 0.11 km s^{-1} at 12 K for the molecules considered in this study, indicating a relatively quiescent core.

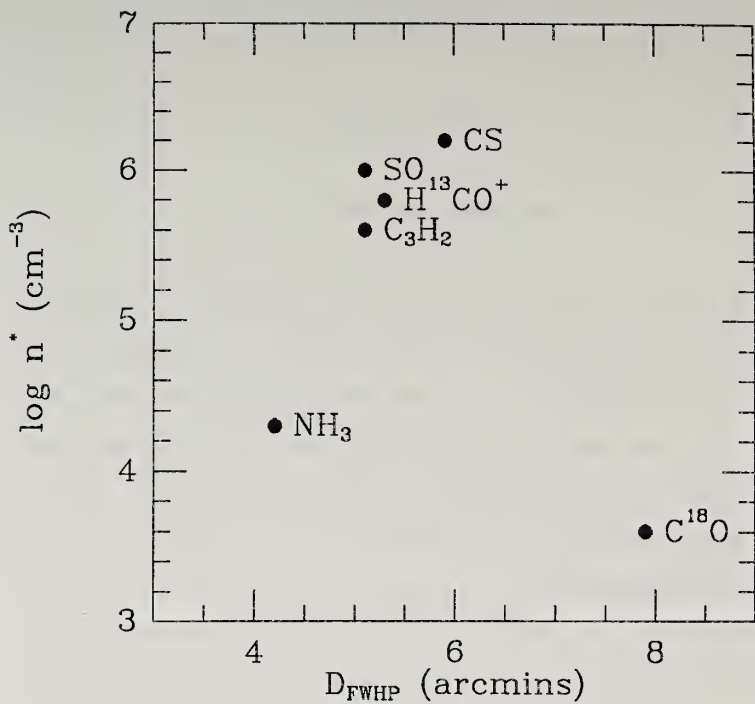


Figure 5.10 Characteristic density as a function of size for six transitions mapped in L134N.

CHAPTER VI

CORE CHEMISTRY

a) Chemical Abundances

In order to compare the results of the molecular survey to chemical models (e.g., Prasad and Huntress 1980a; Leung, Herbst, and Huebner 1984; Millar and Freeman 1984a, b), the abundance of a molecular species with respect to molecular hydrogen must be estimated. Determination of true chemical abundances requires a detailed knowledge of the number density of the species in question, the number density of molecular hydrogen, and the volume over which these two quantities are measured. In practice, all of the above quantities are difficult to determine. However, an approximation to the chemical abundance of a species can be made by consideration of the observed column density (Irvine et al. 1985). The abundance, $f(X)$, of a species, X , will be assumed to be the ratio of the observed species column density, $N(X)$, to the total molecular hydrogen column density, $N(H_2)$. The abundances determined in this manner are averaged abundances over the area of the beam and through the entire column of gas in the cloud.

Using equation 5.1 and the optically thin approximation, the beam averaged column density in the upper level of a transition is related to the total integrated intensity of that transition at each position in the cloud by:

$$N_u = q_v \int T_R^* dv / (1 - J_v(T_{bg})/J_v(T_{ex})), \quad (6.1)$$

where q_v is a constant for each molecular transition and is listed in Table 4.3. For rotational transitions, $q_v = 3k \times 10^5 / 8\pi^3 \nu |\mu_u|^2$ ($s K^{-1} km^{-1} cm^{-2}$), and for the NH_3 inversion transitions, N_u represents the column density of the (J,K) level with

$$q_v = 3h \times 10^5 / 8\pi^3 |\mu_u|^2 T_{ex} X(T_{ex}) \quad (s K^{-1} km^{-1} cm^{-2}).$$

The quantity $X(T_{ex}) = [1 - \exp(-h\nu/kT_{ex})] / [1 + \exp(-h\nu/kT_{ex})]$ and other quantities are as previously defined.

In order to determine the total column density for a given molecular species the fractional population of the upper level of the observed transition must be estimated. This can be accomplished for all the surveyed transitions by assuming that the level populations of the rotational transitions observed are in local thermodynamic equilibrium at the excitation temperature of the transition. An alternative method would be to use statistical equilibrium calculations to determine the level populations, but collisional cross sections are known only for a small fraction of the species observed. The LTE fractional population of each level can be approximated using the formalism detailed in Townes and Schawlow (1955). Using this approximation, the total column density for each molecule can be found

from $N_{\text{tot}} = N_u / f_u$ where f_u is the fraction of molecules in the upper level.

Thus, the determination of the upper level column density requires an assumption about the excitation temperature of the transition. As was shown previously, it is reasonable to assume that the C^{18}O J=1-0 excitation temperature is the same as the ^{12}CO J=1-0 excitation temperature over the region under consideration. Results of hyperfine, isotopic, and multitransitional analyses in the previous chapter indicate that the typical excitation temperatures in the core region for CS, SO, HC_3N , H^{13}CN , N_2H^+ , and NH_3 are approximately 5 K. Hence, it is reasonable for an excitation temperature of 5 K to be assumed in the calculation of the LTE upper level fractional population for all transitions at all survey positions except for C^{18}O J=1-0 and both NH_3 transitions. The discussion in Chapter V indicated that the level populations of NH_3 cannot be represented by a Boltzmann distribution because of the overpopulation of the metastable levels. Hence for NH_3 , a rotation temperature, T_{12} , of 11 K will be used to characterize the relative population between the (1,1) and (2,2) levels.

Once the total column density for an optically thin molecule is known, its abundance relative to any other optically thin molecule can be determined from the ratio of the two column densities. Hence, the next step in obtaining the absolute abundances of the surveyed molecules is to compare the total column densities for two optically thin surveyed molecules and determine the relative abundances of these

two molecules. $C^{18}O$ is chosen as the molecular species with which the others will be compared because: (1) the $C^{18}O$ $J=1-0$ transition was not found to be optically thick, and (2) previous studies (Frerking, Langer, and Wilson 1982) have found that $C^{18}O$ $J=1-0$ column density is correlated with visual extinction, hence molecular column density, in cold molecular clouds.

In order to determine the molecular abundances with respect to H_2 , an absolute abundance for $C^{18}O$ is necessary. The value of $N(C^{18}O) / N(H_2)$ of 1.7×10^{-7} found for the rho Oph and Taurus dark clouds by Frerking, Langer, and Wilson (1982) and will be assumed to hold in L134N. This is reasonable since L134N is at the same distance from the solar system as are rho Oph and Taurus, and all three clouds are physically similar. Also, Langer et al. (1980) find a fractional abundance of 2.2×10^{-7} for $C^{18}O$ holds in the center of B5, B335, and L1262 as long as the visual extinction is greater than four. Since the $C^{18}O$ $J=1-0$ transition traces the molecular hydrogen density, and since CO is easily produced, there are no reasons to believe the fractional abundance of $C^{18}O$ with respect to molecular hydrogen should change across the core of the cloud, and a value of 1.7×10^{-7} for the absolute abundance of $C^{18}O$ will be assumed constant at each surveyed position. In this manner the absolute abundances for all the surveyed molecules will be estimated.

This method for determining molecular fractional abundances underestimates the true fractional abundance for a number of reasons.

(1) The assumption of transitions being optically thin and column density reflecting actual number density through the cloud is not necessarily true as seen in Chapter V. A correction factor to the column density to account for optical depth of $\tau/[1-\exp(-\tau)]$ may be applied if the optical depth is accurately known. Since the optical depth cannot be estimated for most of the observed transitions, this correction will not be applied. (2) The $C^{18}O$ $J=1-0$ emission may extend over a much larger region along the line of sight through the cloud than other molecular emission. The $C^{18}O$ $J=1-0$ emission is thought to be excited in regions of lower density outside the core defined by the NH_3 and C_3H_2 emission, hence may not sample the same volume within the cloud along the line of sight of the telescope beam. This effect would cause an underestimate of the molecular abundances in the high density core since low density $C^{18}O$ emission would be contaminating the beam averaged $C^{18}O$ column density. In this regard, it must be remembered that the fractional abundance estimates are averaged along the line of sight through the cloud as well as within the telescope beam. (3) Another effect which would underestimate the true absolute molecular abundance would be that molecules may exist in regions within the beam but are not excited.

Tables 6.1 and 6.2 summarize these calculations for the FCRAO and NRAO surveys, respectively. C_3H_2 $1_{10}-1_{01}$ data interpolated from the C_3H_2 map and presented in Table 4.2c are included in Table 6.1. The first three columns list the position, species and transition used in the abundance calculation. The fourth column lists the excitation

temperature used in the calculation of the optical depth and upper level column density. The fifth column lists the optical depth as determined from equation 5.1 using the peak line radiation temperature and assuming the listed excitation temperature. These values of the optical depth correspond to the assumed excitation temperature, hence can only be regarded as estimates. The next column lists the derived upper level column density and the seventh column lists the LTE fractional population of the upper level of the observed transition at the corresponding excitation temperature. The fractional populations were calculated using the excitation temperature listed except for the NH_3 (1,1) and NH_3 (2,2) transitions where the rotational temperature between the (1,1) and (2,2) levels, T_{12} of 11.3 K was determined to more accurately represent the LTE population distribution in these two levels. These column densities are determined in the optically thin approximation and are not corrected for optical depth. If the true line excitation temperature is less than 5 K, as indicated in some transitions in the preceding chapter, the optical depth will be greater than the estimate listed in this table. The total molecular column density and absolute fractional abundance as found by the method outlined above are listed in the last two columns. For the results of the NRAO survey tabulated in Table 6.2, the C^{18}O column density at the NRAO survey positions was determined from the spectra at these positions in the C^{18}O J=1-0 map. The column density of the upper level for the NH_3 (1,1) and NH_3 (2,2) transitions represent the total column density of the (J,K) level, and the (1,1) column densities estimated

here are comparable to those found from the derived optical depth in Chapter V.

Cases exist in Tables 6.1 and 6.2 where two transitions of the same molecule were used to determine the molecular fractional abundance at the same position. This occurs for the molecules HC_3N , SO , and C_3H_2 in the FCRAO survey and for NH_3 in the NRAO survey. For HC_3N and NH_3 both transitions give the same results to within acceptable limits due to formal errors in the observations. The more optically thin $\text{SO } N, J=2, 2-1, 1$ transition gives higher abundances than the optically thick $\text{SO } N, J=2, 3-1, 2$ transition. In this case the $\text{SO } N, J=2, 3-1, 2$ intensity is saturated and underestimates the true SO abundance, hence the results for the $\text{SO } N, J=2, 2-1, 1$ transition are more reliable. The opposite is true for the C_3H_2 transitions. The more optically thick $1_{10}-1_{01}$ transition gives a higher abundance than the optically thin $2_{12}-1_{01}$ transition. Possible reasons for this include: (1) miscalibration of the intensities observed with two different antennae; (2) the true excitation temperature is less than 5 K, but would have to be less than the cosmic background in order to reconcile the large difference; or (3) the fractional population of the levels cannot be accurately represented by the LTE approximation and more complicated radiative transfer effects must be considered.

TABLE 6.1a
FCRAO LTE ABUNDANCES AT (0.6,2.9)

molecule	transition	T_{ex}	tau	$N_{\text{U}} (\text{cm}^{-2})$	f_{U}	$N (\text{cm}^{-2})$	$f(X)$
C^{18}O	J=1-0	8.4	0.49	4.6×10^{14}	0.45	1.0×10^{15}	1.7×10^{-7}
CS	J=2-1	5.0	0.51	1.1×10^{12}	0.27	4.0×10^{12}	6.7×10^{-10}
C^{34}S	J=2-1	5.0	0.10	1.9×10^{11}	0.27	6.9×10^{11}	1.2×10^{-10}
H^{13}CO^+	J=1-0	5.0	0.91	5.2×10^{11}	0.47	1.1×10^{12}	1.9×10^{-10}
HC^{18}O^+	J=1-0	5.0	0.08	7.2×10^{10}	0.47	1.5×10^{11}	2.6×10^{-11}
HN^{13}C	J=1-0	5.0	0.52	4.8×10^{11}	0.47	1.0×10^{12}	1.7×10^{-10}
H^{13}CN	J=1-0	5.0	0.13	2.1×10^{11}	0.47	4.4×10^{11}	7.5×10^{-11}
HC_3N	J=5-4	5.0	1.39	1.3×10^{12}	0.13	1.0×10^{13}	1.7×10^{-9}
HC_3N	J=9-8	5.0	0.39	1.1×10^{11}	0.02	6.8×10^{12}	1.2×10^{-9}
C_3H_2	$1_{10}^{-1}0_1$	5.0	>1.	3.1×10^{12}	0.11	2.7×10^{13}	4.6×10^{-9}
C_3H_2	$2_{12}^{-1}0_1$	5.0	1.26	1.4×10^{12}	0.10	1.4×10^{13}	2.4×10^{-9}
N_2H^+	J=1-0	5.0	0.85	1.7×10^{12}	0.47	3.5×10^{12}	5.9×10^{-10}
HCS^+	J=2-1	5.0	0.07	2.1×10^{11}	0.28	7.5×10^{11}	1.3×10^{-10}
OCS	J=7-6	5.0	0.03
SO_2	$3_{13}^{-2}0_2$	5.0	<0.04	$<9.2 \times 10^{10}$	0.06	$<1.6 \times 10^{12}$	$<2.7 \times 10^{-10}$
SO	2,2-1,1	5.0	0.11	3.5×10^{11}	0.01	2.4×10^{13}	4.1×10^{-9}
SO	2,3-1,2	5.0	1.36	1.4×10^{12}	0.15	9.0×10^{12}	1.5×10^{-9}
^{34}SO	2,3-1,2	5.0	0.13	1.8×10^{11}	0.15	1.2×10^{12}	2.0×10^{-10}

TABLE 6.1b

FCRAO LTE ABUNDANCES AT (0.7,0.7)

molecule	transition	T_{ex}	tau	$N_{\text{u}} (\text{cm}^{-2})$	f_{u}	$N (\text{cm}^{-2})$	$f(X)$
C^{18}O	J=1-0	9.1	0.50	5.1×10^{14}	0.44	1.1×10^{15}	1.7×10^{-7}
CS	J=2-1	5.0	0.38	1.2×10^{12}	0.27	4.6×10^{12}	6.7×10^{-10}
C^{34}S	J=2-1	5.0	0.11	2.5×10^{11}	0.27	9.2×10^{11}	1.4×10^{-10}
H^{13}CO^+	J=1-0	5.0	0.73	6.7×10^{11}	0.47	1.4×10^{12}	2.1×10^{-10}
HC^{18}O^+	J=1-0	5.0	0.47
HN^{13}C	J=1-0	5.0	0.38	4.6×10^{11}	0.47	9.8×10^{11}	1.4×10^{-10}
H^{13}CN	J=1-0	5.0	0.08	3.6×10^{11}	0.47	7.7×10^{11}	1.1×10^{-10}
HC_3N	J=5-4	5.0	0.81	7.1×10^{11}	0.13	5.6×10^{12}	8.3×10^{-10}
HC_3N	J=9-8	5.0	0.18	7.4×10^{10}	0.02	4.6×10^{12}	6.8×10^{-10}
C_3H_2	$1_{10}^{-1}0_1$	5.0	4.3	2.4×10^{12}	0.11	2.1×10^{13}	3.1×10^{-9}
C_3H_2	$2_{12}^{-1}0_1$	5.0	0.92	6.2×10^{11}	0.10	6.1×10^{12}	9.0×10^{-10}
N_2H^+	J=1-0	5.0	1.18	2.7×10^{12}	0.47	5.7×10^{12}	8.4×10^{-10}
HCS^+	J=2-1	5.0	0.08	2.4×10^{11}	0.28	8.6×10^{11}	1.3×10^{-10}
OCS	J=7-6	5.0	0.03
SO_2	$3_{13}^{-2}0_2$	5.0	0.24	5.7×10^{11}	0.06	9.7×10^{12}	1.4×10^{-9}
SO	2,2-1,1	5.0	0.44	1.6×10^{12}	0.01	1.1×10^{14}	1.7×10^{-8}
SO	2,3-1,2	5.0	1.22	1.8×10^{12}	0.15	1.2×10^{13}	1.8×10^{-9}
^{34}SO	2,3-1,2	5.0	0.26	4.4×10^{11}	0.15	2.9×10^{12}	4.3×10^{-10}

TABLE 6.1c

FCRAO LTE ABUNDANCES AT (-0.8,0.4)

molecule	transition	T_{ex}	tau	$N_{\text{u}}(\text{cm}^{-2})$	f_{u}	$N(\text{cm}^{-2})$	$f(X)$
C^{18}O	J=1-0	8.9	0.48	6.0×10^{14}	0.44	1.4×10^{15}	1.7×10^{-7}
CS	J=2-1	5.0	0.63	1.8×10^{12}	0.27	6.7×10^{12}	8.5×10^{-10}
C^{34}S	J=2-1	5.0	0.04	7.9×10^{10}	0.27	3.0×10^{11}	3.7×10^{-11}
H^{13}CO^+	J=1-0	5.0	0.40	2.9×10^{11}	0.47	6.3×10^{11}	8.0×10^{-11}
HC^{18}O^+	J=1-0	5.0	0.47
HN^{13}C	J=1-0	5.0	0.17	2.4×10^{11}	0.47	5.1×10^{11}	6.5×10^{-11}
H^{13}CN	J=1-0	5.0	0.06	1.5×10^{11}	0.47	3.2×10^{11}	4.0×10^{-11}
HC_3N	J=5-4	5.0	0.34	5.8×10^{11}	0.13	4.5×10^{12}	5.7×10^{-10}
HC_3N	J=9-8	5.0	<0.03	$<1.6 \times 10^{10}$	0.02	$<9.6 \times 10^{11}$	$<1.2 \times 10^{-10}$
C_3H_2	$1_{10}^{-1}0_1$	5.0	1.4	1.8×10^{12}	0.11	1.6×10^{13}	2.0×10^{-9}
C_3H_2	$2_{12}^{-1}0_1$	5.0	0.55	3.5×10^{11}	0.10	3.5×10^{12}	4.4×10^{-10}
N_2H^+	J=1-0	5.0	0.71	1.8×10^{12}	0.47	3.8×10^{12}	4.8×10^{-10}
HCS^+	J=2-1	5.0	0.10	1.6×10^{11}	0.28	5.8×10^{11}	7.3×10^{-11}
OCS	J=7-6	5.0	0.03
SO_2	$3_{13}^{-2}0_2$	5.0	0.24	1.2×10^{12}	0.06	2.0×10^{13}	2.5×10^{-9}
SO	2,2-1,1	5.0	0.43	1.4×10^{12}	0.01	9.7×10^{13}	1.2×10^{-8}
SO	2,3-1,2	5.0	2.63	3.3×10^{12}	0.15	2.2×10^{13}	2.8×10^{-9}
^{34}SO	2,3-1,2	5.0	0.14	1.5×10^{11}	0.15	1.0×10^{12}	1.3×10^{-10}

TABLE 6.1d

FCRAO LTE ABUNDANCES AT (-1.4,-0.8)

molecule	transition	T_{ex}	tau	$N_{\text{u}} (\text{cm}^{-2})$	f_{u}	$N (\text{cm}^{-2})$	$f(X)$
C^{18}O	J=1-0	8.6	0.61	6.6×10^{14}	0.45	1.5×10^{15}	1.7×10^{-7}
CS	J=2-1	5.0	0.61	1.6×10^{12}	0.27	5.9×10^{12}	6.8×10^{-10}
C^{34}S	J=2-1	5.0	0.09	1.6×10^{11}	0.27	6.0×10^{11}	6.9×10^{-11}
H^{13}CO^+	J=1-0	5.0	0.40	3.6×10^{11}	0.47	7.8×10^{11}	8.5×10^{-11}
HC^{18}O^+	J=1-0	5.0	0.47
HN^{13}C	J=1-0	5.0	0.11	9.6×10^{10}	0.47	2.0×10^{11}	2.3×10^{-11}
H^{13}CN	J=1-0	5.0	0.47
HC_3N	J=5-4	5.0	0.33	5.6×10^{11}	0.13	4.4×10^{12}	5.1×10^{-10}
HC_3N	J=9-8	5.0	0.02
C_3H_2	$1_{10}^{-1}0_1$	5.0	0.68	1.6×10^{12}	0.11	1.4×10^{13}	1.6×10^{-9}
C_3H_2	$2_{12}^{-1}0_1$	5.0	0.30	2.0×10^{11}	0.10	2.0×10^{12}	2.3×10^{-10}
N_2H^+	J=1-0	5.0	0.57	4.1×10^{11}	0.47	8.8×10^{11}	1.0×10^{-10}
HCS^+	J=2-1	5.0	0.08	1.6×10^{11}	0.28	5.7×10^{11}	6.6×10^{-11}
OCS	J=7-6	5.0	0.08	2.0×10^{12}	0.03	6.1×10^{13}	7.1×10^{-9}
SO_2	$3_{13}^{-2}0_2$	5.0	0.49	1.1×10^{12}	0.06	1.9×10^{13}	2.2×10^{-9}
SO	2,2-1,1	5.0	0.61	2.2×10^{12}	0.01	1.6×10^{14}	1.8×10^{-8}
SO	2,3-1,2	5.0	>1.	3.0×10^{12}	0.15	2.0×10^{13}	2.3×10^{-9}
^{34}SO	2,3-1,2	5.0	0.39	6.2×10^{11}	0.15	4.1×10^{12}	4.7×10^{-10}

TABLE 6.1e

FCRAO LTE ABUNDANCES AT (-2.8,0.8)

molecule	transition	T_{ex}	tau	N_u (cm ⁻²)	f_u	N (cm ⁻²)	$f(X)$
C ¹⁸ O	J=1-0	8.9	0.44	5.1×10^{14}	0.44	1.1×10^{15}	1.7×10^{-7}
CS	J=2-1	5.0	0.63	1.3×10^{12}	0.27	5.0×10^{12}	7.4×10^{-10}
C ³⁴ S	J=2-1	5.0	0.10	2.4×10^{11}	0.27	9.0×10^{11}	1.3×10^{-10}
H ¹³ CO ⁺	J=1-0	5.0	0.12	9.5×10^{10}	0.47	2.0×10^{11}	3.0×10^{-11}
HC ¹⁸ O ⁺	J=1-0	5.0	0.47
HN ¹³ C	J=1-0	5.0	<0.04	$<3.0 \times 10^{10}$	0.47	$<6.4 \times 10^{10}$	$<9.5 \times 10^{-12}$
H ¹³ CN	J=1-0	5.0	0.47
HC ₃ N	J=5-4	5.0	0.16	3.8×10^{11}	0.13	3.0×10^{12}	4.4×10^{-10}
HC ₃ N	J=9-8	5.0	0.02
C ₃ H ₂	1 ₁₀ ⁻¹ ₀₁	5.0	<0.53	$<8.8 \times 10^{11}$	0.11	$<7.7 \times 10^{12}$	$<1.1 \times 10^{-9}$
C ₃ H ₂	2 ₁₂ ⁻¹ ₀₁	5.0	0.13	1.9×10^{11}	0.10	1.9×10^{12}	2.8×10^{-10}
N ₂ H ⁺	J=1-0	5.0	0.16	2.7×10^{11}	0.47	5.7×10^{11}	8.4×10^{-11}
HCS ⁺	J=2-1	5.0	0.14	3.6×10^{11}	0.28	1.3×10^{12}	1.9×10^{-10}
OCS	J=7-6	5.0	0.03
SO ₂	3 ₁₃ ⁻² ₀₂	5.0	<0.04	$<1.4 \times 10^{11}$	0.06	$<2.4 \times 10^{12}$	$<3.5 \times 10^{-10}$
SO	2,2-1,1	5.0	0.14	3.0×10^{11}	0.01	2.1×10^{13}	3.2×10^{-9}
SO	2,3-1,2	5.0	1.25	1.9×10^{12}	0.15	1.3×10^{13}	1.9×10^{-9}
³⁴ SO	2,3-1,2	5.0	0.12	2.6×10^{11}	0.15	1.7×10^{12}	2.6×10^{-10}

TABLE 6.1f

FCRAO LTE ABUNDANCES AT (-2.3,2.0)

molecule	transition	T_{ex}	tau	$N_{\text{u}}(\text{cm}^{-2})$	f_{u}	$N(\text{cm}^{-2})$	$f(X)$
C^{18}O	J=1-0	8.5	0.30	5.7×10^{14}	0.45	1.3×10^{15}	1.7×10^{-7}
CS	J=2-1	5.0	0.66	1.8×10^{12}	0.27	6.7×10^{12}	9.0×10^{-10}
C^{34}S	J=2-1	5.0	0.04	5.2×10^{10}	0.27	1.9×10^{11}	2.6×10^{-11}
H^{13}CO^+	J=1-0	5.0	0.47
HC^{18}O^+	J=1-0	5.0	0.47
HN^{13}C	J=1-0	5.0	0.05	3.2×10^{10}	0.47	6.8×10^{10}	9.2×10^{-12}
H^{13}CN	J=1-0	5.0	0.47
HC_3N	J=5-4	5.0	<0.15	$<6.6 \times 10^{10}$	0.13	$<5.2 \times 10^{11}$	$<6.9 \times 10^{-11}$
HC_3N	J=9-8	5.0	0.02
C_3H_2	$1_{10}^{-1}0_1$	5.0	<0.53	8.8×10^{11}	0.11	7.7×10^{12}	1.0×10^{-9}
C_3H_2	$2_{12}^{-1}0_1$	5.0	0.12	9.7×10^{10}	0.10	9.7×10^{11}	1.3×10^{-10}
N_2H^+	J=1-0	5.0	0.14	3.3×10^{11}	0.47	7.0×10^{11}	9.4×10^{-11}
HCS^+	J=2-1	5.0	0.05	1.1×10^{11}	0.28	3.7×10^{11}	5.0×10^{-11}
OCS	J=7-6	5.0	0.03
SO_2	$3_{13}^{-2}0_2$	5.0	<0.19	$<7.6 \times 10^{11}$	0.06	$<1.3 \times 10^{13}$	$<1.7 \times 10^{-9}$
SO	2,2-1,1	5.0	<0.08	$<6.4 \times 10^{11}$	0.01	$<4.5 \times 10^{13}$	$<6.0 \times 10^{-9}$
SO	2,3-1,2	5.0	0.74	1.6×10^{12}	0.15	1.1×10^{13}	1.4×10^{-9}
^{34}SO	2,3-1,2	5.0	0.12	1.2×10^{11}	0.15	8.0×10^{11}	1.1×10^{-10}

TABLE 6.1g

FCRAO LTE ABUNDANCES AT (3.7,-1.2)

molecule	transition	T_{ex}	tau	$N_{\text{u}} (\text{cm}^{-2})$	f_{u}	$N (\text{cm}^{-2})$	$f(X)$
C^{18}O	J=1-0	11.1	0.42	7.5×10^{14}	0.41	1.8×10^{15}	1.7×10^{-7}
CS	J=2-1	5.0	0.59	1.2×10^{12}	0.27	4.5×10^{12}	4.2×10^{-10}
C^{34}S	J=2-1	5.0	0.09	1.3×10^{11}	0.27	4.8×10^{11}	4.4×10^{-11}
H^{13}CO^+	J=1-0	5.0	0.10	9.2×10^{10}	0.47	1.9×10^{11}	1.8×10^{-11}
HC^{18}O^+	J=1-0	5.0	0.47
HN^{13}C	J=1-0	5.0	0.05	4.1×10^{10}	0.47	8.7×10^{10}	8.1×10^{-12}
H^{13}CN	J=1-0	5.0	0.47
HC_3N	J=5-4	5.0	<0.08	$<3.4 \times 10^{10}$	0.13	$<2.7 \times 10^{11}$	$<2.5 \times 10^{-11}$
HC_3N	J=9-8	5.0	0.02
C_3H_2	$1_{10}^{-1}0_1$	5.0	<0.53	$<8.8 \times 10^{11}$	0.11	$<7.7 \times 10^{12}$	$<7.1 \times 10^{-10}$
C_3H_2	$2_{12}^{-1}0_1$	5.0	<0.04	$<1.4 \times 10^{11}$	0.10	$<1.4 \times 10^{12}$	$<1.3 \times 10^{-10}$
N_2H^+	J=1-0	5.0	0.12	2.2×10^{11}	0.47	4.7×10^{11}	4.4×10^{-11}
HCS^+	J=2-1	5.0	0.04	2.3×10^{11}	0.28	8.2×10^{11}	7.5×10^{-11}
OCS	J=7-6	5.0	0.03
SO_2	$3_{13}^{-2}0_2$	5.0	<0.04	$<1.7 \times 10^{11}$	0.06	$<2.9 \times 10^{12}$	$<2.7 \times 10^{-10}$
SO	2,2-1,1	5.0	<0.04	$<8.8 \times 10^{10}$	0.01	$<6.2 \times 10^{12}$	$<5.7 \times 10^{-10}$
SO	2,3-1,2	5.0	1.00	1.3×10^{12}	0.15	8.4×10^{12}	7.8×10^{-10}
^{34}SO	2,3-1,2	5.0	0.09	2.2×10^{11}	0.15	1.5×10^{12}	1.4×10^{-10}

TABLE 6.2
NRAO LTE ABUNDANCES

position	transition	T_{ex} (K)	tau	N_u^a (cm^{-2})	f_u	N_{tot} (cm^{-2})	$f(X)$
(0,0)	C^{18}O J=1-0	8.2	0.57	5.8×10^{14}	0.45	1.3×10^{15}	1.7×10^{-7}
	NH_3 (1,1)	5.0	>1.	1.5×10^{14}	0.24	6.4×10^{14}	8.4×10^{-8}
	NH_3 (2,2)	5.0	0.27	6.2×10^{12}	0.010	6.1×10^{14}	8.1×10^{-8}
	C_3H_2 $1_{10}^{-1}0_1$	5.0	3.5	2.2×10^{12}	0.11	1.9×10^{13}	2.6×10^{-9}
	HC_3N J=2-1	5.0	0.10	5.6×10^{11}	0.17	3.4×10^{12}	4.5×10^{-10}
	C_4H N=2-1	5.0	<0.06	$<9.5 \times 10^{12}$	0.17	$<5.6 \times 10^{13}$	$<7.4 \times 10^{-9}$
(-2,-1)	C^{18}O J=1-0	8.7	0.62	7.5×10^{14}	0.45	1.7×10^{15}	1.7×10^{-7}
	NH_3 (1,1)	5.0	0.79	5.5×10^{13}	0.24	2.3×10^{14}	2.3×10^{-8}
	NH_3 (2,2)	5.0	<0.05	$<3.0 \times 10^{12}$	0.01	$<2.9 \times 10^{14}$	$<2.9 \times 10^{-8}$
	C_3H_2 $1_{10}^{-1}0_1$	5.0	0.65	1.3×10^{12}	0.11	1.1×10^{13}	1.1×10^{-9}
	HC_3N J=2-1	5.0	0.04	$<1.8 \times 10^{11}$	0.17	$<1.1 \times 10^{12}$	$<1.1 \times 10^{-10}$
	C_4H N=2-1	5.0	0.07	1.7×10^{13}	0.17	1.0×10^{14}	1.0×10^{-8}
(-3,1)	C^{18}O J=1-0	8.3	0.71	8.8×10^{14}	0.45	1.9×10^{15}	1.7×10^{-7}
	NH_3 (1,1)	5.0	0.54	4.4×10^{13}	0.24	1.8×10^{14}	1.6×10^{-8}
	NH_3 (2,2)	5.0	<0.05	$<3.1 \times 10^{12}$	0.010	$<3.0 \times 10^{14}$	$<2.6 \times 10^{-8}$
	C_3H_2 $1_{10}^{-1}0_1$	5.0	0.39	5.1×10^{11}	0.11	4.5×10^{12}	3.9×10^{-10}
	HC_3N J=2-1	5.0	0.08	4.9×10^{11}	0.17	3.0×10^{12}	2.6×10^{-10}
	C_4H N=2-1	5.0	0.09	2.8×10^{13}	0.17	1.6×10^{14}	1.4×10^{-8}

(4,-1)	C ¹⁸ O	J=1-0	11.3	0.49	8.6x10 ¹⁴	0.41	2.1x10 ¹⁵	1.7x10 ⁻⁷
	NH ₃	(1,1)	5.0	0.30	1.5x10 ¹³	0.24	6.4x10 ¹³	5.1x10 ⁻⁹
	NH ₃	(2,2)	5.0	<0.05	<3.2x10 ¹²	0.010	<3.1x10 ¹⁴	<2.5x10 ⁻⁸
	C ₃ H ₂	¹ ₁₀ - ¹ ₀₁	5.0	0.35	6.2x10 ¹¹	0.11	5.4x10 ¹²	4.4x10 ⁻¹⁰
	HC ₃ N	J=2-1	5.0	0.04	<1.7x10 ¹¹	0.17	<1.0x10 ¹²	<8.1x10 ⁻¹¹
	C ₄ H	N=2-1	5.0	<0.03	<1.0x10 ¹³	0.17	<5.9x10 ¹³	<4.7x10 ⁻⁹
(0,2)	C ¹⁸ O	J=1-0	9.3	0.47	6.8x10 ¹⁴	0.44	1.6x10 ¹⁵	1.7x10 ⁻⁷
	NH ₃	(1,1)	5.0	>1.	1.2x10 ¹⁴	0.24	4.9x10 ¹⁴	5.3x10 ⁻⁸
	NH ₃	(2,2)	5.0	0.17	5.1x10 ¹²	0.010	5.0x10 ¹⁴	5.4x10 ⁻⁸
	C ₃ H ₂	¹ ₁₀ - ¹ ₀₁	5.0	>1.	2.6x10 ¹²	0.11	2.3x10 ¹³	2.5x10 ⁻⁹
	HC ₃ N	J=2-1	5.0	0.51	1.1x10 ¹²	0.17	6.9x10 ¹²	7.5x10 ⁻¹⁰
	C ₄ H	N=2-1	5.0	0.12	1.8x10 ¹³	0.17	1.1x10 ¹⁴	1.1x10 ⁻⁸
(1,1)	C ¹⁸ O	J=1-0	8.7	0.65	4.9x10 ¹⁴	0.45	1.1x10 ¹⁵	1.7x10 ⁻⁷
	NH ₃	(1,1)	5.0	1.3	7.4x10 ¹³	0.24	3.0x10 ¹⁴	4.7x10 ⁻⁸
	NH ₃	(2,2)	5.0	<0.04	<2.7x10 ¹²	0.010	<2.6x10 ¹⁴	<4.1x10 ⁻⁸
	C ₃ H ₂	¹ ₁₀ - ¹ ₀₁	5.0	>1.	2.5x10 ¹²	0.11	2.2x10 ¹³	3.4x10 ⁻⁹
	HC ₃ N	J=2-1	5.0	0.33	1.2x10 ¹²	0.17	7.9x10 ¹²	1.1x10 ⁻⁹
	C ₄ H	N=2-1	5.0	<0.03	<1.1x10 ¹³	0.17	<6.2x10 ¹³	<9.6x10 ⁻⁹

(1,3)	C ¹⁸ O	J=1-0	8.5	0.45	3.1x10 ¹⁴	0.45	6.8x10 ¹⁴	1.7x10 ⁻⁷
	NH ₃	(1,1)	5.0	>1.	1.2x10 ¹⁴	0.24	4.8x10 ¹⁴	1.2x10 ⁻⁷
	NH ₃	(2,2)	5.0	0.13	5.1x10 ¹²	0.010	5.0x10 ¹⁴	1.3x10 ⁻⁷
	C ₃ H ₂	1 ₁₀ ⁻¹ ₀₁	5.0	>1.	3.4x10 ¹²	0.11	3.0x10 ¹³	7.4x10 ⁻⁹
	HC ₃ N	J=2-1	5.0	0.53	1.5x10 ¹²	0.17	8.8x10 ¹²	2.2x10 ⁻⁹
	C ₄ H	N=2-1	5.0	0.14	1.7x10 ¹³	0.17	1.0x10 ¹⁴	2.5x10 ⁻⁸
(0.6,3.3)	C ¹⁸ O	J=1-0 ^b	8.4	0.49	4.6x10 ¹⁴	0.45	1.0x10 ¹⁵	1.7x10 ⁻⁷
	HC ₃ N	J=2-1	5.0	0.55	2.1x10 ¹²	0.17	1.2x10 ¹³	2.1x10 ⁻⁹

notes to Table 6.2:

^a total column density of (J,K) level for NH₃ transitions

^b based on C¹⁸O J=1-0 position (0.6,2.9) from FCRAO survey

b) correlation analysis

The maps of Figure 4.2 show the different distributions on the plane of the sky for the molecular transitions mapped. As a means of quantifying these differences, linear correlation coefficients were determined between the map spectra. For example, a plot of the integrated intensity of the individual points of one map vs. the integrated intensity of the individual points of a second map would reveal a straight line of slope 1 if the two maps were perfectly correlated and would be scattered with a slope of 0 if the two maps showed no correlation. Correlation coefficients lie between -1 and 1, where 1 represents a perfect correlation, 0 represents no correlation at all, and -1 represents a perfect anti-correlation.

Table 6.3 lists the results of linearly correlating the integrated intensities of the spectra from the six maps. Listed in Table 6.3 are the two maps correlated; the number of mapped points common between the two maps, N; and the linear correlation coefficient, R. A high degree of correlation is seen to exist between the integrated intensities of the NH_3 and C_3H_2 maps. The H^{13}CO^+ and SO maps are moderately correlated with all the other maps, while the C^{18}O and CS maps are not highly correlated with any of the other maps. The high degree of correlation between H^{13}CO^+ and C_3H_2 results from only correlating the region over which C_3H_2 was mapped. Outside this region the H^{13}CO^+ map extends into the region of peak SO emission and does not correlate well

with NH_3 at these positions, hence the $\text{NH}_3 - \text{H}^{13}\text{CO}^+$ correlation is lower than the $\text{NH}_3 - \text{C}_3\text{H}_2$ and $\text{H}^{13}\text{CO}^+ - \text{C}_3\text{H}_2$ correlation coefficients.

These differences are further exemplified by the spectral line survey data presented in Figures 4.5 through 4.28. The integrated intensity correlations for the observed transitions in the FCRAO and NRAO surveys are in Tables 6.4 and 6.5, respectively. Since in the optically thin approximation the constant of proportionality between the molecular abundance and the integrated intensity is the same at each position for a specific transition, the correlation coefficients between integrated intensities are the same as those between abundances. Listed in both these tables are the transitions correlated; the number of points correlated, N ; the correlation coefficient, R ; and the probability that an uncorrelated random distribution would produce a correlation coefficient equal to or greater than the one obtained, P_c (Bevington 1969). This probability provides a means of evaluating the significance of a correlation with a low number of data points. The lower the probability, P_c , the more significant the correlation.

As seen in the C^{18}O $J=1-0$ map and verified with the C^{18}O $J=1-0$ survey data, emission from this transition peaks in the southeast region of the core at survey position (3.7, -1.2) and is weak at the (0.6, 2.9) position of the dense condensation found from the NH_3 spectra. In addition, emission from this transition is noticeably

uniform across the entire core region and does not correlate well any other transition.

Similarly, the CS J=2-1 emission is weak at the (0.6,2.9) position and strong at the (3.7,-1.2) position. Emission from both $C^{34}S$ and HCS^+ is weak, but also seems relatively uniform at the seven surveyed positions. This uniformity is consistent with the CS data, despite the fact that the CS J=2-1 transition is shown to be optically thick with optical depths between 1 and 10 at the survey positions (Table 5.2). Since there is no evidence for isotopic fractionation in sulfur and a main formation mechanism of CS is through recombination reactions with HCS^+ in the dense core, the well correlated $C^{34}S$ and HCS^+ transitions are tracing the optically thin CS distribution. The CS transition is not correlated with the $C^{34}S$ and HCS^+ transitions, as shown in Figure 6.1, because of the effects of high optical depth and self-absorption.

A group of molecules have their emission peak at the (0.6,2.9) position and are also strong at the (0.7,0.7) position, while becoming weaker elsewhere. This group is made up of the molecules $H^{13}CO^+$, $HN^{13}C$, $H^{13}CN$, HC_3N , C_3H_2 , and C_4H . Emission from N_2H^+ clearly peaks at the (0.7,0.7) position, as does the $H^{13}CO^+$ integrated intensity, although the survey $H^{13}CO^+$ maximum intensity and the map $H^{13}CO^+$ intensity peak at (0.6,2.9). Additionally, the $H^{13}CN$ J=1-0, F=2-1 line peaks at (0.6,2.9), but the F=1-1 line is stronger at (0.7,0.7) which results in the total $H^{13}CN$ J=1-0 integrated intensity being stronger at (0.7,0.7) (see Figure 4.12). NH_3 observed at NRAO peaks at (0,0),

while the NH_3 map indicates that the peak in the NH_3 emission is slightly greater at the (0.6,2.9) position. It is not surprising that the two NH_3 transitions are very highly correlated. Also C_3H_2 correlates well with NH_3 and HC_3N . The only clear detection of C_4H is the N=2-1, F=3-2 transition at the (1,3) position. All these transitions seem to have very similar distributions to within the errors of the measurements and their emissions are well correlated as exemplified in Figure 6.2.

Another group of molecules have their peak emission at the (-1.4,-0.8) position, which is coincident with the peak in the SO map, and are weak at the (0.6,2.9) position. These molecules include both observed transitions of SO, ^{34}SO , and SO_2 . This distribution is also evident in the SO_2 data of Irvine, Good, and Schloerb (1983). These molecules are correlated with themselves, as seen in Figure 6.3, but not with the other transitions observed.

To summarize, there are three main groups of optically thin species; basically hydrocarbon molecules which peak at (0.6,2.9) and are strong at (0.7,0.7); SO related molecules which peak at (-1.4,0.8) and are weak or not detected at (0.6,2.9); and the C^{34}S and HCS^+ which peak at the (0.7,0.7) position, but are clearly not peaked at (0.6,2.9). The hydrocarbon group includes the N_2H^+ ion and NH_3 which may peak toward (0,0) or (0.7,0.7), but are nearly as strong at (0.6,2.9). Because of the low density required to excite C^{18}O J=1-0, it is sampling a lower density envelope surrounding the high density

core and the CS J=2-1 map is distorted by radiative transfer effects, hence these two transitions are excluded from the grouping. High optical depths do not necessarily alter the distribution of a particular species, as evidenced by the SO group, but self-absorption effects of CS spectra may be reflected in the lack of correlation between CS and C³⁴S.

TABLE 6.3

L134N MAPPED INTEGRATED INTENSITY CORRELATIONS

moiecular maps	N	R
-----	---	-----
$C^{18}O$: CS	161	0.460
$H^{13}CO^+$	137	0.219
SO	155	0.483
NH_3	116	0.236
C_3H_2	30	-0.026
CS : $H^{13}CO^+$	144	0.218
SO	158	0.489
NH_3	120	0.271
C_3H_2	30	0.160
$H^{13}CO^+$: SO	144	0.466
NH_3	129	0.496
C_3H_2	34	0.731
SO : NH_3	127	0.406
C_3H_2	29	0.416
NH_3 : C_3H_2	34	0.823

TABLE 6.4

FCRAO SURVEY CORRELATIONS

transitions		N	R	Pc
C ¹⁸ O J=1-0 :	CS J=2-1	7	0.285	0.536
	C ³⁴ S J=2-1	7	-0.467	0.291
	HCS ⁺ J=2-1	7	0.233	0.615
	H ¹³ CO ⁺ J=1-0	6	-0.457	0.362
	H ¹³ CN J=1-0	3	-0.809	0.400
	HN ¹³ C J=1-0	7	-0.488	0.267
	HC ₃ N J=5-4	7	-0.511	0.241
	HC ₃ N J=9-8	3	-0.931	0.238
	C ₃ H ₂ 2 ₁₂ -1 ₀₁	7	-0.507	0.246
	N ₂ H ⁺ J=1-0	7	-0.427	0.339
	SO 2,3-1,2	7	-0.026	0.956
	SO 2,2-1,1	7	0.210	0.651
	³⁴ SO 2,3-1,2	7	0.084	0.858
	SO ₂ 3 ₁₃ -2 ₀₂	7	0.013	0.978
	CS J=2-1 :	C ³⁴ S J=2-1	7	-0.738
HCS ⁺ J=2-1		7	-0.248	0.592
H ¹³ CO ⁺ J=1-0		6	-0.131	0.805
H ¹³ CN J=1-0		3	-0.625	0.570
HN ¹³ C J=1-0		7	-0.563	0.188
HC ₃ N J=5-4		7	-0.409	0.362
HC ₃ N J=9-8		3	-0.994	0.070
C ₃ H ₂ 2 ₁₂ -1 ₀₁		7	-0.293	0.524
N ₂ H ⁺ J=1-0		7	-0.291	0.527
SO 2,3-1,2		7	0.512	0.240
SO 2,2-1,1		7	0.186	0.690
³⁴ SO 2,3-1,2		7	-0.232	0.617
SO ₂ 3 ₁₃ -2 ₀₂		7	-0.024	0.959

$C^{34}S$ J=2-1 :	HCS^+ J=2-1	7	0.803	0.030	
	$H^{13}CO^+$ J=1-0	6	-0.048	0.928	
	$H^{13}CN$ J=1-0	3	0.770	0.441	
	$HN^{13}C$ J=1-0	7	0.104	0.824	
	HC_3N J=5-4	7	0.140	0.765	
	HC_3N J=9-8	3	0.952	0.198	
	C_3H_2 $2_{12}^{-1}0_1$	7	0.094	0.841	
	N_2H^+ J=1-0	7	-0.169	0.717	
	SO 2,3-1,2	7	-0.470	0.287	
	SO 2,2-1,1	7	-0.173	0.711	
	^{34}SO 2,3-1,2	7	0.578	0.174	
	SO_2 $3_{13}^{-2}0_2$	7	-0.098	0.834	
	HCS^+ J=2-1 :	$H^{13}CO^+$ J=1-0	6	0.674	0.142
		$H^{13}CN$ J=1-0	3	0.918	0.260
$HN^{13}C$ J=1-0		7	0.675	0.096	
HC_3N J=5-4		7	0.219	0.637	
HC_3N J=9-8		3	0.159	0.898	
C_3H_2 $2_{12}^{-1}0_1$		7	0.666	0.102	
N_2H^+ J=1-0		7	0.711	0.073	
SO 2,3-1,2		7	-0.058	0.902	
SO 2,2-1,1		7	0.353	0.437	
^{34}SO 2,3-1,2		7	0.020	0.966	
SO_2 $3_{13}^{-2}0_2$		7	0.197	0.672	
$H^{13}CO^+$ J=1-0 :	$H^{13}CN$ J=1-0	3	0.961	0.178	
	$HN^{13}C$ J=1-0	6	0.819	0.046	
	HC_3N J=5-4	6	0.576	0.232	
	HC_3N J=9-8	3	0.282	0.818	
	C_3H_2 $2_{12}^{-1}0_1$	6	0.962	0.002	
	N_2H^+ J=1-0	6	0.877	0.022	
	SO 2,3-1,2	6	0.166	0.753	
	SO 2,2-1,1	6	0.397	0.436	

	^{34}SO	2,3-1,2	6	0.108	0.839
	SO_2	$3_{13}^{-2}0_2$	6	0.281	0.590
H^{13}CN J=1-0	:	HN^{13}C J=1-0	3	0.791	0.419
		HC_3N J=5-4	3	-0.355	0.769
		HC_3N J=9-8	3	0.538	0.638
		C_3H_2 $2_{12}^{-1}0_1$	3	0.987	0.103
		N_2H^+ J=1-0	3	0.904	0.281
		SO 2,3-1,2	3	-0.760	0.450
		SO 2,2-1,1	3	0.056	0.964
		^{34}SO 2,3-1,2	3	0.999	0.028
		SO_2 $3_{13}^{-2}0_2$	3	-0.708	0.499
HN^{13}C J=1-0	:	HC_3N J=5-4	7	0.695	0.083
		HC_3N J=9-8	3	0.941	0.220
		C_3H_2 $2_{12}^{-1}0_1$	7	0.813	0.026
		N_2H^+ J=1-0	7	0.913	0.004
		SO 2,3-1,2	7	-0.015	0.975
		SO 2,2-1,1	7	0.112	0.811
		^{34}SO 2,3-1,2	7	-0.136	0.771
		SO_2 $3_{13}^{-2}0_2$	7	0.230	0.620
HC_3N J=5-4	:	HC_3N J=9-8	3	0.598	0.592
		C_3H_2 $2_{12}^{-1}0_1$	7	0.362	0.425
		N_2H^+ J=1-0	7	0.659	0.107
		SO 2,3-1,2	7	0.528	0.223
		SO 2,2-1,1	7	0.447	0.315
		^{34}SO 2,3-1,2	7	0.053	0.910
		SO_2 $3_{13}^{-2}0_2$	7	0.750	0.052
HC_3N J=9-8	:	C_3H_2 $2_{12}^{-1}0_1$	3	0.397	0.740
		N_2H^+ J=1-0	3	0.129	0.918
		SO 2,3-1,2	3	-0.957	0.187
		SO 2,2-1,1	3	-0.811	0.398

	^{34}SO 2,3-1,2	3	0.497	0.669
	SO_2 $3_{13}^{-2}0_2$	3	-0.976	0.140
C_3H_2 $2_{12}^{-1}0_1$:	N_2H^+ J=1-0	7	0.841	0.018
	SO 2,3-1,2	7	-0.067	0.887
	SO 2,2-1,1	7	0.164	0.725
	^{34}SO 2,3-1,2	7	0.047	0.920
	SO_2 $3_{13}^{-2}0_2$	7	0.040	0.932
N_2H^+ J=1-0 :	SO 2,3-1,2	7	0.210	0.651
	SO 2,2-1,1	7	0.240	0.604
	^{34}SO 2,3-1,2	7	-0.238	0.607
	SO_2 $3_{13}^{-2}0_2$	7	0.332	0.467
SO 2,3-1,2 :	SO 2,2-1,1	7	0.732	0.061
	^{34}SO 2,3-1,2	7	0.046	0.922
	SO_2 $3_{13}^{-2}0_2$	7	0.807	0.028
SO 2,2-1,1 :	^{34}SO 2,3-1,2	7	0.588	0.165
	SO_2 $3_{13}^{-2}0_2$	7	0.864	0.012
^{34}SO 2,3-1,2 :	SO_2 $3_{13}^{-2}0_2$	7	0.369	0.415

TABLE 6.5

NRAO SURVEY CORRELATIONS

transitions	N	R	P _c
C_3H_2 $1_{10}^{-1}0_1$: HC_3N J=2-1	7	0.695	0.083
NH_3 (1,1)	7	0.839	0.018
NH_3 (2,2)	7	0.526	0.225
C_4H N=2-1	7	0.428	0.338
HC_3N J=2-1 : NH_3 (1,1)	7	0.387	0.391
NH_3 (2,2)	7	0.254	0.583
C_4H N=2-1	7	0.517	0.235
NH_3 (1,1) : NH_3 (2,2)	7	0.586	0.167
C_4H N=2-1	7	0.267	0.563
NH_3 (2,2) : C_4H N=2-1	7	0.881	0.009

Figure 6.1 Observed Integrated Intensities of CS J=2-1 and HCS⁺ J=2-1 plotted as a function of the observed integrated intensity of C³⁴S J=2-1. A linear fit of HCS⁺ to C³⁴S shows a positive slope indicating that emission from these two transitions is correlated. On the other hand, a linear fit of CS and C³⁴S indicate an anti-correlation due to self-absorption and possible optical depth effects for CS J=2-1. Units of Integrated Intensity are K km s⁻¹.

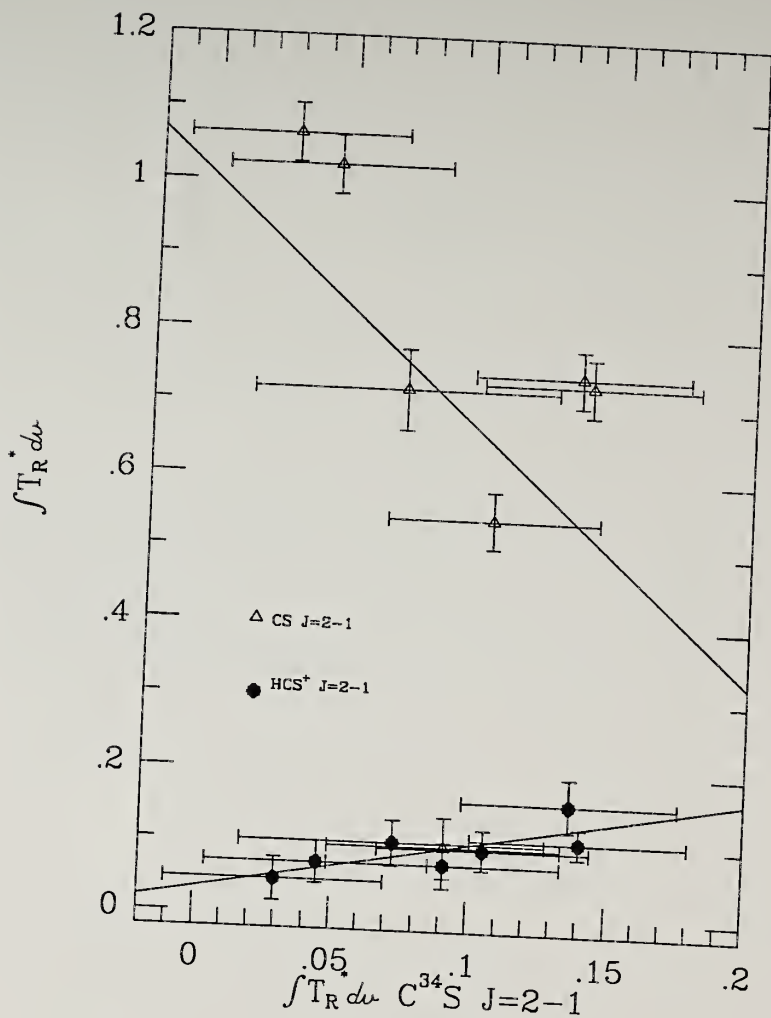


Figure 6.2 Observed integrated intensities of HC_3N $J=5-4$, C_3H_2 $2_{12}-1_{01}$, and H^{13}CN $J=1-0$ plotted as a function of the observed integrated intensity of HN^{13}C . Linear fits indicated a positive slope for all three transitions indicating that they are correlated with HN^{13}C . Units of integrated intensity are K km s^{-1} .

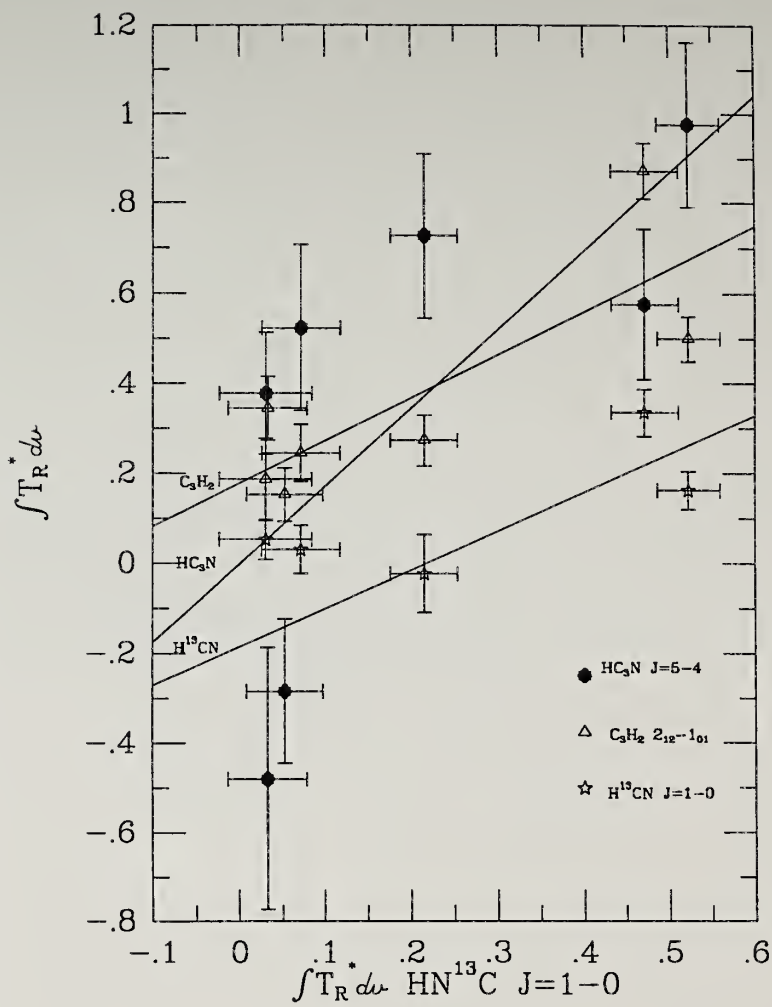
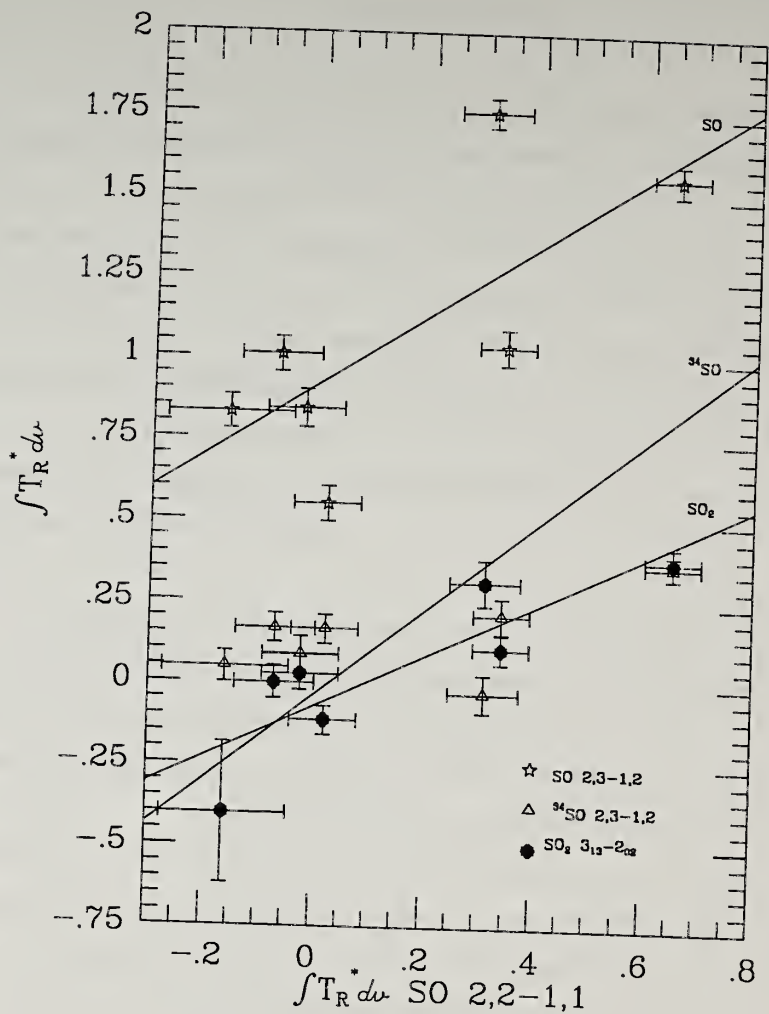


Figure 6.3 Observed Integrated Intensities of SO 2,3-1,2, ^{34}SO 2,3-1,2, and SO_2 3₁₃-2₀₂ plotted as a function of the observed Integrated Intensity of SO 2,2-1,1. Linear fits indicated a positive slope for all three transitions indicating that they are correlated with SO 2,2-1,1. Units of Integrated Intensity are K km s^{-1} .



c) Chemical Models

The observed distributions of molecular species must depend on the chemical reactions which produce the observed molecular abundance, as well as the physical conditions which lead to excitation of the observed transitions. These chemical reactions can affect the molecular distribution since: (1) the abundance of molecules depends upon the abundance of their constituent atoms in the gas phase and there may be elemental abundance gradients within the cloud core gas or (2) physical conditions within a certain core region may not be conducive to production of an intermediate species in the reaction pathway of a specific molecule.

A number of difficulties arise in trying to compare observations of a specific cloud to a general chemical model. (1) The chemistry particular to a cloud depends on the cloud's age and initial conditions, particularly the initial elemental abundances. (2) The abundance of different species varies at different cloud densities, and since density will vary along the line of sight through the cloud, observed abundances are both beam averaged and averaged through the cloud along the line of sight. That is, the assumption that the ratio of column densities represents the true molecular abundance ratio within the core may be in error. (3) Reaction rates used in chemical models and measured in a laboratory may be very uncertain under the conditions of the temperatures and densities common in molecular clouds.

Despite these sources of error, the chemistry of individual molecules or related groups of molecules are discussed below. Observed abundances are compared to predictions made from the reaction schemes used in chemical models. In general, these models consider only steady state chemistry. Models which allow for a time dependent chemistry, but not a physical evolution, find steady state is reached in about 10^7 years (e.g., Leung, Herbst, Huebner 1984). From consideration of free-fall collapse times in Chapter II a lower limit to the age of L134N was set at about 10^6 years, so the possibility exists that a chemical steady state has not yet been reached.

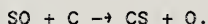
1) CO

Carbon and oxygen are readily available elements that easily form CO through many different reaction pathways even at low densities (Oppenheimer and Daigarno 1975). Destruction of CO occurs mainly by reactions with ionized helium (Prasad and Huntress 1980b) to form C^+ , which either directly recycles back to CO or goes into production of hydrocarbons of which only a small fraction do not recycle back to CO. Almost all other reactions which contribute to its destruction recycle back to CO, hence CO is difficult to remove once it is formed. A high CO abundance combined with the fact that CO $J=1-0$ excitation occurs at low densities makes even the rare $C^{18}O$ isotope a poor probe of core chemistry.

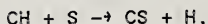
11) sulfur chemistry

Once either all of the carbon or all of the oxygen has gone into the formation of CO, depending on the gas phase C/O ratio, the remaining C or O forms a reservoir for formation of other molecules (Graedel, Langer, and Frerking 1982; Watt 1983). If there is ample sulfur in the gas phase, it is possible to form CS in a region with excess C or SO in a region with excess O. Models of cloud chemistry use single point homogenous clouds and solve chemical reaction networks for clouds with different physical conditions and initial elemental abundances. However, if an elemental abundance difference, such as a C/O gradient, exists in the gas phase within a single cloud, the chemistry may vary within this cloud. Such a C/O gradient in L134N may explain the different morphology observed in the CS and SO maps and survey data of this cloud.

The basic CS production scheme given by Prasad and Huntress (1982) includes a very slow reaction for conversion of SO to CS by



Observations in L134N indicate SO and CS do not coexist over most of the core region. Conversion of SO into CS in a region of high C abundance may be at least partially responsible for the absence of SO in the high density core. Also suggested is the reaction



which may produce CS in lower density regions where CH is abundant. In the high density core region the ion-molecule reaction

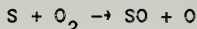


is the principle CS formation mechanism. This is demonstrated by a high correlation between emission from the optically thin species C^{34}S and HCS^+ . CS may be destroyed by charge transfer reactions with atomic and molecular ions producing CS^+ and HCS^+ which recycle back to CS (see for example Graedel, Langer, and Frerking 1982; Watt and Charnley 1985). Hence, CS is a sink for carbon and sulfur atoms. The chemical models of Prasad and Huntress also indicate that as the oxygen abundance is decreased, S goes into CS instead of SO.

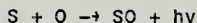
The ease with which CS is produced and the fact that it is difficult to destroy may provide the answer as to why the distribution of CS emission is so extended despite a high value of n^* for the CS $J=2-1$ transition. Since CS is a sink for carbon and sulfur atoms, in an oxygen depleted region all the sulfur will eventually be processed into CS (Watt and Charnley 1985). This leads to a high CS column density for a cloud evolved enough for a significant amount of CS to have formed. Therefore, a high CS abundance is produced, even in the low density regions, which masks CS emission from the high density core. Self-absorption of CS $J=2-1$ spectra provides evidence for CS production at low densities.

SO and SO_2 can only be formed by neutral-neutral reactions with rate coefficients about $10^{-10} - 10^{-12} \text{ cm}^3 \text{ s}^{-1}$, hence SO formation occurs more slowly than other molecules which arise from ion-molecule reactions with rate coefficients on the order of $10^{-9} \text{ cm}^3 \text{ s}^{-1}$.

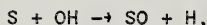
Therefore, SO and SO₂ form in later stages of a cloud's chemical evolution (Watt and Charnley 1985). SO is formed principally through the reactions



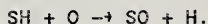
and



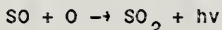
which may be important at 10 K (Millar 1982; Prasad and Huntress 1982). These reactions require regions of high O abundance in order to proceed. Other minor reaction which can contribute to SO production include



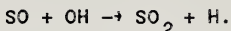
which may produce SO in low density regions where OH is abundant, and



In regions of high oxygen abundance, SO proceeds quickly into SO₂ by



and



Other means of destroying SO involve reactions with ions or carbon, both of which have low abundance in the region of the SO map. SO₂ is only destroyed by reactions with ions which convert SO₂ back into SO, only to be recycled back to SO₂. Hence, SO₂ is a sink for S and O atoms and SO₂ abundance should increase with cloud age.

In principle, a cloud in steady-state chemistry would have converted all of the SO into SO₂. In the molecular clouds W3(OH) and DR21(OH) the SO₂ abundance is greater than the SO abundance indicating

that they are older clouds (Prasad and Huntress 1982), but in L134N the SO abundance is observed to be greater than the SO₂ abundance. Either L134N is not at an advanced stage of chemical evolution or the ion abundance in L134N is high enough to reprocess a significant amount of SO₂ back into SO.

Comparison of these reactions for SO with those for CS production indicate that in a cloud with a reservoir of S, CS will form in a region with excess carbon and SO will form in a region of excess oxygen. The dichotomy of the CS and SO mapped distributions indicate that a C/O gradient exists across the core region of L134N with a high C/O in the dense region where the hydrocarbons, cyanopolyynes, and ammonia peak and a low C/O in the region where SO and SO₂ emission peaks. This C/O gradient may be caused by a change in the absolute gas phase abundance of either C or O, or may be the result of a simultaneous change in the abundance of both.

Based on the chemical models of Watt (1983, 1985), Watt *et al.* (1986) proposed that SO is converted into CS and SO₂ by the reactions indicated above. Hence, the abundance ratio SO/SO₂ is indicative of the C/O abundance ratio. In regions of higher C abundance the SO/SO₂ ratio is high, while in regions of high O abundance the SO/SO₂ ratio is low. Table 6.6 lists the observed SO/SO₂ ratio at the seven survey positions along with the derived C/O abundance ratio from Watt *et al.* (1986). In general, this trend seems to hold, although upper limits for four of the seven SO₂ spectra only provide lower limits for the

SO/SO₂ ratio at these positions. The derived C/O ratio is higher in the dense core region where the oxygen abundance is believed to be low, however the range in values of C/O is not large. One result of this model is that even in the high O region, the C/O ratio is still greater than one.

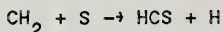
In addition, from the model of Prasad and Huntress (1982), the SO/CS abundance ratio can be used to predict the fractional abundance of atomic oxygen. The observed column densities of optically thin C³⁴S and ³⁴SO are used to determine the SO/CS ratio and the value of the O abundance as a function of the SO/CS abundance ratio is derived from Tables 1 and 2 of Prasad and Huntress. By taking the SO/CS abundance ratio, the O abundance becomes independent of the total sulfur abundance in the model. Interpolation between the listed SO/CS abundance ratio allows a determination of the fractional abundance of oxygen. The results are presented in Table 6.6. The oxygen abundance peaks at the (-1.4,-0.8) position where SO peaks and falls off away from this position. Oxygen is depleted at the (0.6,2.9) position by a factor of 5 from the (-1.4,-0.8) position.

Combining the C/O ratio results from Watt et al. with the O abundance determination from Prasad and Huntress results in a carbon abundance that is relatively constant across the core with a fractional abundance of approximately 2×10^{-6} as indicated in Table 6.6. This value is consistent with the observation of Phillips and Huggins (1981), who determined an atomic carbon column density of $> 2.9 \times 10^{16}$

cm^{-2} at the (0,0) position in L134N. This translates to a fractional abundance of C1, $f(\text{C1}) > 5 \times 10^{-6}$, slightly greater than, but consistent with the C1 abundance determined above. Time-dependent models of cloud chemistry (e.g., Leung, Herbst, and Huebner 1984) find this carbon abundance too high for a steady-state chemistry, but typical of a cloud of age $10^5 - 10^6$ years.

III) OCS

The exact formation mechanism of OCS is unknown, and possible chemical schemes for OCS formation are reviewed by Matthews *et al.* (1987). A principle OCS formation mechanism is through the reactions



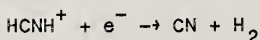
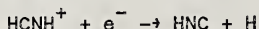
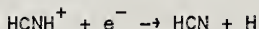
(Graedel, Langer, and Frerking 1982). If OCS requires a high oxygen abundance to form, the (-1.4,-0.8) position should have the highest OCS abundance. However, if the above production scheme is the major source of OCS, regions of high CH_2 , hence hydrocarbon, abundance would have the greatest OCS abundance. Due to the low intensity of the OCS J=7-6 emission line, OCS was only searched for at this position.

Observations at other positions, particularly the (0.6,2.9) position, are needed in order to determine the OCS distribution and provide clues to its chemical formation mechanism.

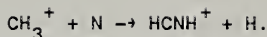
lv) H^{13}CN and HN^{13}C

To date, chemical models of cloud chemistry have not differentiated between molecular isomers, hence they have treated HCN and HNC as one species (e.g., Millar and Freeman 1984a). However, the HNC/HCN abundance ratio in molecular clouds has been reported to vary from values much less than one in giant molecular clouds (Goldsmith *et al.* 1981) to values greater than one in dark clouds (see Irvine *et al.* 1985 for discussion). Irvine and Schloerb (1984) find a HNC/HCN abundance ratio of 1.55 ± 0.16 (3 σ) for the dark cloud TMC 1 using the optically thin ^{13}C and ^{15}N isotopically substituted forms of HNC and HCN. Observations of HN^{13}C and H^{13}CN at three positions in L134N from this study also indicate values of the HNC/HCN ratio greater than one despite large formal errors. These values are 2.5 ± 1.1 at (0.6,2.9), 1.3 ± 0.6 at (0.7,0.7), and 1.7 ± 2.9 at (-0.8,0.4).

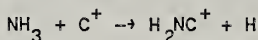
Herbst (1978) suggested that HCN, HNC, and CN form from the ion HCNH^+ by the electron recombination reactions



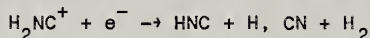
with a value for the branching ratio of the first two reactions such that $\text{HCN}/\text{HNC} = 1.1$ ($\text{HNC}/\text{HCN}=0.9$). This predicts a slight preferential formation of HCN which is not observed in cold dark clouds TMC-1 and L134N. A possible explanation may lie in the formation of the precursor ion HCNH^+ . Herbst proposes its formation by the reaction



However, Allen, Goddard, and Schaefer (1980) proposed that the reaction



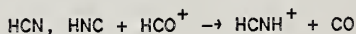
is also active in cold clouds, and that the recombination reaction



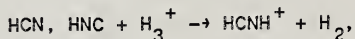
produces HNC, but the structure of H_2NC^+ will not allow for the formation of HCN. Since the branching ratio for this reaction is not known, the amount of HNC formed from this pathway is uncertain. Assuming HCN and HNC are destroyed at the same rate, this may provide an explanation for the high HNC/HCN ratio observed in cold clouds. Additional observational evidence that formation of H_2NC^+ from NH_3 may be responsible for the excess HNC is the fact that the observed HNC/HCN ratio is greatest at the position in L134N which also has the greatest NH_3 abundance.

if the above scheme for producing excess HNC holds true, the effect may actually be greater than the observations suggest.

Reactions of HCN and HNC with other ions, such as HCO^+ and H_3^+ ,



or

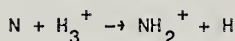


tend to reshuffle the HNC/HCN abundance since these reactions only form the HCNH^+ isomer, and not the H_2CN^+ isomer (Watson and Walmsley 1982). This reshuffling would drive the HNC/HCN ratio back toward unity, hence the HNC/HCN ratio excluding reshuffling would be greater than

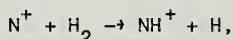
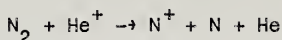
observed. Clearly, the chemistry which determines the HNC/HCN abundance ratio in interstellar clouds is not settled.

v) NH_3

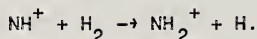
The formation of ammonia has been discussed by Huntress and Anicich (1976), Herbst and Leung (1986a), and Millar *et al.* (1987). The reaction scheme leading to NH_3 begins with formation of NH_2^+ by:



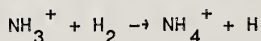
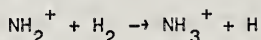
or, alternately



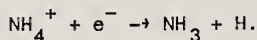
which is predicted to be very slow at low temperatures by Marquette *et al.* (1985), followed by



After NH_2^+ formation both schemes proceed by



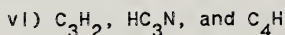
and



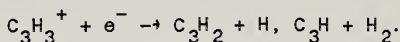
Dissociation of NH_3 occurs slowly with other ions, which form NH_4^+ and recycle back to NH_3 (Prasad and Huntress 1980b). Although conversion to HCN or HNC as described above provides a minor loss mechanism, NH_3 is a sink and its abundance increases with cloud age. The combination of both schemes for production of the precursor NH_2^+ leads to a

chemical model which can account for the observed ammonia abundance in cold clouds (Millar *et al.* 1987).

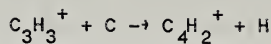
The paradox observed in L134N that the NH_3 has a very narrow distribution despite its low value for n^* of $2 \times 10^4 \text{ cm}^{-3}$, which indicates it should be easily excited at low densities (see Figure 5.10), has a possible explanation in a consideration of the ammonia chemistry. Millar *et al.* (1987) propose that at low visual extinctions, characteristic of regions of low molecular column density, a high neutral carbon, C I, abundance results from the photodissociation of CO. Reactions with C I tend to deplete the abundance of NO, which is a precursor of molecular nitrogen, N_2 . In the above production scheme for ammonia, N_2 is necessary to initiate one of the reaction pathways which leads to NH_2^+ , a link in the chain which leads to NH_3 . Hence, NH_3 production may be inhibited in regions of low visual extinction, and only in the highest density regions can the reaction scheme proceed which leads to formation of NH_4^+ through molecular nitrogen.



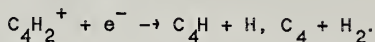
Three molecules which were observed in L134N, C_3H_2 , HC_3N , and C_4H , all can be formed from the precursor ion C_3H_3^+ . C_3H_2 is formed from C_3H_3^+ by electron recombination (Thaddeus *et al.* 1985, Adams and Smith 1987)



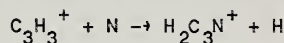
Herbst *et al.* (1984) form C_4H from $C_3H_3^+$ by the carbon fixation reaction



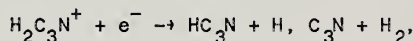
followed by electron recombination



The branching ratio for this reaction is unknown but Herbst (1983) proposes that each product is equally probable. Herbst *et al.* (1984) similarly form HC_3N by the reactions

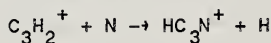


and

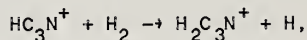


with a branching ratio that favors production of HC_3N over C_3N by factor of 14:1 (Millar *et al.* 1987).

While current chemical models include the above reactions as the only C_3H_2 formation mechanism, other pathways for HC_3N and C_4H have been proposed. Millar and Freeman (1984a, b) and Leung, Herbst, and Huebner (1984) form HC_3N by the reactions:

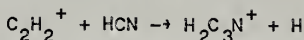


followed by

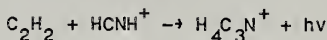


and electron recombination as above. However, Herbst (1983) suggests that radiative association reactions of hydrocarbon ions with molecular hydrogen may not proceed, in which case this is not a plausible mechanism for HC_3N formation.

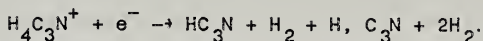
Alternatively, Prasad and Huntress (1980b) form HC_3N by



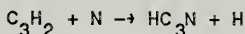
followed by the above electron recombination reaction, and by



and

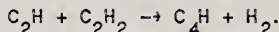


Also suggested is the neutral - neutral reaction

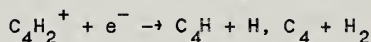
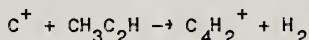


(Herbst 1983).

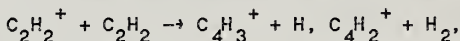
Millar *et al.* (1987) propose that the major formation mechanism for C_4H is the reaction



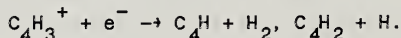
In addition, Millar and Freeman (1984a, b) form C_4H by the scheme



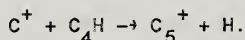
and Herbst (1983) proposes the condensation reactions



followed by electron recombination to form C_4H by



Destruction of C_4H is mostly by the reaction



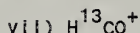
It is evident from the above discussion of dominant reaction pathways that the molecules HC_3N , C_3H_2 , and C_4H have an interrelated chemistry. High correlation coefficients for HC_3N and C_3H_2 verify that

they are closely chemically related. Correlation coefficients for C_4H are not reliable because of the limited observations, but all three molecular abundances peak at the high density position indicated by the peak in C_3H_2 and NH_3 Integrated Intensity maps. This is also the region determined to have a peak in the C/O abundance ratio.

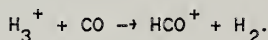
Hydrocarbons form readily in regions of high C/O abundance (Herbst and Leung 1986a) and, since hydrocarbon chemistry is the foundation for the formation of C_3H_2 , HC_3N , and C_4H , it is not surprising that these three molecules peak at the same position. Any other molecular species formed through hydrocarbon chemistry can also be expected to have an intensity peak at this position.

Tabulated in Table 6.7 are the HC_3N/C_3H_2 and the C_4H/C_3H_2 abundance ratios for the seven positions in the NRAO survey in which all three species were observed. At the peak hydrocarbon position, (1,3), HC_3N is a factor of 3 less abundant than C_3H_2 , while C_4H is a factor of 3 more abundant than C_3H_2 . Since the electron recombination reaction rates are approximately the same, if all three molecules were formed only from the precursor $C_3H_3^+$ ion, all three would have approximately the same abundance providing reactions of $C_3H_3^+$ with atomic carbon and nitrogen proceed rapidly. These results suggest that the other pathways for C_4H production are active, while the other pathways proposed for HC_3N formation may not be productive as was suggested by Herbst (1983). In addition, a depletion of atomic nitrogen, perhaps caused by N_2 or NH_3 formation, or an increase in the HC_3N destruction rates compared to C_3H_2 and C_4H destruction rates

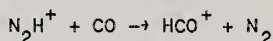
(Herbst 1983) may be responsible for the low HC_3N abundance as compared to C_3H_2 and C_4H .



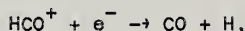
The principle formation mechanism for HCO^+ is ion-molecule reactions between CO and a protonated molecule. The most important of these would be the reaction with the abundant species H_3^+ (Huntress and Anicich 1976)



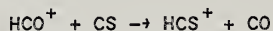
Another important reaction is



(Herbst et al. 1975). Destruction of HCO^+ occurs predominantly by electron recombination

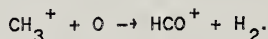


although a reaction with CS,



may also contribute to the destruction process.

Prasad and Huntress (1980b) propose HCO^+ formation through the reaction



Also, Herbst (1983) proposes formation of HCO^+ by this and other reactions of hydrocarbon ions with oxygen. This production scheme seems reasonable in L134N considering that H^{13}CO^+ is seen to peak in the region of high hydrocarbon abundance. Hence, the high abundance of

HCO^+ in this region may be due to its formation through hydrocarbon ions, which would be most abundant in the high C/O region of the core. Previous estimates of the oxygen abundance at the (0.6,2.9) position indicate that it is depleted by a factor of five from the most oxygen rich position, but there is still enough free O for this reaction to proceed. H^{13}CO^+ formation from hydrocarbon species, which are shown to be prominent in the dense core region, along with the high density requirements for H^{13}CO^+ excitation, indicate that the observed H^{13}CO^+ J=1-0 emission is indeed probing the dense core region of L134N.

The estimated abundance for H^{13}CO^+ at the (0.6,2.9) peak position indicates that HCO^+ is one of the most abundant species in the core region of L134N. The HCO^+ J=1-0 transition was determined to be optically thick and self-absorbed by (Langer *et al.* 1978), but the observed $\text{H}^{13}\text{CO}^+/\text{HC}^{18}\text{O}^+$ column density ratio indicates that H^{13}CO^+ J=1-0 emission is optically thin (as previously discussed). Hence, the observed $\text{H}^{13}\text{CO}^+/\text{HC}^{18}\text{O}^+$ abundance ratio of 7.4 ± 2.6 may indicate slight $^{13}\text{C}/^{12}\text{C}$ fractionation (Langer *et al.* 1984), but to within the errors of the measurement the $^{13}\text{C}^{16}\text{O}/^{12}\text{C}^{18}\text{O}$ abundance ratio determined from H^{13}CO^+ and HC^{18}O^+ is consistent with a terrestrial value of 5.5 and no fractionation occurring within the dense core of L134N.

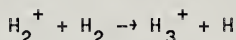
From consideration of the most prominent reactions for formation and destruction of HCO^+ , that is formation by $\text{CO} + \text{H}_3^+$ with a rate constant of $1.7 \times 10^{-9} \text{ cm}^3 \text{ s}^{-1}$ and destruction by electron recombination with a rate constant of $1.9 \times 10^{-6} \text{ cm}^3 \text{ s}^{-1}$ (Graedel, Langer, and Frerking 1982), chemical equilibrium yields the equation:

$$\frac{[\text{H}_3^+]}{[\text{e}]} = 1100 \frac{[\text{HCO}^+]}{[\text{CO}]} \quad (6.2)$$

where $[X]$ is the modeled number density of species X with respect to the number density of H_2 . At the (0.6,2.9) position the observed $\text{HC}^{18}\text{O}^+/\text{C}^{18}\text{O}$ column density ratio implies $[\text{H}_3^+]/[\text{e}]$ is about 0.17. Other HCO^+/CO abundance ratios based on the observed H^{13}CO^+ and C^{18}O spectra, along with an assumed $^{13}\text{C}^{16}\text{O}/^{12}\text{C}^{18}\text{O}$ terrestrial ratio of 5.5, are presented in Table 6.6. The C^{18}O isotope is used in this case because it is optically thin and has not been shown to suffer isotopic fractionation as does ^{13}CO (Langer et al. 1980). Guellin, Langer, and Wilson (1982) and Wootten et al. (1982) have determined the electron abundance at the (0,0) position in L134N from observations of deuterated HCO^+ to be $[\text{e}] = 2 \times 10^{-7}$. Calculations of Guellin, Langer, and Wilson indicate that the electron density does not vary appreciably across the L134N core, so $[\text{H}_3^+] = 3 \times 10^{-8}$ at the (0.6,2.9) position. However, more recent laboratory measurements of the H_3^+ electron recombination rate indicate a value of $2 \times 10^{-8} \text{ cm}^3 \text{ s}^{-1}$ (Smith and Adams 1984), which suggests that this H_3^+ abundance must be considered an upper limit. Under the further assumption that the $^{18}\text{O}/^{16}\text{O}$ abundance ratio is the terrestrial value of 489, the HCO^+ abundance is found to be 1.3×10^{-8} based on the HC^{18}O^+ observations. This close agreement

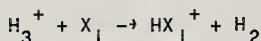
between the abundances for H_3^+ and HCO^+ indicate that HCO^+ is the predominant ion formed from reactions of H_3^+ as a result of the high abundance of CO.

Consideration of the chemical balance equations for the H_3^+ ion allows for independent determination of the H_3^+ abundance. H_3^+ is formed from H_2^+ , which is formed by a cosmic ray ionizing a H_2 molecule. The rate of H_2^+ formation is $n(H_2)\zeta$, where ζ is the cosmic ray ionization rate determined to be $4 \times 10^{-17} \text{ s}^{-1}$ for H_2 molecules in dark clouds (Goldsmith and Langer 1978) and $n(H_2)$ is the molecular hydrogen number density determined to be $3 \times 10^4 \text{ cm}^{-3}$ at the L134N core from the previous NH_3 and HC_3N analysis. H_3^+ is then formed from the reaction



with a rate constant of $k_f = 2.1 \times 10^{-9} \text{ cm}^3 \text{ s}^{-1}$ (Bowers et al. 1969).

H_3^+ destruction occurs by electron recombination at a rate constant k_e and by reaction with molecule X_1 of the form



at a rate constant k_1 . The most important of these reactions will be

$X_1 = CO$ and $k_{CO} = 1.7 \times 10^{-9} \text{ cm}^3 \text{ s}^{-1}$ (Graedel, Langer, and Frerking 1982). The rate constant k_e is determined to be $< 2 \times 10^{-8} \text{ cm}^3 \text{ s}^{-1}$ by Adams, Smith, and Alge (1984), and Herbst and Leung (1986a) use $1.3 \times 10^{-8} \text{ cm}^3 \text{ s}^{-1}$ which will be assumed here. Hence

$$[H_3^+] = \frac{\zeta}{n(H_2)} \frac{1}{([e]k_e + [CO]k_{CO})} \quad (6.3)$$

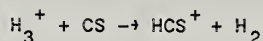
and with the appropriate values as given above, $[H_3^+] = 1 \times 10^{-8}$ which is consistent with the value of $[H_3^+]$ determined above, indicating that these are the dominant reactions in the $[H_3^+]$ chemistry.

These values determined for $[H_3^+]$ must be considered lower limits whenever a isotopic form of HCO^+ is compared with the corresponding isotopic form of CO because of the differences in excitation conditions between HCO^+ and CO. Conclusions previously presented claim $C^{18}O$ to be excited in a lower density gas than exists at the high density core, where the $HC^{18}O^+$ emission is observed. Hence the two transitions may not be sampling the same region of the cloud along the line of sight.

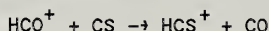
If a cloud core is neutral, the electron abundance must be the same as the total ion abundance. Along with the molecular ions, atomic ions exist in the core region. The sum of the observed and deduced molecular ion abundances of H_3^+ , HCO^+ , N_2H^+ , and HCS^+ total to approximately 3×10^{-8} at the (0.6, 2.9) position. However, an upper limit to electron abundance assumed at that position was 2×10^{-7} , a factor of 7 greater. Therefore, atomic ions may comprise as much as 90 percent of the ion content of the cloud.

viii) HCS^+

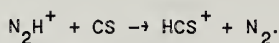
The chemistry of the HCS^+ ion is discussed by Prasad and Huntress (1982) and Millar (1983). The principle formation mechanism is through the reaction



but other formation reactions include



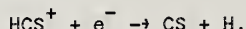
and



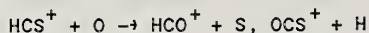
In addition, formation of HCS^+ may occur by



however, the rate constant for this reaction is small (Millar 1983) and the abundance of CS^+ is believed to be low, so that this reaction is not of importance in the HCS^+ formation scheme. Destruction of HCS^+ occurs by electron recombination



In regions of high oxygen abundance Prasad and Huntress (1982) also suggest



as a means of HCS^+ destruction.

Chemical balance of the above reaction scheme produces the equation

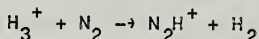
$$\frac{[\text{HCS}^+]}{[\text{CS}]} = \frac{[\text{H}_3^+]k_1 + [\text{HCO}^+]k_2 + [\text{N}_2\text{H}^+]k_3}{[e^-]k_e} \quad (6.4)$$

where the HCS^+ reaction with O has been assumed to not be of importance in dense regions. The rate constant for the electron recombination reaction is uncertain, but other rate constants are given by Prasad and Huntress to be $k_1 = 2 \times 10^{-9}$, $k_2 = k_3 = 1 \times 10^{-9} \text{ cm}^{-3} \text{ s}^{-1}$. Using an assumed $k_e = 3 \times 10^{-7}$, also from Prasad and Huntress, gives $[\text{HCS}^+]/[\text{CS}] \approx 5 \times 10^{-4}$. The observed values of $[\text{HCS}^+]/[\text{CS}]$ were determined from the HCS^+ and C^{34}S column densities, along with an assumed terrestrial $^{32}\text{S}/^{34}\text{S}$ abundance ratio of 22.5 (since the CS emission is self-absorbed and may underestimate the true CS abundance), and are listed in Table 6.6. These values range from 4.1×10^{-2} to 8.4×10^{-2} , hence are typically a factor of about 100 greater than predicted. The difference must be attributed to either other production pathways for HCS^+ , a lower electron abundance, or a lower electron recombination constant of about $3 \times 10^{-9} \text{ cm}^3 \text{ s}^{-1}$. A rate constant of $7 \times 10^{-9} \text{ cm}^3 \text{ s}^{-1}$ has also been suggested by Millar (1983) as representative of the HCS^+ electron recombination.

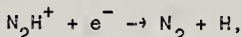
Millar (1983) uses the abundance ratio HCS^+/CS as a indicator of the total molecular hydrogen abundance in a cloud core. He finds that the HCS^+/CS ratio decreases with increasing density. Data from the FCRAO survey in Table 6.6 indicates that this ratio is lower in the higher density regions as determined from the previous NH_3 analysis, hence the HCS^+/CS ratio in L134N follows this trend. However, the observed ratios are almost an order of magnitude greater than predicted by Millar.

1x) N_2H^+

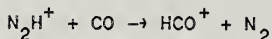
Formation of N_2H^+ occurs almost exclusively through the reaction



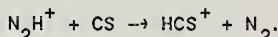
and Herbst *et al.* (1975) have determined a reaction rate of $1.8 \times 10^{-9} \text{ cm}^3 \text{ s}^{-1}$. Destruction of N_2H^+ can occur by electron recombination



an ion-molecule reaction with CO



where Herbst *et al.* have determined this reaction rate to be $8.8 \times 10^{-10} \text{ cm}^3 \text{ s}^{-1}$, or less importantly by an ion-molecule reaction with CS



Steady-state chemical balancing yields the equation

$$\frac{[N_2H^+]}{[N_2]} = \frac{[H_3^+]k_f}{[e]k_e + [CO]k_{CO}} \quad (6.5)$$

where the reaction with CS has been neglected. With the reaction rates k_f and k_{CO} determined by Herbst *et al.*, the N_2H^+ and CO abundances estimated from the observations, and the H_3^+ abundance previously determined, the only unknowns in this equation are the N_2 abundance and the electron recombination reaction rate, k_e . Assuming a value for the rate k_e of $2 \times 10^{-6} \text{ cm}^3 \text{ s}^{-1}$, the same as for HCO^+ recombination (Smith and Adams 1984), the abundance for N_2 in the dense core region is approximately 2×10^{-5} . Estimates of the N/H_2 abundance ratio range from 2×10^{-4} (Allen 1981) suggesting that approximately ten percent of interstellar nitrogen is in the form of N_2 .

TABLE 6.6

FCRAO ABUNDANCE RATIOS

position	$\frac{[\text{SO}]}{[\text{SO}_2]}$ ^a	$\frac{[\text{C}]}{[\text{O}]}$	$\frac{[\text{CS}]}{[\text{SO}]}$ ^b	[O]	[C]	$\frac{[\text{HCO}^+]}{[\text{CO}]}$ ^c	$\frac{[\text{HCS}^+]}{[\text{CS}]}$ ^d
	(0.6, 2.9)	>15.	>1.3	0.60	8.7×10^{-7}	$>1.1 \times 10^{-6}$	2.0×10^{-4}
(0.7, 0.7)	11.	1.3	0.32	1.4×10^{-6}	1.8×10^{-6}	2.3×10^{-4}	4.2×10^{-2}
(-0.8, 0.4)	4.9	1.2	0.30	1.5×10^{-6}	1.8×10^{-6}	5.8×10^{-5}	8.6×10^{-2}
(-1.4, -0.8)	8.4	1.2	0.15	4.5×10^{-6}	5.3×10^{-6}	1.3×10^{-4}	4.2×10^{-2}
(-2.8, 0.8)	>8.8	>1.2	0.53	9.3×10^{-7}	$>1.1 \times 10^{-6}$	3.3×10^{-5}	6.4×10^{-2}
(-2.3, 2.0)	>1.4	>1.0	0.24	1.9×10^{-6}	$>1.9 \times 10^{-6}$...	8.7×10^{-2}
(3.7, -1.2)	>2.1	>1.1	0.32	1.4×10^{-6}	$>1.5 \times 10^{-6}$	1.9×10^{-5}	7.6×10^{-2}

^a $[\text{SO}]/[\text{SO}_2] = N(\text{SO}(2,2-1,1)) / N(\text{SO}_2)$;

except (-2.3, 2.0) where $[\text{SO}]/[\text{SO}_2] = 22.5 N(^{34}\text{SO}) / N(\text{SO}_2)$

^b $[\text{CS}]/[\text{SO}] = N(\text{C}^{34}\text{S}) / N(^{34}\text{SO})$

^c $[\text{HCO}^+]/[\text{CO}] = N(\text{H}^{13}\text{CO}^+) / 5.5 N(\text{C}^{18}\text{O})$

^d $[\text{HCS}^+]/[\text{CS}] = N(\text{HCS}^+) / 22.5 N(\text{C}^{34}\text{S})$

TABLE 6.7

NRAO ABUNDANCE RATIOS

position	$\frac{[\text{HC}_3\text{N}]}{[\text{C}_3\text{H}_2]}$	$\frac{[\text{C}_4\text{H}]}{[\text{C}_3\text{H}_2]}$
(0,0)	0.18	2.9
(-2,-1)	<0.10	9.1
(-3,1)	0.67	36.
(4,-1)	<0.19	<11.
(0,2)	0.30	4.8
(1,1)	0.36	<2.8
(1,3)	0.29	3.3

CHAPTER VII

SOURCE MODEL

In the previous two chapters the physical parameters and chemistry of L134N have been discussed. In this chapter these two aspects which define the state of the dark cloud are brought together to form a model of the source in order to explain the differences in the observed molecular emission distributions. In the extreme limits, these observations could be attributed to two effects. Either the relative abundances for the molecular species are constant, with the different distributions being caused by varying excitation due to gradients in density, temperature, or total gas column density; or the physical conditions within the source are constant, with varying gas phase chemical abundances. In reality, the distribution differences are probably a complex combination of both effects.

a) excitation differences

The $C^{18}O$ map is tracing a lower excitation envelope surrounding the high density core. Evidence for this includes the characteristic density for $C^{18}O$ $J=1-0$ emission being about $10^{3.5} \text{ cm}^{-3}$ as determined from the average $C^{18}O$ map density calculated in Chapter II and the LVG models of $C^{18}O$ $J=1-0$ in Chapter V (see Figure 5.2).

The ease with which CO is chemically produced is attested to by the uniformity of the $C^{18}O$ emission. CO formation occurs until either all the carbon or oxygen has gone into CO, and the abundance is assumed to be constant across the core region. Combined with the results that the $C^{18}O$ J=1-0 transition is not optically thick and the gas temperature is constant across the core, constant abundance means $C^{18}O$ is tracing the total molecular column density through the core (Schloerb, Snell, and Schwartz 1987).

As previously indicated, the NH_3 , $H^{13}CO^+$, and hydrocarbon species seem to peak in the high density core where the density is about $10^{4.5} \text{ cm}^{-3}$ as determined from NH_3 and HC_3N results (Chapter IV). These species have high density excitation requirements and their presence at this location indicates that the difference between these distributions and $C^{18}O$ is an excitation effect. In addition, transitions emanating from the high density core all have narrow emission lines without line wings or self-absorption indicating that this core is quiescent and excitation of these transitions outside the core in a lower density region does not occur.

Although some molecular emission differences are a result of density induced excitation effects, a constant kinetic temperature of about 12 K was found for the core region from both the NH_3 and ^{12}CO transitions which are probing the two extremes in density for the

molecular emission. Hence, variations in excitation due to temperature effects do not occur.

b) chemical differences

The CS and SO have similar, high density, excitation requirements, yet different distributions which are not due entirely to the high optical depths of the individual spectra. There is a line of evidence which suggests that CS and SO exist in low density gas outside the dense core, and their observed spectral lines in L134N contain significant emission from this low density region. Both CS and SO have asymmetric line profiles indicating large scale motions (Myers 1980) which occur in a outer, less quiescent region than probed by transitions of species observed in the dense core. CS $J=2-1$ and SO $N, J=2,3-1,2$ line widths are approximately 50 percent broader than line widths of transitions believed to arise only from the quiescent core indicating more extended emission along the line of sight, hence from regions of lower density. Also, both transitions have signs of self-absorption indicating that some CS and SO exists in a lower excitation foreground gas. That CS and SO are abundant in low density gas is not unreasonable considering the ease at which they both are chemically produced.

A possible explanation for the observed CS and SO distribution difference is a C/O gas phase abundance gradient. This C/O gradient may be reflected in the formation of CS from sulfur in a region of

excess carbon after CO formation, and formation of SO from sulfur in a region of excess oxygen abundance after CO formation since SO formation occurs through neutral - neutral reactions requiring a high oxygen abundance. A projection of these two regions on the sky may account for some of the overlap of the maps.

Further evidence for this C/O gradient lies with other observed species. Surveyed molecular species indicate that the position of maximum NH_3 intensity is where products of a hydrocarbon chemistry are most abundant and where oxygen bearing species are not readily detected. Hence, the high density core region of L134N must have a relatively high C/O ratio. If hydrocarbon species require a low oxygen abundance environment in which to form (Millar, Leung, and Herbst 1987), this high C/O ratio may not necessarily reflect a high carbon abundance, but may be a result of oxygen depletion.

The oxygen depletion may be a function of density. The region of the cloud characterized by the SO $N, J=2,3-1,2$ emission does not include the NH_3 density peak. In fact, the SO peak lies on the $10^{3.5} \text{ cm}^{-3}$ contour level of the H_2 density map derived from the NH_3 (1,1) transition. Since the density map derived from ammonia observations is really a convolution of H_2 density with ammonia abundance, the density at this position may be higher than $10^{3.5} \text{ cm}^{-3}$. However, this derivation of density depends on the ratio of the NH_3 (1,1) hyperfine satellite line to the main line and it should not suffer from the above effect at this location where the NH_3 (1,1) lines are still readily

detected. Additionally, it has been argued that SO emission emanates from a lower density region. Since SO is easily formed in regions of high oxygen abundance, the SO map may reflect a less dense region of the core where oxygen is not depleted, and hydrocarbon formation is inhibited by less visual extinction and a high oxygen abundance. Modeled oxygen abundances indicate that atomic oxygen is depleted by a factor of five at the NH_3 density peak as compared to the SO distribution peak (see Chapter VI).

In addition, the oxygen bearing species H^{13}CO^+ is seen to have emission extended into the region where SO peaks. The H^{13}CO^+ distribution has a peak at the northern NH_3 and C_3H_2 peak, but that peak is not as sharp as the other species. The peak at the (0.6,2.9) position may be a result of the combination of a high excitation requirement for the H^{13}CO^+ $J=1-0$ transition and reactions of oxygen with abundant hydrocarbon molecules at that position. The extension of H^{13}CO^+ into the SO distribution region may be attributed to the high oxygen abundance there. In this regard, H^{13}CO^+ seems to be intermediate between species found in the dense core region and SO related species.

A possible cause of the oxygen depletion in the dense core could be removal of oxygen from the gas phase through the condensation of H_2O onto dust grains. The water would exist on the grain in the form of an ice mantle which would coat the silicate grain. Evidence for this mechanism occurring in dense clouds lies in observations of the 3.07

micron H_2O absorption feature (Harris et al. 1978). In addition, this feature is only detected toward reddened stars behind high density molecular clouds with large extinctions (Hagen et al. 1983). Harris et al. suggest a relationship between water ice abundance and density of interstellar matter based on an increase in the observed absorption strength of the 3.07 micron feature as a function of opacity in regions of interstellar clouds. Calculations by Hagen et al. suggest that this feature is due to pure water ice mantles which form around a silicate grain. However, Leger et al. (1983) model the 3.07 micron feature line wings as a mixture of two-thirds water and one-third ammonia; and Knacke et al. (1982) find the wings are fit by a mixture of water to ammonia in a ratio of 4:1. These results lead to a high abundance of NH_3 on dust grain mantles, perhaps as high as twenty times more ammonia in mantles than in the gas phase (Knacke et al.).

Two possible reasons why water ice should preferentially condense onto a grain are suggested. (1) H_2O does have the highest condensation temperature of known interstellar molecules, indicating that it would be the first to condense out of a molecular gas (Yamamoto 1985) and NH_3 also has a relatively high condensation temperature. However, the kinetic temperature in the L134N core is observed to be constant and the proposed oxygen depletion is a function of density. (2) Blake et al. (1987) propose that C, N, and O all readily stick to grain mantles and react with H and H_2 on the grain surface to form the fully hydrogenated end products CH_4 , NH_3 , and H_2O . CH_4 is most easily evaporated due to its nonpolar nature, which puts carbon back into the

gas phase, leaving a $\text{NH}_3 - \text{H}_2\text{O}$ ice mantle. Since collisions between gas phase atoms and molecules with grains increase as a function of density, this mechanism would be more efficient in high density regions. Details of the H_2O formation on grain mantles must await further investigations of grain properties and chemistry.

c) L134N age

The combination of physical and chemical models for dark clouds allow an estimate of the age of L134N. A lower limit can be set from the consideration of the free-fall collapse time from Chapter II to be approximately 10^6 years. An upper limit can be set by assuming the L134N molecular core has not yet reached steady-state chemistry. Chemical models (Leung, Herbst, Huebner 1984) indicate that a chemical steady-state should be reached in 10^7 years at dark cloud densities. Possible arguments that L134N is not yet at steady-state include the SO/SO_2 ratio. Watt and Charnley (1985) argue that in the later stages of chemical evolution all SO is converted into SO_2 . The high SO abundance in L134N would indicate that this cloud is chemically young.

Secondly, Phillips and Huggins (1981) have observed the atomic carbon (C I) transition at 492 GHz at the (0,0) position in L134N and found a C I/CO column density ratio of approximately 1/20. It is generally believed that C I should be confined to the edges of a cloud, up to approximately the penetration depth of the interstellar ultraviolet radiation (Tielens and Hollenbach 1985). However, recent

observations indicate that CI is more uniformly mixed throughout the cloud (Keene *et al.* 1985). If CI does exist in the core region, two alternatives have been suggested to explain its presence there. Either turbulent mixing occurs between the core and edges of the cloud (Boland and de Jong 1982); or it is a result of incomplete conversion of atomic carbon into the molecular state by the gas phase chemistry (Langer *et al.* 1984). For the latter case, the model of Leung, Herbst, and Huebner indicate an age of approximately 10^6 years for the observed CI/CO ratio.

However, the CI data of Phillips and Huggins does not clearly indicate that CI is emanating from the core region. Examination of the L134N CI spectra of Phillips and Huggins reveals a double peaked structure with a large peak at 3.7 km s^{-1} , a second peak at 2.3 km s^{-1} , and a dip in the spectra at 2.8 km s^{-1} . Two possible explanations exist which would produce these features. First, the CI emission could be coming from two different regions in velocity space, one at 2.3 km s^{-1} , which is the characteristic velocity of molecular transitions observed in the dense core, and one at 3.7 km s^{-1} . Alternatively, the CI emission is singly peaked at about 2.8 km s^{-1} and suffers from self-absorption by a lower excitation foreground gas. In view of the fact that self-absorption is common in other high column density species in L134N and the fact that multiple velocity components have not been observed in any other species, the latter explanation would seem to be true in this case. The high velocity of the self-absorption feature at 2.8 km s^{-1} , as compared to the a typical velocity with respect to the

local standard of rest of about 2.5 km s^{-1} found for other transitions, may be attributed to the CI emission arising more toward the cloud edge.

In addition, Stahler (1984) estimates the age of L134N to be 3.3×10^5 years based on chemical models of cyanopolyynes formation. This age is the same as the free-fall collapse time for C^{18}O obtained in Chapter II and must be considered a lower limit. However, all lines of evidence suggest that L134N is a relatively young cloud and may be a future site of low mass star formation.

d) summary of source model

A model to explain the observed differences in the distributions of molecular emission from the dark cloud L134N has been proposed. A brief summary of that model is presented here.

L134N has a high density core, $n(\text{H}_2)$ of $3 \times 10^4 \text{ cm}^{-3}$, characterized by maps of NH_3 , C_3H_2 , H^{13}CO^+ , and the surveyed distributions of hydrocarbon molecules. In this high density region, oxygen is depleted from the gas phase by condensation of water ice onto dust grain mantles. This core may be the site of future star formation.

As indicated by the NH_3 map, density decreases with distance from the high density condensation. To the north of the NH_3 peak, a sharp edge of the cloud is observed in ^{13}CO . This umbrella shaped edge

defines the upper boundary of molecular formation due to the dissociating effects of the interstellar ultraviolet radiation field in regions of low extinction.

Southwest of the high density core lies a region characterized by the map of SO. This region is still embedded deep enough within the cloud for molecular formation to occur. However, an enhanced oxygen abundance relative to the NH₃ peak results in the formation of SO and SO₂. This enhanced oxygen abundance may be the result of lower densities, hence less condensation of gas phase atoms and molecules on grains.

A low density envelope is characterized by the C¹⁸O emission, which is excited by densities on the order of $10^{3.5} \text{ cm}^{-3}$. There are no apparent energy sources embedded within the cloud and a relative constant kinetic temperature of 12 K is determined over the core region.

e) TMC 1

Another dark cloud, TMC 1, has been the object of many molecular line observations. TMC 1 is also nearby, lying at a distance of 140 parsec (Elias 1978), hence observations can obtain comparable spatial resolution to L134N. In terms of temperature, density, and size, L134N and TMC 1 are very similar. Yet, despite these similarities, these two clouds appear chemically different. For example, cyanopolyynes appear to be more abundant in TMC 1 than in L134N (Snell *et al.* 1981), however sulfur bearing molecules appear to be more abundant in L134N than TMC 1 (cf. Irvine, Good, and Schloerb 1983; Irvine *et al.* 1985). Possible explanations for these observations include: (1) dark molecular clouds form from different initial conditions which produce differing chemistries between the clouds; (2) molecular clouds undergo a chemical evolution (Leung, Herbst, and Huebner 1984), such that L134N and TMC 1 are currently at different stages of a chemical evolutionary sequence; and (3) emission from various molecules is excited by slight physical differences which exist between L134N and TMC 1 (Millar and Freeman 1984b).

Transitions that have been mapped in TMC 1 show a narrow filamentary structure in NH_3 (Little *et al.* 1979), HC_3N (Toile *et al.* 1981; Schloerb, Snell, and Young 1983), HC_5N (Churchwell, Winnewisser, and Walmsley 1978), C_2H (Wootten *et al.* 1980), CS (Snell *et al.* 1982), and HCO^+ (Guellin, Langer, and Wilson 1982). Schloerb, Snell, and Young model TMC 1 as a filament with a constant density of about 10^5 cm^{-3} ,

which is a slightly higher density than exhibited by L134N. Tolle et al. estimate a kinetic temperature of 10 K from NH_3 observations.

The vast number of observations of TMC 1 and L134N have not as yet given a clear reason for the abundance differences. Certainly if the initial atomic abundances were different for each cloud, they would each evolve a different chemistry. But there are no clear indications as to why their initial conditions should vary. Both are at the relatively the same position in the galaxy, and barring any cataclysmic events near one of them and not the other at an earlier stage of evolution, they should have similar elemental abundances.

Another possibility is that TMC 1 and L134N are at different stages of a chemical evolution. Stahler (1984) suggests that TMC 1 is three times as old as L134N based on modeling abundances of cyanopolyynes. Time dependent models of chemistry, such as Leung, Herbst, and Huebner (1984), indicate the abundances of hydrocarbon chain molecules should peak in dark clouds between 10^5 and 10^6 years, and TMC 1 being older than L134N may explain the increase in abundance of these molecules. However, models of sulfur chemistry (e.g., Watt and Charnley 1985) indicate that SO abundance should also increase with age, hence, provided TMC 1 and L134N have the same elemental abundance of sulfur, SO would be observed to be more abundant in TMC 1.

Alternatively, these observations are consistent with the above model presented for L134N being applicable to TMC 1 in a number of

ways. First, the higher abundance of hydrocarbon chain molecules in TMC 1 may be a result of the slightly higher density leading to more oxygen depletion onto grains. Secondly, NH_3 is observed to be slightly less abundant in TMC 1 than L134N (Irvine *et al.* 1985), which is again consistent with larger $\text{NH}_3\text{-H}_2\text{O}$ grain mantles in TMC 1. In addition, the CS map of Snell *et al.* (1982) could be a result of sulfur going into CS formation in the densest regions of the cloud, where the oxygen is depleted.

If such a model were used to explain the distribution of SO in TMC 1, the SO should form a cylindrical shell around the high density filament. Searches for SO along the high density ridge would look through the lowest column density of SO. Instead, SO should have the highest column density along the filament edges. SO has been observed in TMC 1 by Rydbeck *et al.* (1980) at two positions within the ridge. These spectra show a multiple velocity structure with one component at the NH_3 velocity and another more intense component at a lower velocity, which Rydbeck *et al.* suggest arises in a lower density region. A more detailed mapping of SO in TMC 1 at high spectral resolution would be useful in order to determine the SO distribution.

CHAPTER VIII

CONCLUSIONS AND PROSPECTUS

a) conclusions

The dark cloud L134N has been studied in detail through millimeter and centimeter wavelength emission line spectra. The principal results are as follows:

1. The large scale structure has been probed with the ^{13}CO J=1-0 transition which has revealed a hierarchal structure for the L134N cloud. This structure is suggestive of fragmentation and collapse models which have been developed for the formation of protostars. The total mass of the L134N cloud derived from ^{13}CO observations is 190 solar masses.
2. The ^{13}CO J=1-0 transition fails to reveal a core of molecular gas, hence ^{13}CO is not a good tracer of high density molecular gas in nearby dark clouds.
3. A high density core of molecular gas exists in L134N which has a kinetic temperature of approximately 12 K, a peak molecular hydrogen density of about $10^{4.5} \text{ cm}^{-3}$, a mass of approximately 23 solar masses

determined from $C^{18}O$ J=1-0 emission, and may be the site of future star formation.

4. Maps of the emission from $C^{18}O$, CS, $H^{13}CO^+$, SO, NH_3 , and C_3H_2 reveal different distributions. These differences result from $C^{18}O$ probing a less dense envelope; NH_3 , C_3H_2 , and $H^{13}CO^+$ excitation from a high density condensation; CS emission suffering self-absorption and high opacities; and SO emission emanating from a region of high oxygen abundance.

5. A consistent set of LTE chemical abundances has been estimated at as many as seven positions, which can be used to constrain chemical models of dark clouds.

6. A C/O abundance gradient exists within the core of L134N which is possibly caused by removal of oxygen from the gas phase in high density regions by the formation of H_2O mantles on dust grains.

7. The physics and chemistry of dark clouds are interrelated in a complex manner, hence chemical effects can not be ignored in the physical modeling of dark clouds.

Hence, the goals of developing a physical and chemical model for L134N, which may be applicable to other dark clouds and regions of star formation, have been met. In the future, further detailed studies of the physics and chemistry of regions of potential low mass star

formation may lead to information of conditions within pre-solar nebulae and to initial boundary conditions for solar system formation.

b) future endeavors

Although many of the results of this study were observations which yielded temperatures, densities, and gas phase abundances for many molecular species in L134N, at least the proposal of a C/O abundance gradient within the molecular core warrants further investigation.

The SO molecule is a potentially powerful tool for analysis of conditions in molecular clouds. The three-sigma electronic ground state structure of SO produces many rotational transitions observable in the millimeter range. However, a statistical equilibrium model for analysis of emission from these transitions has yet to be utilized. Problems which have prohibited this type of study include calculations of energy level structure and collisional cross sections for SO. Such an analysis would yield a more precise determination of the physical conditions within regions of SO emission. This would be particularly useful for L134N since the density at the SO peak was only inferred from other species.

A multitransitional study of CS in L134N would also be useful for determining the conditions which lead to CS excitation and help elucidate the distribution of CS which was masked by radiative transfer effects and weak line emission in the isotopically substituted

species. A detailed study of CS emission combined with a corresponding study of SO emission would considerably help in detailing the possible C/O abundance gradient.

Also helpful in this regard would be observations of optically thin oxygen bearing species such as OCS, HDO, HCOOH, or NO. The problem is that these lines are extremely weak in dark clouds. However, abundance determinations, at least at the NH_3 and SO peaks for some of these species, would lead to a better understanding of oxygen abundance and chemistry of the observed species.

Finally, observations of other sources could test whether this model is applicable elsewhere. Of particular interest is the SO distribution in dark clouds. As already mentioned, the SO distribution around TMC 1 has been predicted by this model to peak along the edges of the dense filament, and a detailed map of SO in this cloud would be desirable. Because of many transitions in the millimeter range, observations of SO in other environments, combined with a statistical equilibrium model, could be used to probe a wide range of physical conditions around newly formed stars and protostars, in outflow regions, and in shocked regions, as well as in other quiescent regions.

BIBLIOGRAPHY

- Adams, N.G., Smith, D., and Alge, E. 1984, *J.Chem.Phys.*, 81, 1778.
- Adams, N.G. and Smith, D. 1987, *Ap.J.Lett.*, 317, L25.
- Allen, C.W. 1981, *Astrophysical Quantities*, 3rd ed. (London: Athlone Press).
- Allen, T.L., Goddard, J.D., and Schaefer, H.F. III 1980, *J.Chem.Phys.*, 73, 3255.
- Bevington, P.R. 1969, *Data Reduction and Error Analysis for the Physical Sciences* (New York: McGraw-Hill).
- Blake, G.A., Sutton, E.C., Masson, C.R., and Phillips, T.G. 1987, *Ap.J.*, 315, 621.
- Bodenheimer, P., Tohline, J.E., and Black, D.C. 1980, *Ap.J.*, 242, 209.
- Boland, W. and de Jong, T. 1982, *Ap.J.*, 261, 110.
- Bowers, M.T., Elleman, D.D., and King, J. 1969, *J.Chem.Phys.*, 50, 4787.
- Caldwell, J.A.R. 1979, *Astron.Astrophys.*, 71, 255.
- Churchwell, E., Winnelisser, G., and Walmsley, C.M. 1978, *Astron.Astrophys.*, 67, 139.
- Churchwell, E., Nash, A.G., and Walmsley, C.M. 1984, *Ap.J.*, 287, 681.
- Clark, F.O. and Johnson, D.R. 1981, *Ap.J.*, 247, 104.
- Dickman, R.L. 1978, *Ap.J.Supp.*, 37, 407.
- Dickman, R.L., Snell, R.L., and Schloerb, F.P. 1986, *Ap.J.*, 309, 326.
- Ellas, J.H. 1978, *Ap.J.*, 224, 857.

- Evans, Neal J. II 1980, in *IAU Symposium 87, Interstellar Molecules*, ed. B.H. Andrews (Dordrecht:Reidel) pp. 1-19.
- Evans, N.J. II and Kutner, M.L. 1976, *Ap.J.Lett.*, 204, L113.
- Frerking, M.A., Langer, W.D., and Wilson, R.W. 1982, *Ap.J.*, 262, 590.
- Goldsmith, P.F. and Langer, W.D. 1978, *Ap.J.*, 222, 881.
- Goldsmith, P.F., Langer, W.D., Eddler, J., Irvine, W.M., and Kollberg, E. 1981, *Ap.J.*, 249, 524.
- Graedel, T.E., Langer, W.D., and Frerking, M.A. 1982, *Ap.J.Supp.*, 48, 321.
- Green, Sheldon 1975, *Ap.J.*, 201, 366.
- Green, Sheldon 1980, *J.Chem Phys.*, 73, 2740.
- Green, Sheldon and Thaddeus, Patrick 1974, *Ap.J.*, 191, 653.
- Green, Sheldon and Chapman, Sally 1978, *Ap.J.Supp.*, 37, 169.
- Guelin, M., Langer, W.D., and Wilson R.W. 1982, *Astron.Astrophys.*, 107, 107.
- Guelin, M., Friberg, P., and Mezaoui A. 1982, *Astron.Astrophys.*, 109, 23.
- Hagen, W., Tielens, A.G.G.M., and Greenberg, J.M. 1983, *Astron.Astrophys.*, 117, 132.
- Harris, D.H., Woolf, N.J., and Rieke, G.H. 1978, *Ap.J.*, 226, 829.
- Henkel, C., Wilson, T.L., and Bieging, J. 1982, *Astron.Astrophys.*, 109, 344.
- Herbst, E. 1978, *Ap.J.*, 222, 508.
- Herbst, E. 1983, *Ap.J.Supp.*, 53, 41.
- Herbst, E., Bohme, D.K., Payzant, J.D., and Schiff, H.I. 1975, *Ap.J.*, 201, 603.

- Herbst, E., Adams, N.G., and Smith, D. 1984, *Ap.J.*, 285, 618.
- Herbst E., and Leung, C.M. 1986a, *MNRAS*, 222, 689.
- Herbst E., and Leung, C.M. 1986b, *Ap.J.*, 310, 378.
- Heyer, M.H., Vrba, F.J., Snell, R.L., Schloerb, F.P., Strom S.E.,
Goldsmith, P.F., and Strom, K.M. 1987, *Ap.J.*, to be published.
- Ho, P.T.P and Townes, C.H. 1983, in *Ann.Rev.Astron.Astrophys.*, eds. G.
Burbidge, D. Layzer, and J. Phillips (Palo Alto: Annual Reviews,
Inc.), vol. 21, pp. 239-270.
- Hunter, C. 1962, *Ap.J.*, 136, 594.
- Huntress, W.T. Jr. and Anicich, V.G. 1976, *Ap.J.*, 208, 237.
- IRAS Point Source Catalogue 1985, Joint IRAS Science Working Group,
(Washington, D.C.: U.S. Government Printing Office).
- Irvine, W.M., Good, J.C., and Schloerb, F.P. 1983, *Astron.Astrophys.*,
127, L10.
- Irvine, W.M. and Schloerb, F. P. 1984, *Ap.J.*, 282, 516.
- Irvine, W.M., Schloerb, F.P., Hjalmarson, A., and Herbst, E. 1985, in
Protostars and Planets II, eds. D. C. Black and M. S. Matthews
(Tucson: University of Arizona Press) pp. 579-620.
- Keene, J., Blake, G.A., Phillips, T.G., Huggins, P.J., and Belchman,
C.A. 1985, *Ap.J.*, 299, 967.
- Knacke, R.F., McCorkle, S., Puetter, R.C., Erickson, E.F., and
Kratschmer, W. 1982, *Ap.J.*, 260, 141.
- Kutner, M.L. and Ulich, B.L. 1981, *Ap.J.*, 250, 341.
- Langer, W.D., Wilson, R.W., Henry, P.S., and Guelin, M. 1978,
Ap.J.Lett., 225, L139.

- Langer, W.D., Schloerb, F.P., Snell, R.L., and Young, J.S. 1980, *Ap.J.Lett.*, 239, L125.
- Langer, W.D., Graedel, T.E., Frerking, M.A., and Armentrout, P.B. 1984, *Ap.J.*, 277, 581.
- Larson, R.B. 1981, *MNRAS*, 194, 809.
- Leger, A., Gauthier, S., Defourneau, D., and Rouan, D. 1983, *Astron.Astrophys.*, 117, 164.
- Leung, C.M., Herbst, E. and Huebner, W.F. 1984, *Ap.J.Supp.*, 56, 231.
- Little, L.T., MacDonald, G.H., Riley, P.W., and Matheson, D.N. 1979, *MNRAS*, 189, 539.
- Lovas, F.J. 1985, *Jour.Phys.Chem.Ref.Data*, 14, 395.
- Lynds, B.T. 1962, *Ap.J.Supp.*, 7, 1.
- Marquette, J.B., Rowe, B.R., Dupeyrat, G., and Roueff, E. 1985, *Astron.Astrophys.*, 147, 115.
- Matthews, H.E. and Irvine, W.M. 1985, *Ap.J.Lett.*, 298, L61.
- Matthews, H.E., MacLeod, J.M., Broten, N.W., Madden, S.C., and Friberg, P. 1987, *Ap.J.*, 315, 646.
- McCutcheon, W.H., Dickman, R.L., Shuter, W.L.H., and Roger, R.S. 1980, *Ap.J.*, 237, 9.
- Millar, T.J. 1982, *MNRAS*, 199, 309.
- Millar, T.J. 1983, *MNRAS*, 202, 683.
- Millar, T.J. and Freeman, A. 1984a, *MNRAS*, 207, 405.
- Millar, T.J. and Freeman, A. 1984b, *MNRAS*, 207, 425.
- Millar, T.J., Leung, C.M., and Herbst, E. 1987, *Astron.Astrophys.*, to be published.

- Myers, P.C. 1980, *Ap.J.*, 242, 1013.
- Myers, P.C. 1983, *Ap.J.*, 270, 105.
- Myers, P.C. and Goodman, A.A. 1987, *Ap.J.*, submitted.
- Oppenheimer, M. and Dalgarno, A. 1975, *Ap.J.*, 200, 419.
- Penzias, A.A. and Burris, C.A. 1973, In *Ann.Rev.Astro.Astrophys.*, eds. G. Burbidge, D. Layzer, and J. Phillips (Palo Alto: Annual Reviews, Inc.), vol. 11, pp. 51-72.
- Phillips, T.G. and Huggins, P.J. 1981, *Ap.J.*, 251, 533.
- Prasad, S.S. and Huntress, W.T.Jr. 1980a, *Ap.J.Supp.*, 43, 1.
- Prasad, S.S. and Huntress, W.T.Jr. 1980b, *Ap.J.*, 239, 151.
- Prasad, S.S. and Huntress, W.T.Jr. 1982, *Ap.J.*, 260, 590.
- Rydbeck, O.E.H., Sume, A., Hjalmanson, A., Eilder, J., Ronnang, B.O., and Koilberg, E. 1977, *Ap.J.Lett.*, 215, L35.
- Rydbeck, O.E.H., Irvine, W.M., Hjalmanson, A., Rydbeck, G., Eilder, J., and Koilberg, E. 1980, *Ap.J.Lett.*, 235, L171.
- Sargent, A.I., van Drienen, R.J., Nordh, H.L., Fridlund, C.V.M., Aalders, J.W.G., and Beintema, D. 1983, *Astron.J.*, 88, 88.
- Saykally, R.J., Dixon, T.A., Anderson, T.G., Szanto, P.G., and Woods, R.C. 1976, *Ap.J.Lett.*, 205, L101.
- Scalo, J.M. 1985, In *Protostars and Planets II*, eds. D.C. Black and M.S. Matthews (Tucson: University of Arizona Press) pp. 201-296.
- Schloerb, F.P., Friberg, P., Hjalmanson, A., Hoglund, B., and Irvine, W.M. 1983, *Ap.J.*, 264, 161.
- Schloerb, F.P., Snell, R.L., and Young, J.S. 1983, *Ap.J.*, 267, 163.
- Schloerb, F.P. and Snell, R.L. 1984, *Ap.J.*, 283, 129.
- Schloerb, Snell, and Schwartz 1987, *Ap.J.*, 319, 426.

- Shu, F.H. 1977, *Ap.J.*, 214, 488.
- Shu, F.H. 1983, *Ap.J.*, 273, 202.
- Smith, D. and Adams, N.G. 1984, *Ap.J.Lett.*, 284, L13.
- Snell, Ronald L. 1981, *Ap.J.Supp.*, 45, 121.
- Snell, R.L., Schloerb, F.P., Young, J.S., Hjalmanson, A., and Friberg, P. 1981, *Ap.J.*, 244, 45.
- Snell, R.L., Langer, W.D., and Frerking, M.A. 1982, *Ap.J.*, 255, 149.
- Snell, Ron 1985, FCRAO memorandum.
- Stahler, Steven W. 1984, *Ap.J.*, 281, 209.
- Stutski, J. and Winnewisser, G. 1985a, *Astron.Astrophys.*, 144, 13.
- Stutski, J. and Winnewisser, G. 1985b, *Astron.Astrophys.*, 148, 254.
- Sweltzer, James S. 1978, *Ap.J.*, 225, 116.
- Terebey, S., Shu, F.H., and Cassen, P.M. 1984, *Ap.J.*, 286, 529.
- Thaddeus, P., Vrtilik, J.M., and Gottlieb, C.A. 1985, *Ap.J.Lett.*, 299, L63.
- Tielens, A.G.G.M. and Hollenbach, D. 1985, *Ap.J.*, 291, 722.
- Tiemann, Eberhard 1974, *Jour.Phys.Chem.Ref.Data*, 3, 259.
- Tolle, F., Ungerechts, H., Walmsley, C.M., Winnewisser, G., and Churchwell, E. 1981, *Astron.Astrophys.*, 95, 143.
- Townes, C.H. and Schawlow, A.L. 1955, *Microwave Spectroscopy* (New York:McGraw-Hill).
- Turner, B.E. and Thaddeus, P. 1977, *Ap.J.*, 211, 755.
- Ungerechts, H., Walmsley, C.M., and Winnewisser, G. 1980, *Astron.Astrophys.*, 88, 259.
- Ungerechts, H., Walmsley, C.M., and Winnewisser, G. 1986, *Astron.Astrophys.*, 157, 207.

- Vanden Bout, P.A., Loren, R.B., Snell, R.L., and Wootten, A. 1983, *Ap.J.*, 271, 161.
- Vrtilek, J.M., Gottlieb, C.A., and Thaddeus, P. 1987, *Ap.J.*, 314, 716.
- Watson, W.D. and Walmsley, C.M. 1982, In *Regions of Recent Star Formation*, eds. R.S. Roger and P.E. Dewdney (Dordrecht: D Reidel) pp. 357-377.
- Watt, Graeme D. 1983, *MNRAS*, 205, 321.
- Watt, Graeme D. 1985, *MNRAS*, 212, 93.
- Watt, G.D., and Charnley, S.B. 1985, *MNRAS*, 213, 157.
- Watt, G.D., Millar, T.J., White, G.J., and Harten, R.H. 1986, *Astron.Astrophys.*, 155, 339.
- Wilson, T.L., Downes, D., and Biegling, J. 1979, *Astron.Astrophys.*, 71, 275.
- Wilson, R.W., Langer, W.D., and Goldsmith, P.F. 1981, *Ap.J.Lett.*, 243, L47.
- Winnewisser, G., Churchwell, E., and Walmsley, C.M. 1979, In *Modern Aspects of Microwave Spectroscopy*, ed. G.W. Chantry (New York: Academic Press), pp. 313-499.
- Wootten, A., Snell, R.L., and Evans, N.J. 1980, *Ap.J.*, 240, 532.
- Wootten, A. Loren, R.B., and Snell R.L. 1982, *Ap.J.*, 255, 160.
- Yamamoto, T. 1985, *Astron.Astrophys.*, 142, 31.

